Thèse de doctorat en Physique de l'Univers
de l'Université Sorbonne Paris Cité
préparée à l'Université Paris Diderot
Ecole doctorale STEP'UP — ED N° 560
Laboratoire AstroParticule et Cosmologie

sous la direction de

Antoine Kouchner et Bruny Baret

Search for High Energy Neutrinos from the Galactic Plane with the Antares Neutrino Telescope.

soutenue le
18 septembre 2018 par

Timothée Grégoire

Présidente du jury	Université Paris 7	Pr. Alessandra Tonazzo
Directeur de thèse	Université Paris 7	Pr. Antoine Kouchner
Co-encadrant de thèse	CNRS	Dr. Bruny Baret
Rapporteur	Synchrotron à électrons allemand, DESY	Dr. Markus Ackermann
Rapporteur	Université Grenoble Alpes	Pr. Laurent Derome
Examinateur	Université de Bologne	Pr. Maurizio Spurio
Examinateur	Université de Montpellier	Dr. Éric Nuss

Abstract

Keywords— Astrophysics, Neutrinos, Galactique plane, Cosmic-rays, Gravitational waves, GW170817

Two analyses are detailed in this thesis.

A first analysis exploit the data of the ANTARES neutrino telescope to probe the presence of a Galactic diffuse neutrino flux. This analysis is based on a recent model of cosmic ray propagation in the Galaxy, the KRAγ model. This model predicts a neutrino flux particularly high and close to the sensitivity of the current neutrino telescopes. Two versions of this model exist corresponding to different cuts in the cosmic ray energy, one at 5 PeV/nucleon and an other one at 50 PeV/nucleon. A method of maximization of a likelihood function is used in order to account for the model characteristics in energy and space. The analysis has also been combined with the data of the IceCube experiment in order to exploit all the available data. Limits have been put on this model rejecting the version of the model with the 50 PeV cutoff and limiting the version with the 5 PeV cutoff to less than 1.2 times the predicted flux.

A second analysis of gravitational wave signal follow-up by the ANTARES neutrino telescope is also presented in this work. The GW170817 gravitational wave signal results from the coalescence of a binary neutron star system. This second analysis aims at probing the presence of a neutrino flux coming from this event looking for neutrino events correlated in space and time. I took part to this analysis by adding the shower-like event sample. No event has been detected in correlation. Limits have been put on the expected neutrino flux.

Résumé

Keywords— Astrophysique, Neutrinos, Plan galactique, Rayon-cosmiques, Onde gravitationnelles, GW170817

Deux analyses sont présentées dans cette thèse.

Une première analyse exploite les données du télescope à neutrino ANTARES pour sonder la présence d'un flux diffus de neutrinos galactiques. Cette analyse se base sur un modèle récent de propagation des rayons cosmiques dans la galaxie, le modèle KRAγ. Ce modèle prédit un flux de neutrinos particulièrement élevé et proche de la sensibilité des télescopes à neutrinos actuels. Il existe deux versions de ce modèle correspondant à différentes coupures sur l'énergie des rayons cosmiques, à 5 et 50 PeV/nucléon. Une méthode de maximisation d'une fonction de vraisemblance est utilisée pour prendre en compte les caractéristiques du modèle, autant spatiales qu'en énergie. Cette analyse a également été combinée avec les données de l'expérience IceCube dans le but d'exploiter au mieux les données actuelles. Des limites ont été mises sur ce modèle rejetant la version avec une coupure à 50 PeV et limitant la version avec une coupure à 5 PeV à moins de 1,2 fois le flux prédit par le modèle.

Une deuxième analyse de suivi du signal d'ondes gravitationnelles GW170817 par le télescope à neutrino ANTARES est également présentée. Le signal d'onde gravitationnelles GW170817 résulte de la coalescence d'une binaire d'étoiles à neutrons. Cette deuxième analyse a pour objectif de sonder la présence d'un flux de neutrinos provenant de cet événement en

cherchant des neutrinos corrélés spatialement et temporellement. J'ai pris part à cette analyse en y ajoutant les événement de type cascade. Aucun événement n'a été détecté en corrélation. Des limites ont été mises sur le flux de neutrino attendu.

The Long Arm of Common Sense: A Theory of the Scientific Method

It seems to me that the scientific method is rarely well understood.

Indeed, the scientific method is sometimes presented as being of a particular nature, of a nature different from our reasoning of everyday life, and in particular, of a nature profoundly different from pseudo-sciences and other beliefs. Thus science is presented as almost perfect and expressing absolute truths. "It's scientific!" say the media without trying to understand the methods of the articles presented, using the term "scientific" as an argument of authority. Everything that is "scientific" would be true, everything that is not would be false.

In opposition to this, many people fall into the opposite excess, concluding that science is a belief like any other, a dogma like any other, which "[...] does not touch or reveal reality in itself" (*Truth in Science*, Aurélien Barrau).

It is in this context that I wanted to reproduce here an excerpt from the book *Defending Science-within Reason: Between Scientism and Cynicism* by Susan Haack (2003). In this text, Susan Haack presents the scientific reasoning as being in continuity with the common sense that we all use in our everyday lives. However, she does not deny the effectiveness of science in understanding the world. The scientific method is simply described as the common sense exploited at best, to the extreme, to make the most of it.

This text was the first correct description of the scientific method I ever read. I therefore wanted to add it to my thesis, I hope you will enjoy it.

> "The scientific method is something less wonderful than it seems. Is scientific inquiry categorically different from other kinds? No, Scientific inquiry is continuous with everyday empirical inquiry—only more so. Is there a mode of inference or procedure of inquiry used by all and only scientists? No. There are only, on the one hand, modes of inference and procedures of inquiry used by all inquirers, and, on the other, special mathematical, statistical, or inferential techniques, and special instruments, models, etc., local to this or that area of science. Does this undermine the epistemological pretensions of science? No! The natural sciences are epistemologically distinguished, have achieved their remarkable successes, in part precisely because of the special devices and techniques by means of which they have amplified the methods of everyday empirical inquiry.
>
> That annoying honorific use of 'science' and its cognates notwithstanding, not all and not only scientists are good inquirers, And there is no distinctive procedure or mode of inference used by all and only practitioners of science, and guaranteeing, if not true, approximately true, or probably true, or more nearly true, or more empirically adequate results—no 'scientific method,' as that phrase has often been understood. Inquiry in the sciences is continuous with other kinds of empirical inquiry. But scientists have devised many and various ways to extend and refine the resources on which we all rely in the most ordinary of everyday empirical inquiry. Controlled experiments, for example—sometimes thought of as distinctive of the sciences—aren't used by all scientists, or only by scientists; astronomers and

evolutionary theorists don't use them, but auto mechanics, plumbers, and cooks do. In many areas of science, however, techniques of experimental control have been developed to a fine art.

[…] I recalled John Dewey's observation that '[s]cientific subject-matter and procedures grow out of the direct problems and methods of common sense,' and James B. Conant's *Science and Common Sense*; and then, to my surprise and pleasure, found Thomas Huxley observing that '[t]he man of science simply uses with scrupulous exactness the methods which we all, habitually and at every minute, use carelessly,' Albert Einstein that 'the whole of science is nothing more than a refinement of everyday thinking,' Percy Bridgman that 'there is no scientific method as such,… the most vital feature of the scientist's procedure has been merely to do his utmost with his mind'—and Gustav Bergmann describing the sciences, in a marvelously resonant phrase, as the 'long arm' of common sense."

Contents

Introduction

Since their detection by Victor Hess in 1912, the origin of cosmic rays and their propagation are not well understood. Indeed, cosmic rays being charged particles, they are deflected by magnetic fields and do not point back to their sources. Neutrinos and γ-rays are emitted subsequently to cosmic ray interactions, γ-rays being easier to detect than neutrinos, they have been used to study the cosmic ray propagation and acceleration processes. However γ-rays do not allow to distinguish firmly leptonic and hadronic acceleration processes, while neutrinos are only emitted at hadronic acceleration sites. More generally, neutrinos are very good astrophysical messengers. Indeed, they point to their sources as they are neutral, so not deflected by magnetic fields, and they interact very weakly with matter allowing them to travel cosmological distances without being affected by the matter and radiation encountered along their path. They can also escape from dense media and even from the core of astrophysical objects.

Neutrino telescopes like ANTARES and ICECUBE aim at detecting these cosmic neutrinos to exploit their characteristics. ANTARES is a three dimensional array of photomultiplier tubes installed in the abyss of the Mediterranean sea and ICECUBE is located in the ice of the South Pole. These telescopes detect the Cherenkov light induced by the charged particles produced by a (cosmic) neutrino interaction with matter, allowing to estimate its direction and energy.

The propagation of cosmic rays in the Galaxy is studied in this thesis with the ANTARES neutrino telescope data, as well as the potential acceleration of cosmic rays during the coalescence of a binary neutron star system.

This thesis is organised in three parts: the first part introduces the motivations for a neutrino astronomy, the context and the neutrino telescopes, ANTARES in particular. The second part presents a search for neutrinos from the Galactic plane based on a maximum likelihood method. The Galactic diffuse neutrino emission from cosmic ray propagation is introduced followed by the data set, the search method and the results. This study was followed by a combined search with the ICECUBE detector, exploiting the complementarity of the two detectors. The third part presents the neutrino follow-up of the gravitational wave event *GW170817*. This event marks a turning point in the history of multimessenger astronomy, as it was not only the first gravitational wave detection of a neutron star merger, but also a multimessenger detection involving tens of observatories and leading to a publication with more than 3 500 authors. This part begins by a presentation of binary neutron stars, gravitational waves and gravitational wave detectors. Then the context of the multimessenger detection is presented and the extraor-

dinary implications of this event are summarized. Finally, the neutrino follow-up is detailed as well as its results.

Part I:

Neutrino Astronomy

Chapter 1

General Context

This chapter is a short introduction to neutrinos and their use in astrophysics. The scientific motivations of a neutrino astronomy are summarized, insisting on the role that neutrinos could play to identify the sites of cosmic ray acceleration to ultra high energies. The multimessenger astronomy which aims at exploiting the synergy between the multiple messengers emitted at these acceleration sites is presented too. A special attention will be given to the potential insights that neutrinos could bring for what concerns cosmic ray propagation.

1.1 Neutrinos

The existence of neutrinos was first proposed by Wolfgang Pauli in 1930 to solve the problem of the continuity of the energy spectrum of β-rays. Indeed, at this time the beta decay was thought to be a two body decay, producing an electron with a fixed energy equal to the mass difference between the parent and daughter nucleus, however a continuous spectrum was observed. Two solutions have been proposed to solve this problem. Some physicists like Niels Bohr proposed that the conservation laws of energy, momentum and angular momentum were only statistically true. In the other hand, Pauli prefered the hypothesis of a third particle, neutral and very light that will be named later *neutrino*.

However, neutrinos were thought not to be detectable and therefore this hypothesis was reaching a limit of science, it was not falsifiable. Pauli himself said "I have done a terrible thing, I have postulated a particle that cannot be detected". Indeed, neutrinos interact very weakly and are difficult to detect, but fortunately it is not impossible. Neutrinos were detected in 1956 by Reines and Cowan [1]. More precisely, it was electron antineutrinos detected by inverse β-decay. Indeed, neutrinos exist in three different leptonic flavours: electron ν_e, muon ν_μ and tau ν_τ. Muon neutrinos have been detected six years later in 1962 [2] and its first detection in a bubble chamber (1970) is shown in figure 1.1. It is only in 2000 that tau neutrinos has been detected for the first time [3].

In opposition to what was predicted by the standard model of particle physics, the Super-Kamiokande experiment showed in 1998 that neutrinos are massive particles by detecting neutrino flavour oscillation [4]. Indeed, a neutrino produced with a certain flavour can be detected

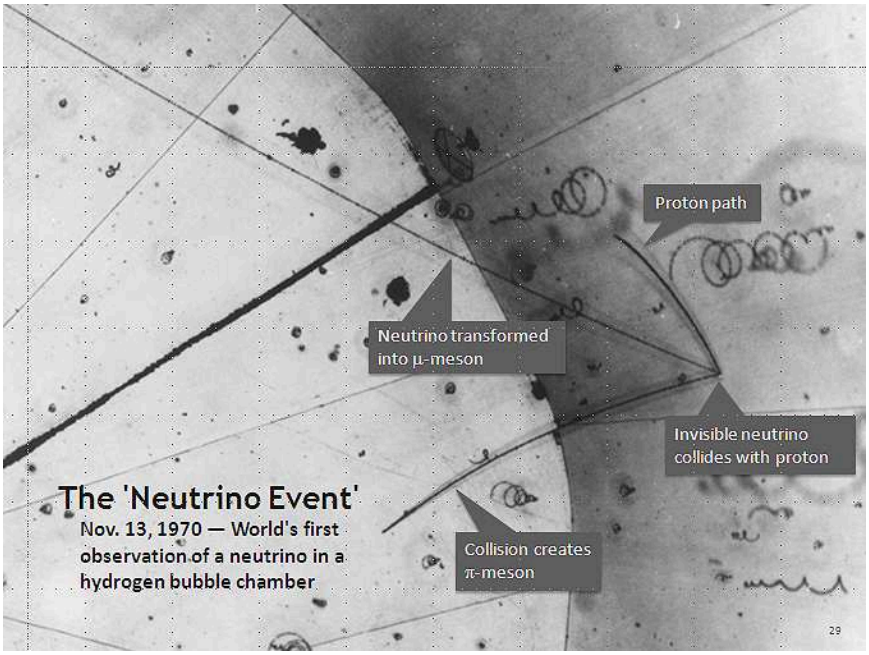

Figure 1.1 – Muon neutrino detection in a bubble chamber. Credit: Argonne National Laboratory

with a different flavour after propagation. This is due to the different propagation properties of the three neutrino mass eigenstates that change the mixture of mass and flavour states of the neutrino. Therefore neutrino oscillation implies that neutrinos are massive. However, the neutrino masses are the lowest known (and they are not even known).

1.2 Search for Cosmic Ray Origin

After the discovery of radioactivity by Henri Becquerel in 1896, the ionization of the air was considered as coming from the decay of radioactive elements, mostly from the ground. Theodor Wulf was the first to show that these radiations were increasing with altitude by doing measurements from the top of the Eiffel tower. However, the scientific community was not convinced until Victor Hess proved the existence of cosmic rays in 1912 [5] by doing measurements up to an altitude of 5 300 m with a balloon. He also took measurements during a solar eclipse showing that these cosmic rays were not originating from the Sun.

The name *cosmic rays* has been used because it was interpreted as being γ-rays[1]. Evidence was found that cosmic rays are high-energy charged particles by Jacob Clay in 1927 [6]. They are composed of 1 % electrons and 99 % nuclei, and among these nuclei there are 89 % of protons (hydrogen nuclei), 10 % of helium nuclei and 1 % of heavier elements.

Since then, the origin of cosmic rays is still an open question. Of course, there has been a substantial progress since their discovery and their origin is not totally unknown as there are many convincing hypotheses, but their deflection by magnetic fields during their propagation

[1]Which is not totally wrong as there are also γ-rays interacting within the atmosphere producing charged secondary particles.

makes difficult the localization of their acceleration sites and by consequence we cannot quantify and characterize precisely the acceleration or propagation processes.

The cosmic ray spectrum at Earth has been measured on 12 orders of magnitude in energy and 32 in flux as shown in figure 1.2. It is particularly regular and can be approximated by an unbroken power law $E^{-\gamma}$ with γ the spectral index. Nevertheless, three irregularities can be seen. At energies lower than 10^{15} eV a spectral index of 2.7 is measured, it increases to ~3.1 above. This softening of the spectrum is called the *knee*. Then the spectral index decreases again to ~2.7 after the *ankle* at $10^{18.5}$ eV. The origin of the knee and ankle are still open questions nevertheless cosmic rays are generally assumed to be of Galactic origin below the knee and extragalactic above the ankle [7].

A cutoff in the cosmic ray spectrum is measured around $5{\cdot}10^{19}$ eV [8, 9]. This can be explained by a maximum in the energy reachable at acceleration sites, but another explanation is the so-called *Greisen-Zatsepin-Kuz'min* (GZK) effect [10, 11]. Indeed, at this energy, cosmic rays are expected to interact with the cosmic microwave background via the Δ^+ resonance.

1.3 Cosmic Ray Acceleration

In 1949 Enrico Fermi proposed a clever mechanism explaining the acceleration of cosmic rays [12]. It involves a collisionless shock wave between two plasmas, which can result from a supernova explosion for example. In this context, in the interstellar medium rest frame, the shocked medium is heading toward the interstellar medium as illustrated in figure 1.3 and vice versa in the shocked medium rest frame. Moreover, the magnetic irregularities of the plasma isotropize the particle speed in its rest frame which makes it crosses the shock front again and again. The change of referential of a particle crossing the shock back and forth will increase its energy by a factor v_{shock}/c with v_{shock} the shock velocity and c the speed of light in vacuum. Instead of a referential change, the energy gain can also be interpreted as an electric field (induced by the movement of the particle relatively to the magnetic field) accelerating the particle. As the energy gain is proportional to v_{shock}, this mechanism is called the *first order Fermi mechanism* [12]. The acceleration ends when a particle's gyroradius is bigger than the cloud size and the particle escape or when the shock has no more energy and dies out.

Cosmic rays can also be accelerated in the presence of magnetized clouds moving randomly in any direction. As for the first order Fermi mechanism, the particle entering the cloud will be reflected, the clouds are called *magnetic mirrors* in this case. The change of referential of the particle will increase its energy only if the magnetic mirror is moving towards the particle, which happens more often than the contrary. The energy gain at each reflection is proportional to the square of the mirror velocity, therefore this mechanism is called *second order Fermi mechanism*.

These mechanisms predict a spectral index of the order of 2.0. The measured spectral index of 2.7 can be obtained considering the leaky box model [14] which accounts for the loss of high-energy cosmic rays escaping the Galaxy.

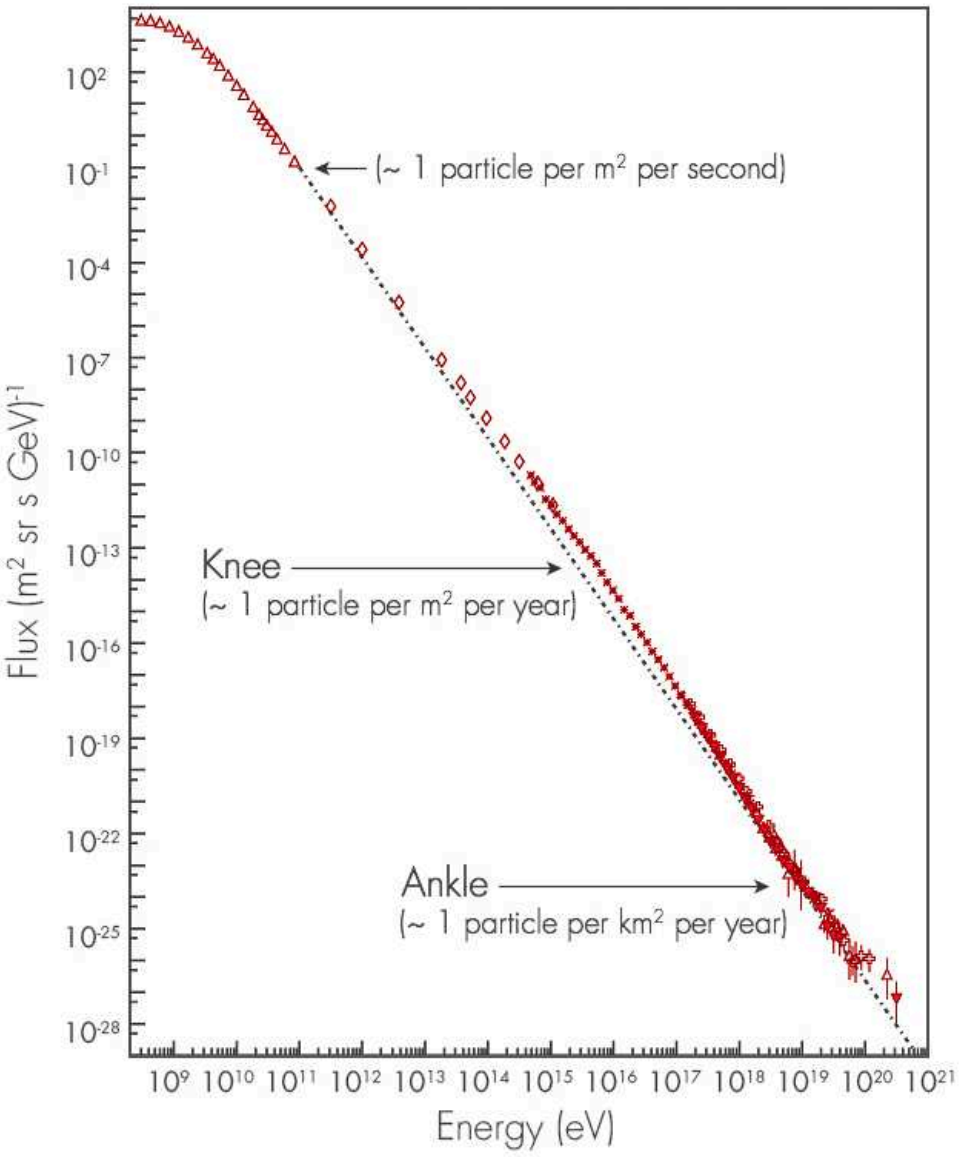

Figure 1.2 – Cosmic ray energy spectrum.

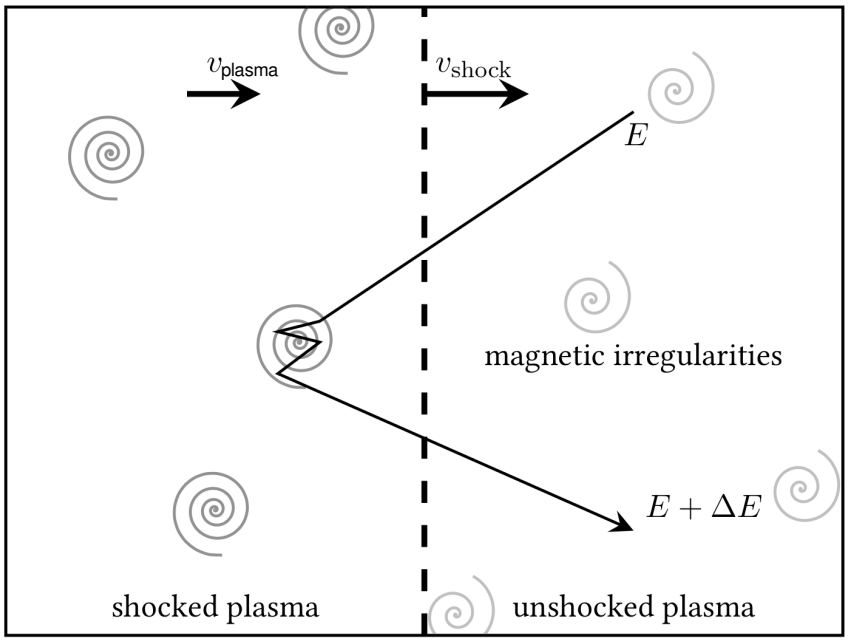

Figure 1.3 – First order Fermi mechanism. Adapted from [13].

1.4 Cosmic Ray Interaction

At acceleration sites or during propagation, cosmic rays can interact with ambient matter or radiations. We focus here on the pions that are produced via different processes like Delta-resonance

$$\begin{aligned} p + \gamma \rightarrow \Delta^+ &\rightarrow p + \pi^0 \\ &\rightarrow n + \pi^+, \end{aligned}$$

or nucleon-nucleon interaction

$$\begin{aligned} p + p &\rightarrow p + p + \pi^0 \\ &\rightarrow p + n + \pi^+ \\ p + n &\rightarrow p + n + \pi^0 \\ &\rightarrow p + p + \pi^-. \end{aligned}$$

Then the charged pions decay, producing neutrinos

$$\begin{aligned} \pi^+ &\rightarrow \mu^+ + \nu_\mu \rightarrow e^+ + \nu_e + \nu_\mu + \bar{\nu}_\mu \\ \pi^- &\rightarrow \mu^- + \bar{\nu}_\mu \rightarrow e^- + \bar{\nu}_e + \nu_\mu + \bar{\nu}_\mu \end{aligned}$$

and the neutral pions produce ɣ-rays

$$\pi^0 \rightarrow \gamma + \gamma.$$

Finally, neutrinos and γ-rays are arise from cosmic ray interactions. The γ-rays are easier to detect than neutrinos, therefore they are already used for testing the models of cosmic ray acceleration and propagation. However their interpretation is ambiguous as a comparable γ-ray emission is also expected from leptonic processes such as inverse Compton scattering, which corresponds to a low energy photon scattered to high energies by a relativistic electron

$$e^- + \gamma^{\text{low E}} \rightarrow e^- + \gamma^{\text{high E}}.$$

Up to now, the leptonic or hadronic origin of γ-rays is not known, more precisely the proportion of each is not quantified as both processes can occur from the same source. As a consequence, γ-ray data cannot be interpreted without making assumptions.

As for neutrinos, they are not expected from leptonic processes therefore their detection would provide evidence for a hadronic component of the γ-ray emission and would allow a non-ambiguous identification of the cosmic ray acceleration sites.

Moreover, neutrinos combine two ideal characteristics of an astrophysical messenger. They are neutral, therefore they are not deflected by magnetic fields and propagate in straight lines pointing back to their sources. And they interact weakly, by consequence they can travel cosmological distances without being affected by matter and radiation in their trajectory, contrary to photons. Moreover neutrinos emitted in dense environments or even from the core of a source can easily escape and be detected. This would allow accessing informations very early in the acceleration process.

1.5 Multimessenger Astronomy

As seen in the previous section, cosmic rays, γ-rays and neutrinos can be emitted by the same sources at the same time. The multimessenger astronomy tries to exploit this correlated emission. When a significant transient event is detected with a certain messenger, a search for a counterpart from the same location and time with different messengers begins. The search in a restricted area and time window allows to reject a lot of background, therefore a better sensitivity is reached. Moreover, each messenger brings different informations and the combination of these informations from a single source (like the time delay between messengers) is more valuable than the sum of the informations from different sources.

The first multimessenger detection outside our solar system occurred on February 23rd, 1987, while a burst of neutrinos was detected in three observatories few hours before the electromagnetic detection of the supernova SN1987A [15, 16, 17]. It was the closest observed supernova since 1604. It has been observed by many observatories and thanks to all the data taken is it one of the most important object of the modern astronomy.

Since then, no multimessenger detection has been done up to the last upgrade of the gravitational wave detectors. Indeed, the LIGO and Virgo detectors have recently been upgraded to advanced LIGO and advanced Virgo. LIGO accomplished the upgrade first and, while they were still running in engineering mode, measured the first gravitational wave signal from a binary black hole merger [18] opening a new window on the sky. More binary black hole coalescence

followed without any multimessenger counterpart until the first binary neutron star merger on August 17th, 2017 called *GW170817* [19]. This event has been detected as a short γ-rays burst by *Fermi*-GBM [20] less than two seconds after the gravitational wave signal. Many more electromagnetic detections followed [21].

More details about this event are given in part III as well as its neutrino follow-up to which I took part. On top of what has been explained above about the benefits of multimessenger astronomy, in the particular case of neutrino follow-up of gravitational wave, an online neutrino detection would permit to reduce the localization uncertainty from ~100 deg² to typically 1 deg², allowing an early follow-up with small field of view facilities such as optical or X-ray instruments. It would also be a proof of hadronic acceleration processes and could probe the core of the merger as mentioned previously.

The coalescence of the binary neutron star resulted in a kilonova which has been measured for the first time thanks to GW170817 helping to understand the synthesis of heavy elements. It also allowed to confirm that short γ-ray bursts are linked to binary neutron star coalescence and to refine the models of jets and dynamical ejecta. It has also been used for gravitation tests, limiting the difference between the gravitational wave speed and the speed of light as well as testing the weak equivalence principle.

Once again, the multimessenger measurement leads to great progress in the understanding of high-energy astrophysical sources, but hopefully this event, in contrast to SN1987A, should be followed by many more in the coming years.

The first success of neutrinos in a multimessenger analysis followed the GW170817 one when an electromagnetic counterpart to an IceCube alert has been claimed on September 22nd, 2017 [22]. This event is called *IceCube-170922A*, it is a ~290 TeV neutrino correlated with the TXS 0506+056 blazar as can be seen in figure 1.4. This blazar was part of the *Fermi*-LAT catalogue and was in a flaring state at the time of the neutrino detection. The hypothesis that such a neutrino event is a background event while it is correlated with such a flaring blazar is rejected at the 3σ level.

Then, the IceCube Collaboration looked for signal events coming from this source in the 9.5 preceding years (2008–2017) [23]. An excess of 13±5 events over background clustered between September 2014 and March 2015 leads to a 3.5σ evidence for neutrino emission from the direction of TXS 0506+056 prior to the IceCube alert 170922A. This excess is not correlated with a flare in γ-rays, but indications of a hardening of the spectrum have been reported [24].

Three different searches for neutrinos from this source have also been done with the Antares data [25]. The online search looked for an event correlated with the IceCube alert, the time-dependant search looked for events correlated with the cluster of IceCube events. No signal has been detected in these two analyses. An integrated analysis has also been done where 1.03 events are fitted as illustrated in figure 1.5, this leads to a 3.4 % probability to come from background, which degrades to 87 % if we account for the 106 other sources that have been searched for in the point source analysis. However, this source is the third most significant correlation.

These studies are compelling evidences that blazars can accelerate cosmic rays up to at least several PeV.

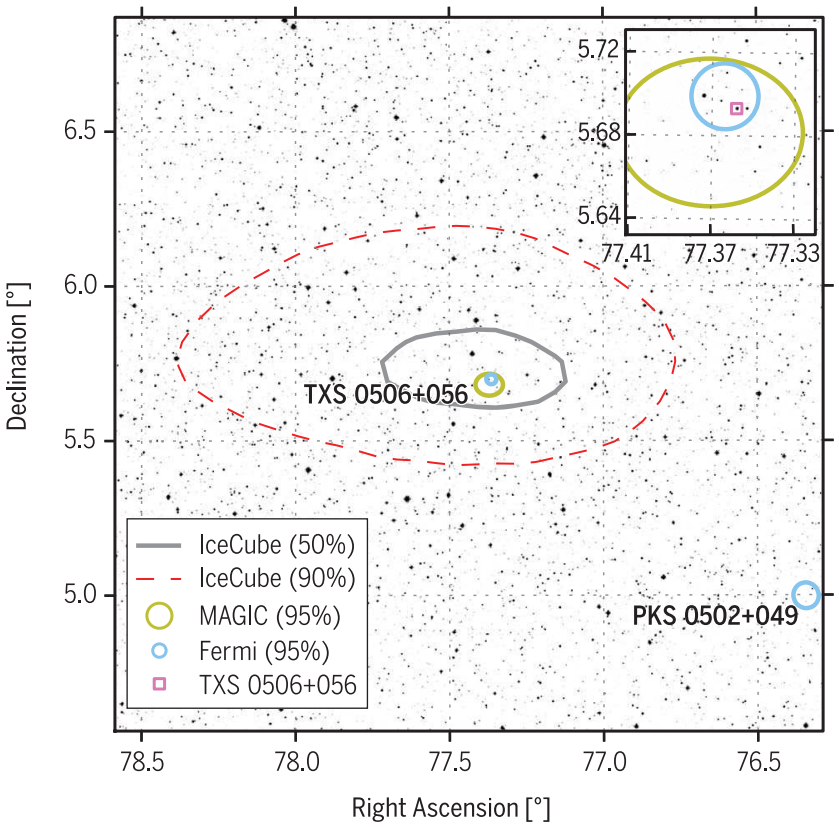

Figure 1.4 – Multimessenger observation of blazar TXS 0506+056. The 50 % (solid grey) and 90 % (dashed red) containment regions of the IceCube event are shown overlain on a V-band optical image of the sky. *Fermi* (blue circles) and MAGIC (green circles) 95 % positional uncertainty of the sources in this region are shown with the sources names. Figure taken from [22].

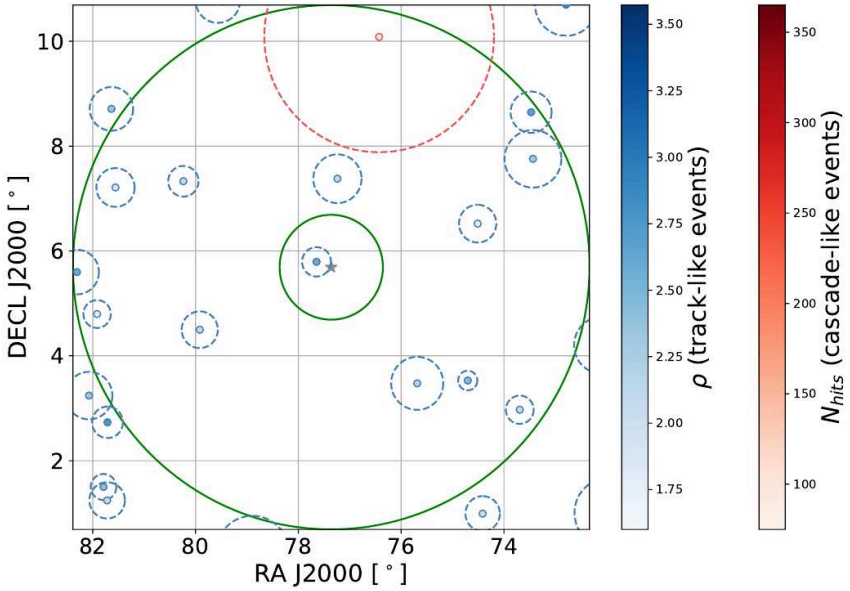

Figure 1.5 – ANTARES follow-up of IC-170922A. Distribution of ANTARES track (blue) and shower (red) events around position of the TXS 0506+056 with their angular error estimates (dashed lines). The shades of blue and red represent the values of the energy estimators, the right legend shows the colour scale. The green circles depicts the one and five degree distance from the TXS 0506+056. Figure taken from [25].

1.6 Galactic Neutrino Emission

The cosmic ray interactions presented in section 1.4 also happen during their propagation in the Galaxy, cosmic rays interacting with the interstellar medium produce neutrinos and γ-rays. Therefore, several papers claimed for hints of a Galactic component in the ICECUBE data [26, 27, 28, 29, 30].

Indeed, a cosmic neutrino flux not compatible with background has been measured and fitted with several ICECUBE event samples as can be seen in figure 1.6. The main difficulty to detect an astrophysical signal being to reject the background of atmospheric muons coming from above the detector. This difficulty is addressed in one hand, with event samples probing only the Northern sky where the Galactic component is expected to be very low (the track samples [31, 32], more details about detection principle in section 2.1). In the other hand, samples sensitive to the whole sky are used (the cascade [33] and HESE [34] samples). Four full-sky samples and two Northern sky samples are used in the combined analysis [35], which is therefore mostly sensitive to the whole sky.

Our main motivation to look for a Galactic neutrino signal was the tension between the two best ICECUBE analyses, with the six-years track sample and the combined one as illustrated in figure 1.6. The results from these two analyses are incompatible at a 3.3σ level (two-sided significance), the combined sample fitting a softer spectrum than the track one as can be expected from a Galactic component.

In the part II of this thesis, we try to probe a potential Galactic signal in the ANTARES data

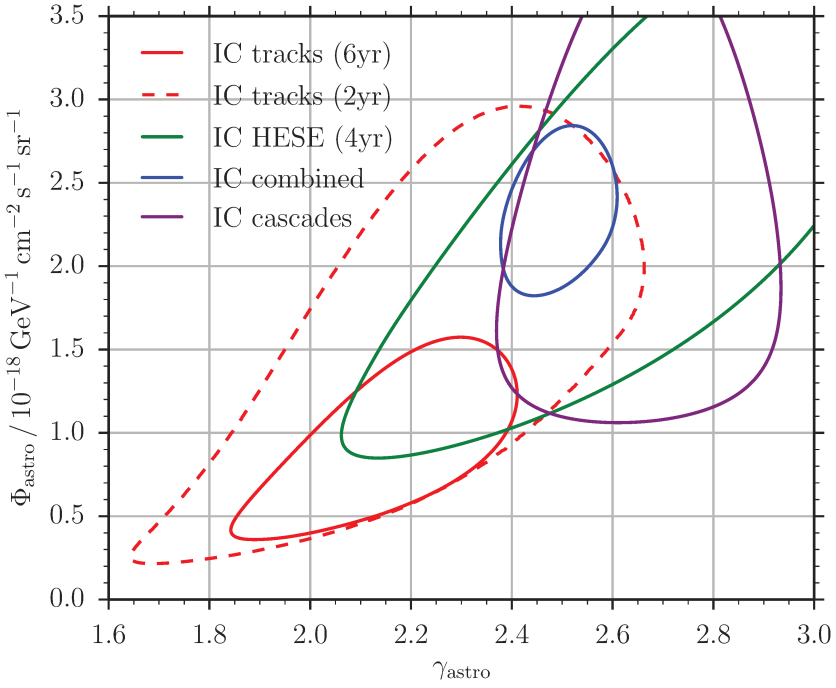

Figure 1.6 – IceCube fitted astrophysical flux parameters. Normalisations Φ_{astro} and spectral indices γ_{astro} fitted by different IceCube analyses. The contour lines represent the 90 % confidence level. Figure taken from [32].

as well as in a combination of ANTARES and ICECUBE data. To do so, we use the so-called *KRA*$_\gamma$ model [36] as a reference. It is a phenomenological model of Galactic cosmic ray propagation characterized by radially dependent transport properties. This model is fitted on the *Fermi*-LAT γ-ray data and predicts a particularly high Galactic neutrino flux peak in the Galactic centre.

Chapter 2

ANTARES Telescope

The present chapter introduces the **A**stronomy with a **N**eutrino **T**elescope and **A**byss environmental **Res**earch (ANTARES) experiment [37] on which rely the analyses presented in this work. The ANTARES project was born in 1996 and ten years later, the first detection unit has been deployed after the completion of an extensive conception and development program as well as site studies. The detector was completed in May 2008 and is still taking data.

All the knowledge necessary to understand the work presented in this thesis on the detection principle, the detector layout and data taking, the simulation and the reconstruction algorithms are detailed in this chapter.

2.1 Detection Principle

Neutrinos only significantly interact through the weak force, therefore, in neutrino telescopes, their detection relies on the secondary particles that can be induced by a neutrino interaction with matter. If the incoming neutrino energy is high, charged particles produced during the interaction can travel faster than the speed of light in the medium (water) and induce Cherenkov light. Neutrino telescopes like ANTARES detect this light and use this information to estimate the neutrino direction and energy. The neutrino interactions relevant for neutrino telescopes as well as the Cherenkov radiation mechanism are developed in the following.

As the cosmic neutrino flux is low and their interaction cross section is weak, the instrumented volume of the detector has to be very large. It must also be transparent and dark in order to see the faint Cherenkov radiation. For these reasons, the ANTARES detector is located in the depth of the Mediterranean sea. Neutrinos interact on the sea water and the rock of the ground. The detector is made of a three dimensional matrix of optical modules detecting the Cherenkov light as is illustrated in figure 2.1. The position and time informations of the detected light are used to estimate the direction of the incoming neutrino as well as its energy.

Neutrino telescopes are not able to distinguish particles from antiparticles, therefore no distinction is made in this work except if mentioned.

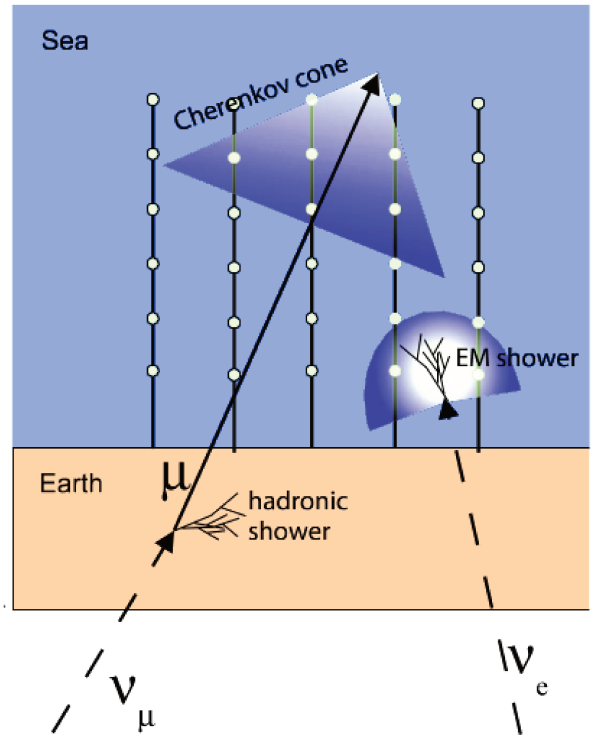

Figure 2.1 – ANTARES detection principle. A ν_μ producing a muon track and a ν_e producing an electromagnetic shower are represented.

2.1.1 Neutrino Interactions

In the standard model [38], weak interaction is mediated by the exchange of a Z^0, W^+ or W^- boson. The exchange of a Z^0 boson with a nucleon N, the neutral-current (NC) channel, can be written

$$\nu_l + N \rightarrow \nu_l + X, \tag{2.1}$$

where X stands for hadronic shower products and l is the leptonic flavour of the neutrino. The charged-current (CC) channel can be written

$$\nu_l + N \rightarrow l^{\pm} + X, \tag{2.2}$$

where a W^+ or W^- is exchanged and a lepton l is produced.

Depending on the flavour of the incoming neutrino, the interactions may have different signatures in the detector. All interactions relevant for neutrino telescopes are presented in figure 2.2.

In the analyses, the interaction channels are gathered in two categories corresponding to two different morphologies, the *track* and *shower* events. A track results from the Cherenkov light induced by a muon on a long distance as represented in figure 2.1. A shower results from hadronic or electromagnetic cascades, it is seen as a point like source in the detector. These morphologies are reconstructed by two different algorithms. The various neutrino interactions are described in the following.

Muon Neutrino Charged-Current Interaction

The charged-current interaction of a neutrino with a nucleus produces a muon and a hadronic shower (figure 2.2 top left).

The hadronic shower results from the deep inelastic interaction breaking the nucleus. This hadronic shower is present in all interactions presented here except the Glashow resonance which does not affect the nucleus.

Because of the presence of the muon, the event is referred to as a track event. A muon carrying more than a teraelectronvolt of energy can propagate up to several kilometres before decaying [39]. For this reason, ν_μ charged-current interactions occurring far from ANTARES can be detected if the muon reaches the detector which makes the effective detection volume of the detector much bigger than its fiducial size. However, most of the neutrino energy is deposited outside of the detector by consequence the energy is difficult to estimate precisely.

The muon direction can be reconstructed with good accuracy as it is seen as a long track inside of the detector. However, this direction is an approximation of the neutrino one, as part of the neutrino momentum is deposited in the hadronic system. At 1 TeV the average angle between the neutrino and muon directions is about $0.7°$ and its evolution with energy is approximately given by $0.7°/(E_\nu[\text{TeV}])^{0.6}$ [40].

Until recently, only tracks were used in the ANTARES analyses because of the high effective volume and good angular resolution they offer.

Electron Neutrino Charged-Current Interaction

The ν_e charged-current interaction produces an electron and a hadronic shower (figure 2.2 top right). The electron can experience bremsstrahlung emission, the resulting photons having enough energy to produce electron-positron pairs which can also experience bremsstrahlung emission and so on. This results in an electromagnetic cascade with a typical length of few metres. Most of the charged leptons produced in the shower are relativistic and induce Cherenkov radiation.

The shower emissions extend on a few metres only. Therefore, the angular resolution of shower events is not as good as tracks because of the granularity of the detector. Their effective volume is also lower as they must be contained in the detector in order to be well reconstructed, however they have a good energy resolution thanks to this condition.

Electromagnetic showers are the brightest, therefore ν_e charged-current interactions is better detected and reconstructed than other shower channels.

Tau Neutrino Charged-Current Interaction

A hadronic shower and a tau lepton are produced by the ν_τ charged-current interaction. The tau is a very short-lived particle ($\tau_\tau \approx 2.9 \times 10^{-13}$ s [7]). It can travel few tens of metres before decaying into a lepton (muon or electron) with the associated neutrinos or into a pair of quark-antiquark. In any case, a ν_τ is produced during the decay.

In the case of decay into a muon (figure 2.2 middle right), the event morphology is that of a ν_μ charged-current interaction.

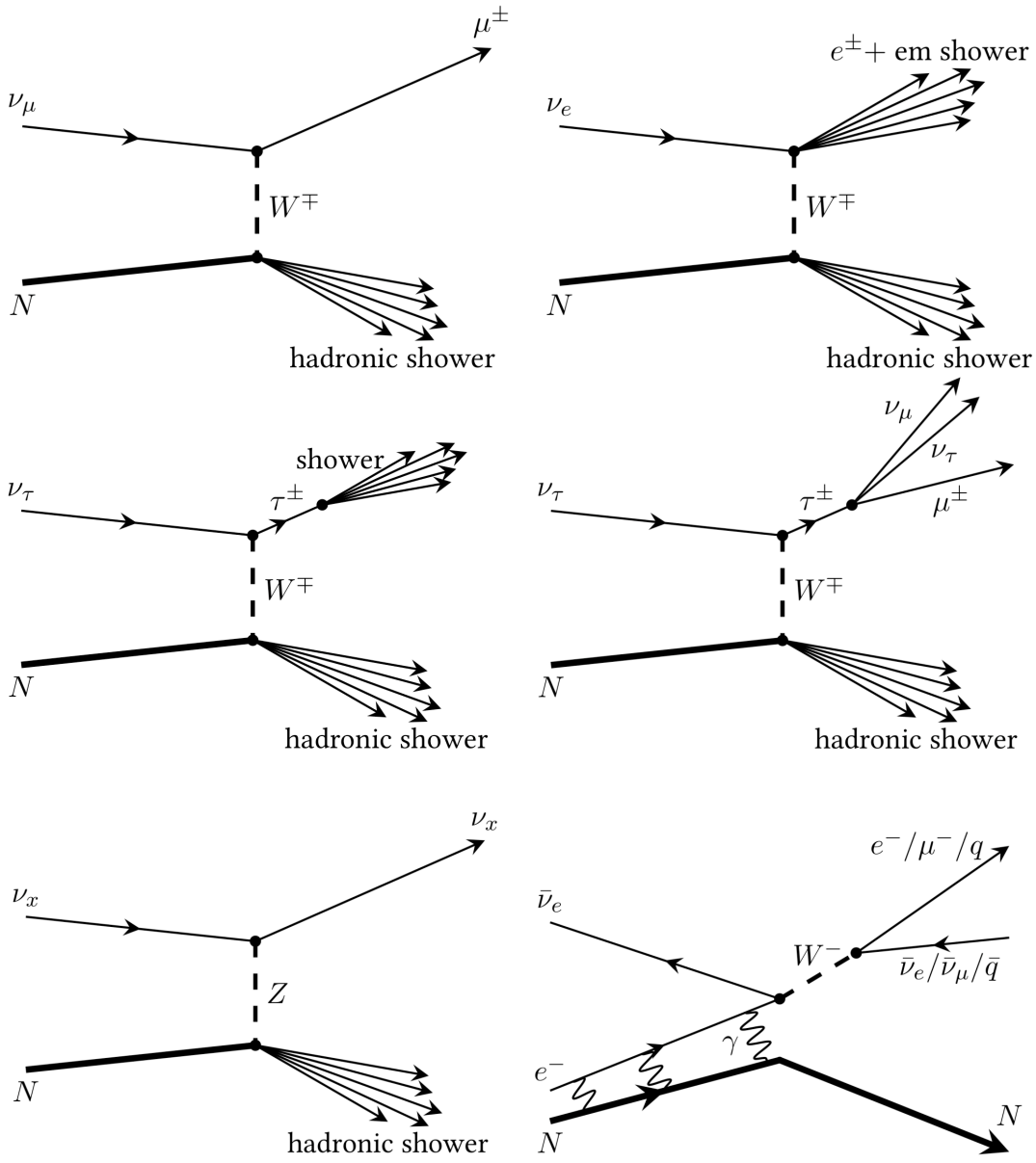

Figure 2.2 – Neutrino interactions. Diagrams of the relevant neutrino interactions in the Antares neutrino telescopes. No distinction between particles and antiparticles is made except for the bottom right plot, the Glashow resonance. The notation ν_x represents either ν_e, ν_μ or ν_τ. Adapted from [13].

A shower results from the decay into an electron or a pair of quark-antiquark (figure 2.2 middle left). The decay of a tau into a shower can produce a distinct signature in the detector. Indeed, as a shower is produced at the interaction vertex, if the tau travels a long enough distance before producing an other shower, both showers can be distinguished giving a so-called *double bang* event.

Neutral-Current Interaction

Neutral-Current interaction does not depend on the neutrino flavours. High-energy neutrinos exchanging a Z^0 boson with a nucleus by deep inelastic interaction breaks up the nucleus and creates a hadronic shower (figure 2.2 bottom left) as for all previous interactions. The charged particles created induce Cherenkov light. The neutrino remains after the interaction, by consequence only a fraction of its energy is deposited in the detector.

Glashow Resonance

If an electron antineutrino has an energy of roughly 6.3 PeV, its interaction cross section with a *stationary* ambient electron increases a lot producing a W^- boson by the so-called *Glashow resonance* [41]. Then, the W^- decays through its usual channels as shown in figure 2.2 bottom right. This interaction has not been observed in ANTARES because of the low number of PeV neutrinos.

2.1.2 Cherenkov Radiation

In a transparent dielectric medium, a moving charged particle polarizes the atoms along its path. Then the atoms relax back by emitting dipolar electromagnetic radiations. If the charged particle goes slower than the phase velocity of light (v_p) in the medium, the radiations are incoherent. In the case of a particle going faster than the phase velocity of light in the medium, nearby atoms emissions will have the same phases and so will interfere constructively, resulting in the *Cherenkov radiation* [42].

These emissions all along the particle path will result in a wave front as illustrated in figure 2.3. The emission angle θ_c with respect to the particle direction depends on the refractive index of the medium n_p and the speed of the charged particle v. It can be parametrized as

$$\cos(\theta_c) = (n_p \cdot \beta)^{-1}, \tag{2.3}$$

with $\beta = v/c$ and c the light velocity in vacuum. High-energy particles as the ones detected in neutrino telescopes travel approximately at the speed of light in vacuum ($\beta \approx 1$). The refractive index of deep sea water is roughly $n_p \approx 1.35$ which gives a characteristic Cherenkov angle of $\theta_c \approx 42°$.

Most of the Cherenkov light is emitted in the blue to ultraviolet range where the water is also most transmissive.

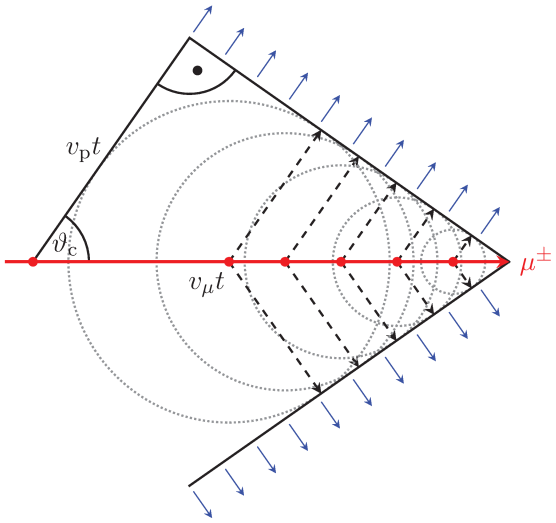

Figure 2.3 – Illustration of the cone shape of the Cherenkov effect. The atoms (red dots) along the path of the charged particle (red line) travelling faster than the light phase velocity in the medium emit Cherenkov light (dotted circles) which forms a wave front with a characteristic angle θ_c. Figure taken from [13].

2.2 Sources of Background Noise

Two types of background sources affect ANTARES. The optical background is due to the light emitted by biological organisms or to the decay of radioactive potassium present in the seawater salt. The physical background is due to cosmic-ray interactions in the atmosphere which produce muons and neutrinos that can reach the detector.

Optical Background

At the depth of the ANTARES detector, daylight is not visible, however light is measured as can be seen in figure 2.4. This is mainly due to the radioactive potassium (^{40}K isotope) β-decay into calcium. This decay produces a relativistic electron with an energy up to 1.33 MeV which can induce Cherenkov light. The concentration of potassium in the sea water is of about 416 ppm, and 0.012% of this is the ^{40}K radioactive isotope which has a half-life time of $t_{1/2} = 1.3 \cdot 10^9$ years [7].

A dark noise in each photomultiplier tube adds a detection rate 20 times lower.

Bioluminescence is an other major source of optical noise, it comes from microscopic biological organisms. Bioluminescence occurs as bursts of light, lasting a few seconds with a count rate up to 20 times more than the baseline of the ^{40}K decay, it can be seen in figure 2.4. Its average rate depends on the quantity of biological organisms which increases at spring time and is correlated with sea current velocity.

Optical background cannot be confused with cosmic neutrinos but can deteriorate the event reconstruction and affect the data transmission band-width.

Physical Background

Physical background results in the interaction of cosmic rays in the atmosphere, producing showers of particles. Among these particles only the muons and neutrinos can reach the detector. In the following, these background events will be called atmospheric muons and atmo-

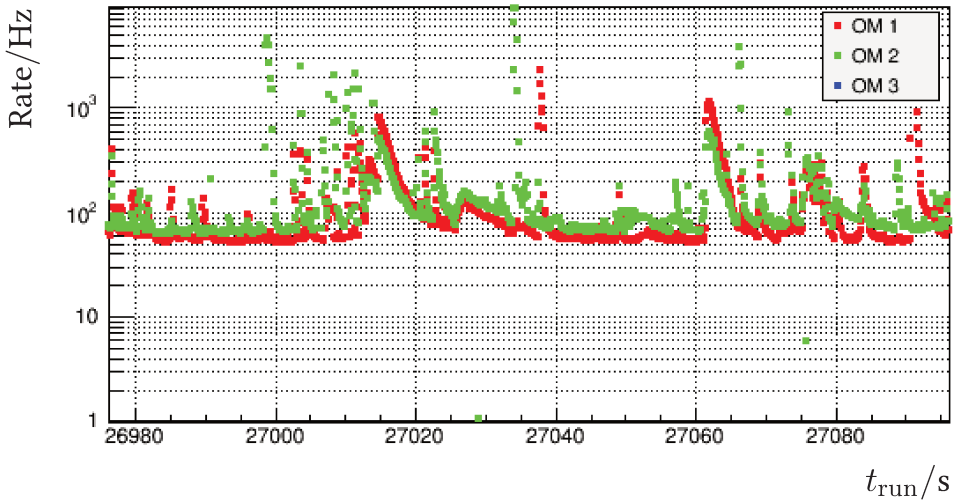

Figure 2.4 – Rate of light detection of two photomultiplier tubes. The baseline rate due to the ^{40}K decay and dark noise is visible as well as bursts of bioluminescence. Figure taken from [13].

spheric neutrinos. This physical background is more problematic than optical background as it mimic the signal events topology.

Atmospheric muons produce track-like events in the detector. As can be seen in figure 2.5 the atmospheric muon flux is very important at the detector depth, it is six orders of magnitude larger than the flux of muons induced by atmospheric neutrinos. However, it can be rejected by selecting events reconstructed as upward-going. Indeed, as illustrated in figure 2.6 the Earth is opaque to muons and mostly transparent to neutrinos [43]. A large majority of the ANTARES analyses uses upward-going events, however a background of misreconstructed muon tracks will remain depending on the selection cuts.

Atmospheric neutrinos cannot be distinguished from cosmic neutrinos on an event-by-event basis. However there are two techniques to distinguish them statistically. The energy spectrum of the atmospheric neutrino flux is softer ($E^{-3.7}$) than the cosmic neutrino one (E^{-2}), therefore we can look for excess of high-energy events. Atmospheric neutrinos are also at very good approximation isotropically distributed while part of the cosmic signal can be expected to be correlated in space and time with astrophysical sources. In the case of unknown astrophysical sources, events can be spatially and temporally correlated with each other.

2.3 Detector Layout

The ANTARES detector is located on the Mediterranean seabed at a depth of 2 475 m and at a distance of about 40 km off the coast of Toulon in the South of France at 42° 48' N, 6° 10' E (figure 2.7) [37]. This location offers a good visibility of the central part of the Galactic plane in the Southern sky when considering upward-going events.

A schematic layout of the detector is represented in figure 2.8. ANTARES is an array of 885 optical modules (OM) distributed over 12 lines. Each line is anchored to the seabed and

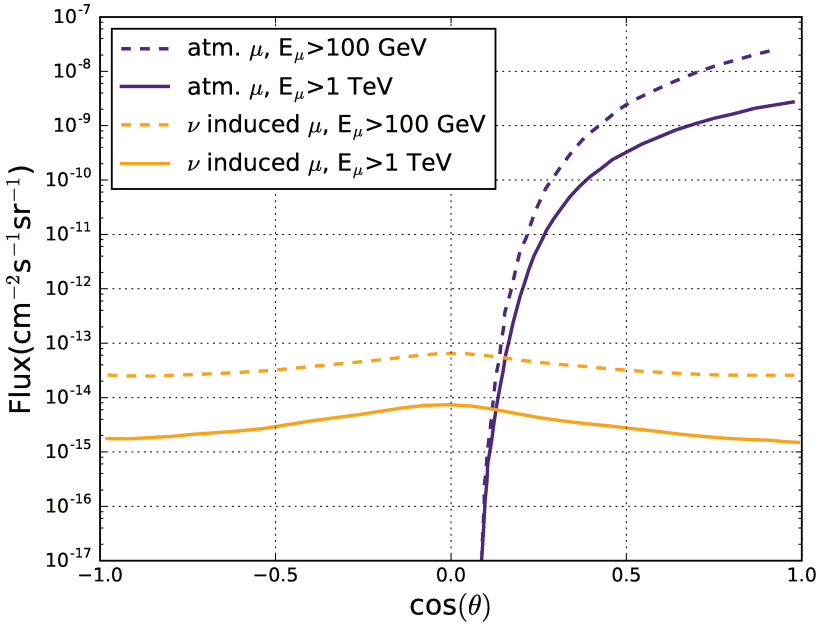

Figure 2.5 – Fluxes of atmospheric muons and muons induced by atmospheric neutrinos for two muon energy detection threshold, 100 GeV and 1 TeV, in function of their zenith angle θ at the detector depth. Events are downward-going if $\cos(\theta) > 0$. Figure taken from [44].

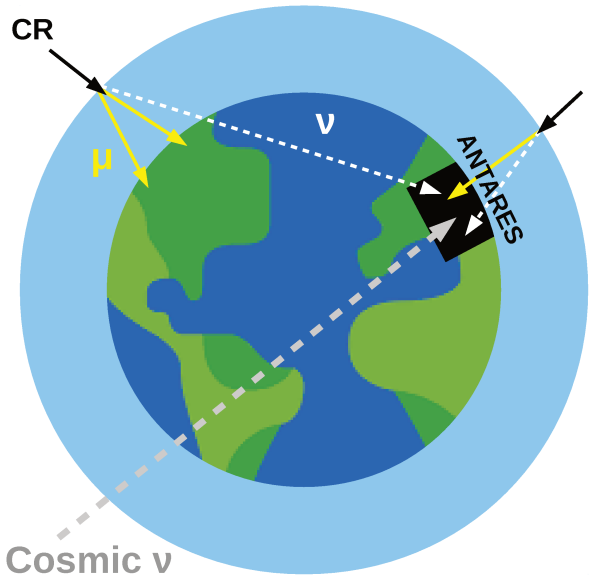

Figure 2.6 – Effect of the Earth on the different physical events.

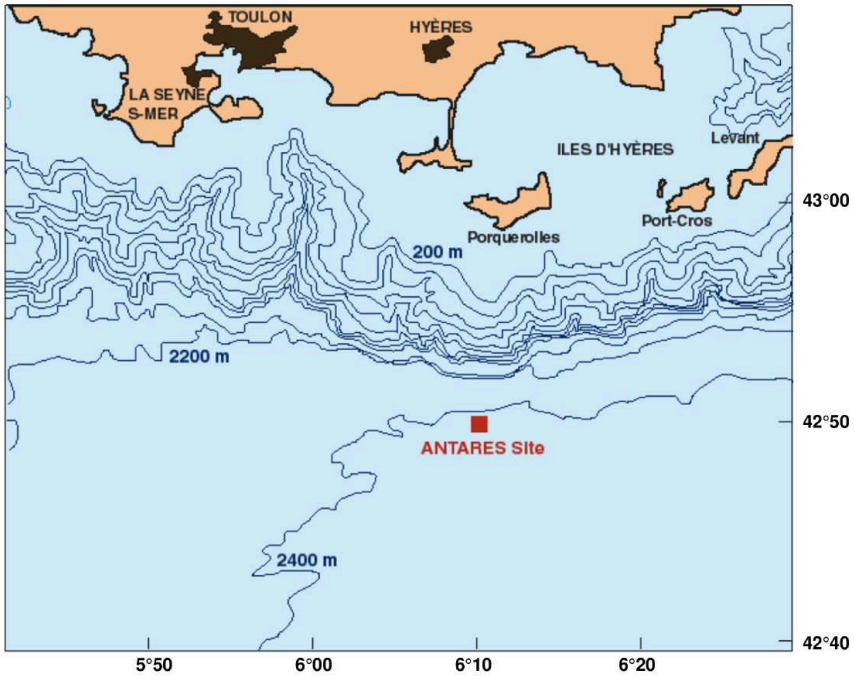

Figure 2.7 – Location of the ANTARES detector in the Mediterranean sea off coast of Toulon, France (red square).

pulled up straight by a buoy at a height of 480 m. Two nearby lines are separated by ~60 m. A long cable from the shore is connected to the junction box which distributes the power supply to every line as well as collects and transfers the data to shore.

Optical modules are attached to the lines by the *storeys* as can be seen in figure 2.9. Each line contains 25 storeys with 14.5 m vertical spacing between two adjacent storeys starting 100 m above seabed. Each storey houses three optical modules looking downward at 45° and a *local control module* (LCM) housing the electronics. The upper five storeys of line 12 (L12 in figure 2.8) hold acoustic neutrino detection hardware instead of optical modules [45]. The instrumentation line (IL07 in figure 2.8) carries oceanographic and acoustic equipments as well as optical modules for longterm bioluminescence rate tracking. This line is now disconnected.

An ANTARES optical module consists of a photomultiplier tube (Hamamatsu R7081-20) with a 500 cm² photocathode area inside a pressure-resistant glass sphere of 43 cm diameter (figure 2.10). The photomultiplier tube is coupled to the glass through an optical gel with a refractive index of 1.4. The photo-cathode is sensitive to light in the wavelength range 300–600 nm, matching the Cherenkov light, with a maximum quantum efficiency of 25 % at 370 nm. A Faraday cage of high magnetic permeability metal surrounds the photomultiplier tube to prevent the Earth magnetic field to disturb the electron currents and the measurement.

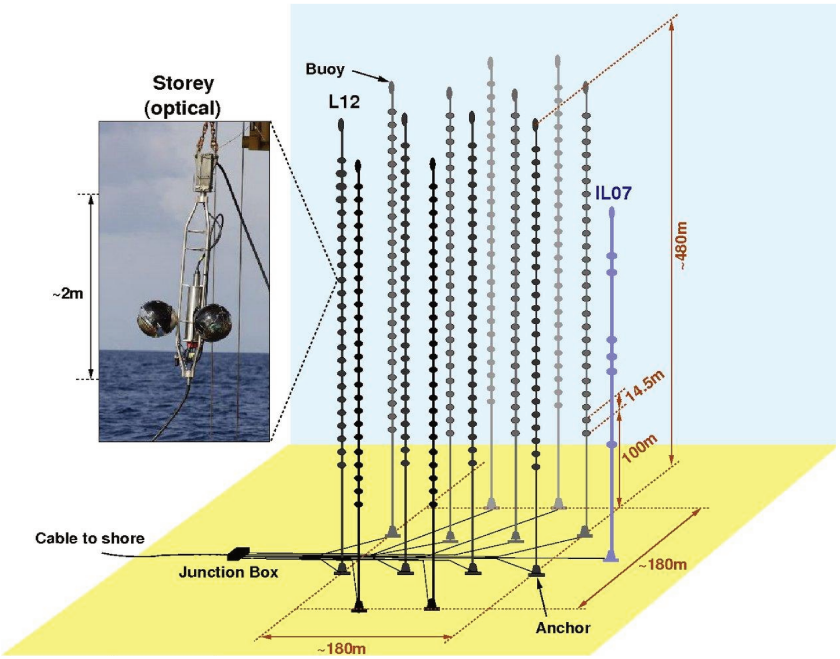

Figure 2.8 – Schematic view of the ANTARES detector layout.

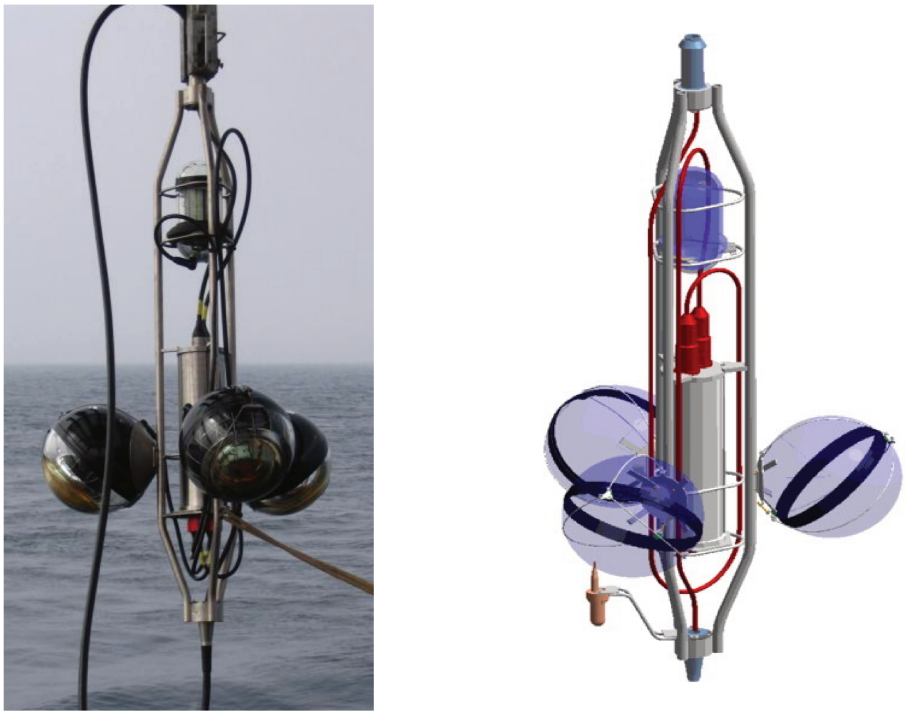

Figure 2.9 – Photograph and computer model of an ANTARES storey. On the computer model: The grey cylinder is the *local control module*, the purple spheres represent the three optical modules. Some of the storeys are additionally equipped with hydrophones (orange, bottom left) and LED-flashers (blue cylinder, top).

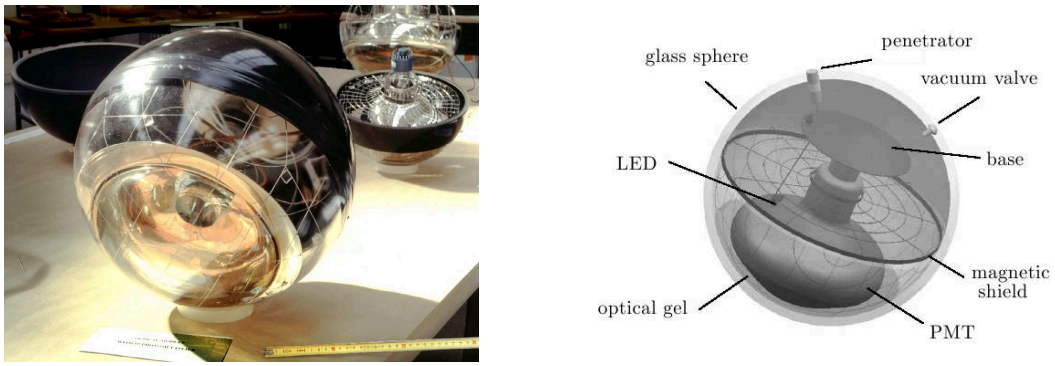

Figure 2.10 – Photograph and schematic of an ANTARES optical module.

2.4 Data Acquisition System

As detailed in [46], the ANTARES data acquisition system relies on the *all data to shore* concept. Each photon detected by a photomultiplier tube, a *hit*, is digitised at the level of the storey and send to shore through an optical fibre. Onshore, the computer farm runs algorithms selecting hits resulting from physical events in order to save them. These algorithms will be called *triggers* in the following.

2.4.1 Offshore Data Acquisition

The light detection by an optical module happens when a photon hitting the photocathode kicks out an electron which is then accelerated by the high electric fields produced by the high voltage of the photomultiplier tube. This electron will hit the first dynode and start an avalanche of secondary electrons. These electrons will produce an electric signal with a pulse shape. In order to reject the dark noise, the signal is processed if its pulse integrated charge is greater than $1/3$ p.e., with a p.e. being the mean of a single photoelectron pulse. This is the level 0 trigger, so these signals are called *L0-hits* or simply *hits*.

The electric signals are digitized by the custom-made chips called *Analogue Ring Samplers* (ARSs) [47] and the integrated pulse charge is measured. Two analogue ring samplers per optical module are used in order to reduce deadtime.

The time of the hit is measured too. At each storey, a local clock is synchronised with an onshore master clock. The ticks of the clock are used as time stamps and the time between a tick and a hit (1/3 p.e. threshold crossing) is measured by a Time to Voltage Converter (TVC). The output of the time to voltage converter is digitized by an Analogue to Digital Converter (ADC).

The hits time and amplitude informations are organised in dataframes of 105 ms which are send to the shore by a Central Processing Unit (CPU). A Dense Wavelength Division Multiplexing (DWDM) uses different wavelength to send the different data streams to shore through the Main Electro-Optical Cable (MEOC).

2.4.2 Onshore Data Filtering and Triggering

The onshore data filtering is the main challenge of the ANTARES data acquisition system, between 0.3 to 1 GB/s of data have to be processed. The general idea is to select the hits resulting from physical events (neutrinos or muons) and to reject the optical noise. To do so we are looking for causally correlated hits in the detector.

The level 1 hits (or L1-hits) are defined as two or more hits from optical modules of the same storey that occur within a 20 ns time-window. Hits with a high amplitude (typically > 3 p.e.) are also classified as L1-hits.

Then, L1-hits are considered as resulting from a physical event if they are causally related, using

$$|t_i - t_j| \leq |\vec{r}_i - \vec{r}_j| \cdot v_g + 20\,\text{ns}, \tag{2.4}$$

with t_i the time of the hit i, $\vec{r}_i$ the position of the corresponding optical module and $v_g = c/n_g$ is the group velocity of light in water. The additional 20 ns account for potential scattering of the light or time calibration uncertainties.

If a sufficient number of L1-hits are causally correlated (typically ≥ 5 L1-hits) then all the L0 hits within 2.2 µs before the first and after the last L1-hits are written to disk. The value of 2.2 µs roughly corresponds to the time needed for a muon to cross the detector. The rate of such physical events triggered is between 1 to 10 Hz, most of these being atmospheric muons.

After this first filter, higher level trigger selections are applied, a robust one (3N) and a less robust but more effective in particular at low energies (2T3):

T3 Trigger The T3 trigger requires L1-hits coincidence on adjacent or next-to-adjacent storeys of the same line. The coincidence time window is of 100 ns for adjacent storeys and 200 ns for next-to-adjacent. A more stringent version of this trigger is used, the 2T3 trigger which requires two T3 clusters within 2.2 µs.

3N Trigger The 3N trigger uses the assumption that the light is produced by a muon track. Indeed, the algorithm look for hits that can result from a same track scanning over 210 directions. The time t_i for a photon emitted by a muon to arrive at an optical module can be expressed as

$$t_i = t_0 + \frac{1}{c}\left(z_i - \frac{r_i}{\tan(\theta_c)}\right) + v_g \frac{r_i}{\sin(\theta_c)}, \tag{2.5}$$

with t_0 the time at which the muon passes $z_i = 0$ and θ_c the Cherenkov angle. The parameter r_i is the distance of closest approach of the track to the optical module. Therefore the two hits can be emitted by a same muon track if they respect the inequality

$$|t_i - t_j| \leq \frac{|z_i - z_j|}{c} + \frac{R_{ij}}{c}\,\tan(\theta_c) + 20\,\text{ns}, \tag{2.6}$$

with R_{ij} the distance between the optical modules in the plane perpendicular to the muon direction. All these parameters are illustrated in figure 2.11.

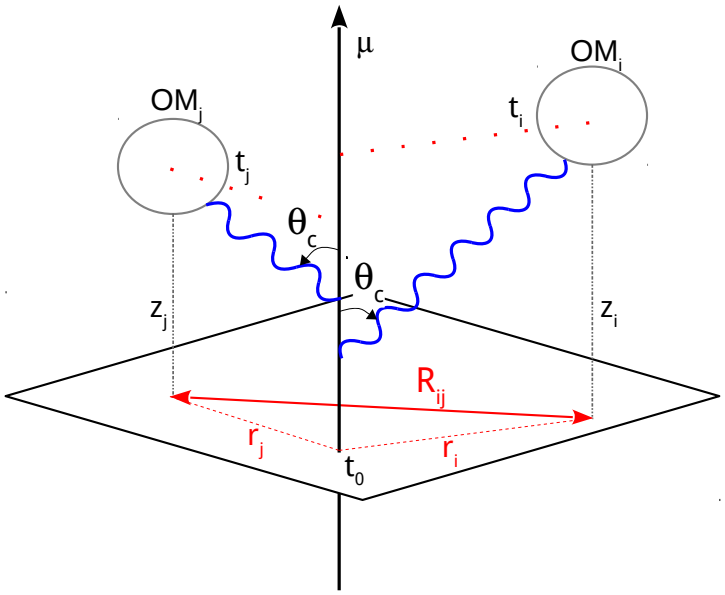

Figure 2.11 – Parameters used to define the causal relation between two L0-hits for the passage of a muon track as given by equation 2.6.

2.4.3 Calibration

The ANTARES physics analyses rely on the neutrino energy and direction reconstructions. The accuracy of the charge reconstruction is crucial for the energy estimation, mostly, while the accuracy on timing and optical module positions are crucial for the direction reconstruction. The calibration procedures of the detector allow to reach the required accuracy.

Time Calibration

The time calibration [48] has two goals: the measurement of the time resolution of each optical module and of the relative time offset between optical modules.

Inside each optical module a LED is mounted in order to illuminate the photocathode from the back. This allows measuring the difference between the hit time as given by the readout electronics and the real time of the photon hitting the photocathode. This includes the transit time of the photomultiplier tube which is the time between the hit on the photocathode and the output of the tube, as well as the time taken by the readout electronics. A time resolution of ≈ 1.3 ns is measured. From previous measurements, we know that this comes mainly from the transit time of the photomultiplier tubes.

Two laser beacons are mounted at the bottom of the lines 7 and 8 and optical beacons are mounted on storeys 2, 9, 15 and 21 of each line. The optical beacons are used to measure the time offsets between optical modules of a same line while the laser beacons are used for inter-line time offsets. A diffuser is placed on the laser beacon so that the light is seen by all surrounding lines.

Position Calibration

The ANTARES lines are pulled up by buoys, therefore they can move with sea currents. The goal of the position calibration is to measure the position and orientation of each storey of each line as well as the absolute position of the detector, in order to meet the targeted precision for track reconstruction.

The measure of the storey positions is done by triangulation with acoustic signals. Indeed, an acoustic transceiver is installed at the bottom of each line as well as an additional one located at a distance of 145 m from the detector. Hydrophones are mounted on storeys 1, 8, 14, 20 and 25 of each line. Measurements of the time elapsed between emission and reception are performed every two minutes. Oceanographic instruments are monitoring the sound velocity in the seawater which allows determining distances. Then a fit of the line shape is used in order to find the position of all the storeys reaching an accuracy better than 10 cm. [49]

In each storey, a bi-axial tiltmeter and a compass measure the storey orientation, allowing for some redundancy on the position determination.

The detector geographical position is measured by the GPS positioning of the ship used during the deployment of the lines.

Charge Calibration

The goal of the charge calibration is to link the number of photo-electrons associated to the measured amplitude of the signal. It is of prime importance as it affects the L1-hit triggering. The calibration must reproduce the time evolution of the related quantities in order to ensure stable and optimal simulation and reconstruction accuracy.

Before deployment, measures have shown that the relation between the number of photo-electrons and the digitized amplitude output is linear. Then, the conversion from the digitized amplitude called AVC and the number of photoelectrons $Q_{p.e.}$, is done with

$$Q_{p.e.} = \frac{\text{AVC} - \text{AVC}(0\,p.e.)}{\text{AVC}(1\,p.e.) - \text{AVC}(0\,p.e.)}, \tag{2.7}$$

with $\text{AVC}(1\,p.e.)$ the AVC measured from the optical background which comes mainly from single photoelectrons, and $\text{AVC}(0\,p.e.)$ the AVC measured from the baseline of the photomultiplier tubes.

For charges higher than about 20 photoelectrons the readout electronics saturates and no further differentiation is possible.

During my PhD I took part to the charge calibration as a service task. For each optical module the $\text{AVC}(1\,p.e.)$ is automatically fitted by a Gaussian function. However, because of the ageing of the photomultiplier tubes and the biofouling of the optical modules, the peak of 1 p.e. can change and the fit can fail. The fitting program checks if the fit is correct comparing the average and standard deviation of the fitted Gaussian with the fit of the previous calibration. If these quantities differ more than predefined values, the fitting goes into manual mode. My participation has been to check these fit for the two ARS of the 885 optical modules, to redo the fit if needed or to use the fit of the previous calibration if it was correct. The program can also go into manual mode if the ARS is noisy. The ARS is considered noisy if one bin of the

distribution of the time to voltage converter (TVC) collects more than 4 % of the total number of events, which is an empirical rule of thumb.

After the charge calibration, we check that the fitted AVC($1\,p.e.$) is higher than the AVC($0\,p.e.$).

More details are given in [50].

2.4.4 Data Quality

To account for varying conditions in marine environment, ANTARES data are organized by runs [51]. A run is a period of data taking usually lasting between six and twelve hours to which is attached various informations about the light background, the calibration features and more generally the data quality. These informations are used to simulate the real conditions of data taking but also to select the runs to be analysed.

The data quality parameter has a value of 0 assigned to runs that have a malfunction of the detector, a high background light due to bioluminescence or runs which are too short. All other runs have a good quality parameter of 1 or even more if the background light is particularly low with a high number of working optical modules.

Malfunctioning optical modules can sporadically produce very bright sparks that are reconstructed as shower events by the algorithms. Runs containing these sparks are identified and excluded.

Some of the runs, flagged as *SCAN* runs, have been used for dynamic calibration. Therefore some of the control variables (high voltage, trigger definitions...) have been modified on the fly and the history of changes were not stored automatically in the data base as for other runs. However, all these modifications have been written down in a log and thanks to this, several of these runs have been recovered and can therefore be used in the analyses.

2.5 Simulations

Simulations are crucial in particle physics analyses to understand or interpret the data. They are used for the event reconstruction as well as in the analyses in order to produce pseudo-experiments. Simulations allow to estimate the statistical relations between true values and the estimated ones, like the energy or direction of an event or the number of signal events in a pseudo-experiment. To do so, Monte Carlo methods, based on random generation are used. Therefore simulations will often be called *Monte Carlo simulations* or just *Monte Carlo* in this work.

The accuracy of the simulation is very important. To check for this, we compare distributions from simulations and data. We consider the simulation not reliable for a variable if data and simulations are not adjusted.

In ANTARES the full simulation is done in three stages, the event generation, the photon tracking and the detector response.

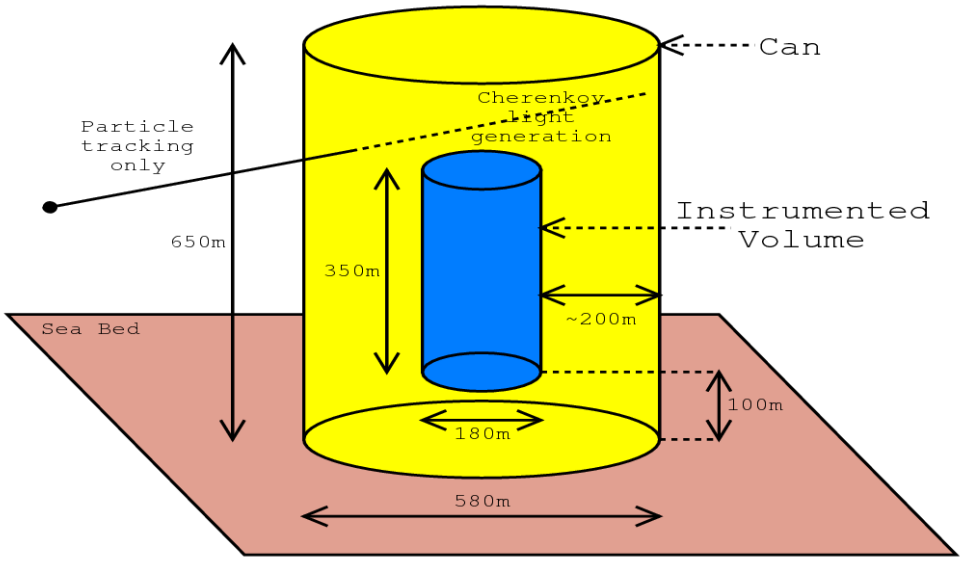

Figure 2.12 – Size of the can (yellow) used for the simulation, in comparison with the instrumented volume (blue).

2.5.1 Event Generation

Two different volumes surrounding the detector are used in the simulation, the generation volume and the can. The generation volume has a radius and height of 25 km, a size chosen in order to generate every neutrino which can produce a muon that can reach the detector. It is only in the can that the light is generated, the can being the volume in which a Cherenkov emission can reach the detector. The can is represented in figure 2.12 with the detector represented by the instrumented volume.

Neutrino Generation

The neutrino event generation procedure [52] is described in figure 2.13. First, the neutrino energy is picked up. Then, a vertex is generated randomly in the generation volume accounting for the higher density of rock compared to water. Third stage, the shortest distance between the vertex and the can is computed checking that it is shorter than the maximum distance reachable by a muon [53] with the energy picked up previously. If it is the case, the neutrino direction is generated. Then it is checked if the neutrino direction (as an approximation of the muon one) passes close to the detector. At the fifth stage the interaction is generated, if the event is in the can, the energy and direction of all the particles are saved, otherwise the muons are propagated and the ones that cross the can are saved.

The same number of neutrinos are simulated for each energy decade between 10^2 and 10^8 GeV.

Then, events are weighted by

$$w_{\text{gen}} = V_{\text{gen}} \cdot \rho \cdot N_A \cdot \sigma \cdot P_{\text{Earth}} \cdot I_\theta \cdot I_E \cdot E^\gamma \cdot \Delta t_{\text{gen}}, \tag{2.8}$$

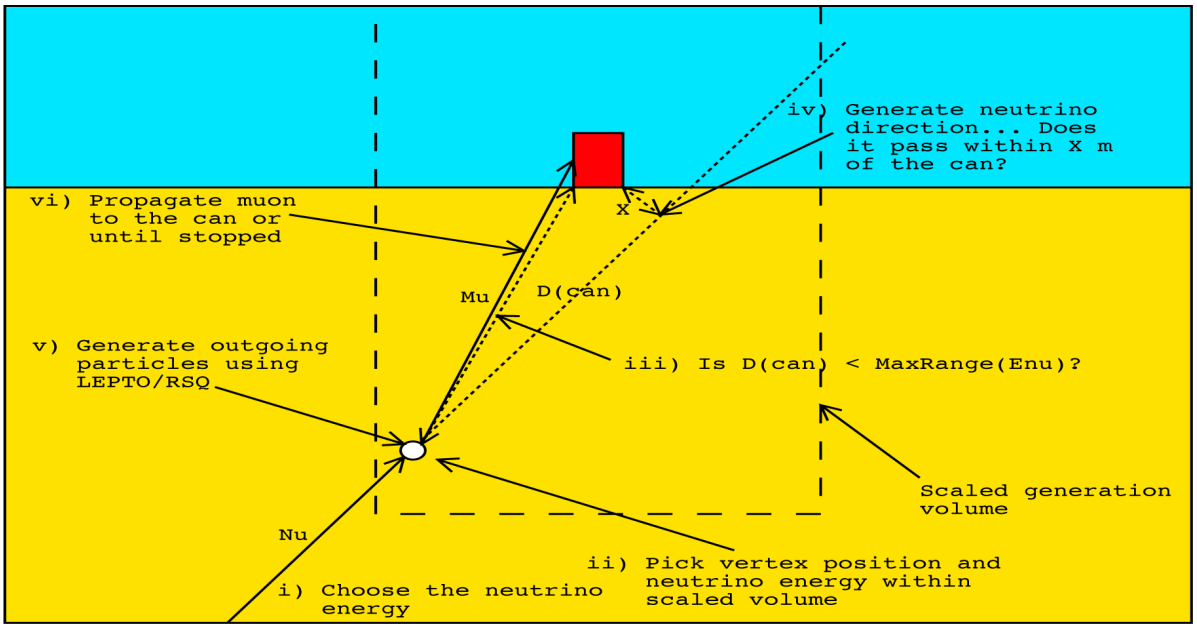

Figure 2.13 – Neutrino Generation. Description of the different stages of the neutrino generation.

with:

- V_{gen} [m³]: the generation volume.
- ρ [mol·m⁻³]: the density of target nucleons per unit volume and N_A the Avogadro number.
- $\sigma(E_\nu)$ [m²]: the neutrino cross-section.
- $P_{\text{Earth}}(E_\nu, \theta)$: the probability of the neutrino to pass through the Earth without being absorbed.
- $I_\theta = 2\pi(\cos(\theta_{\text{max}}) - \cos(\theta_{\text{min}}))$ [sr]: the angular phase space factor, it is the integral of the solid angle.
- $I_E = (E_{\text{max}}^{1-\gamma} - E_{\text{min}}^{1-\gamma})/(1-\gamma)$ [GeV$^{1-\gamma}$]: the energy phase space factor, with γ the input spectral index. It is the integral of the generation spectrum.
- Δt_{gen} [s]: the interval of time simulated (a year).

Tau Neutrinos Until now, ν_τ are not simulated (they will be added very soon). Indeed, they usually produce hadronic showers which are not emitting as much light as electromagnetic showers or muon tracks, therefore less of them are triggered and their reconstruction quality is of bad. Moreover, there is no tau neutrinos in the atmospheric background. In order to account for these events, interaction channels of ν_e and ν_μ are scaled up by a factor shown in Table 2.1. These factors are obtained from dedicated simulations. A tau produced by charged

Table 2.1 – ν_τ scaling factors. Scaling factors to apply on ν_μ and ν_e channels in order to account for ν_τ interactions.

Simulated channel	Scaling factor	Associated ν_τ channel
ν_μ NC	1.0	
ν_μ CC	1.09	0.09: ν_τ CC $\longrightarrow \mu$
ν_e NC	4.74	1.0: ν_τ NC $\longrightarrow$ had 2.74: ν_τ CC $\longrightarrow$ had
ν_e CC	1.12	0.12: ν_τ CC $\longrightarrow$ e

current interaction has 17 % chance to decay into a muon (ν_τ CC $\longrightarrow \mu$) and 18 % into an electron (ν_τ CC $\longrightarrow$ e). The corresponding factors are smaller due to the missing energy carried by the two neutrinos produced during the tau decay that diminish the probability of triggering the event. In other cases the tau decays into a hadronic shower. The scaling factor corresponding to the charged-current interaction producing a hadronic shower (ν_τ CC $\longrightarrow$ had) is high because the cross section of charged current interactions is roughly twice the one of neutral current interaction. It is also because the resulting showers produce more light in average and are in consequence easier to detect. See section 2.1.1 for details about the interaction types.

Atmospheric Muon Generation

The number of atmospheric muons detected is way higher than atmospheric neutrinos. By consequence, obtaining a realistic sample in terms of statistics is very time consuming. To reduce this time, parametrisations of the energy and angular distributions of the muon flux under-water are used. This is done by the *MUPAGE* software [54]. This method is much less time consuming than a full simulation. However it is still too long to simulate all muons, one third of them is simulated and a weight of 3 is applied.

2.5.2 Particles and Light Propagation

The particles reaching the can volume are simulated with their energy losses and light emission by the *KM3* package, based on *GEANT* [55]. It would require too much CPU time to simulate every photons, and it is not necessary as the seawater is homogeneous. The *KM3* package uses tables from full simulations to determine the energy losses, scatterings and the photon distributions. The number of hits on optical modules, their arrival time and position with respect to the photomultiplier tube orientation are evaluated.

2.5.3 Detector Response

The *TriggerEfficiency* program accounts for the data taking conditions of the detector, simulate the electronic response and the triggering.

The first stage is to add the optical background due to the radioactive decay and the bioluminescence. This is done by using a Poisson probability distribution and based on the measured

rates in the data run. The detector condition is also simulated, such as the number of inactive optical modules. The electronic is simulated by accounting for the time needed by the chips to digitize the signal as well as its dead time. The time and charge resolutions of the optical modules are also simulated based on the calibration measurements. Then the triggers are applied like in the data run.

2.6 Event Reconstruction

Reconstruction algorithms are used in order to estimate the direction and energy of the incoming neutrino. Depending on the event topology, different reconstructions are used. Some of the output parameters of these algorithms are used in the analyses described in this thesis in order to select events with the best reconstruction quality. They will be presented.

2.6.1 Track Reconstruction

A detailed description of the track reconstruction algorithm can be found in [56]. The reconstruction is divided into two algorithms, one for the direction of the event and an other one for the energy.

Event Direction

The event direction relies on a hit pre-selection, which selects only the hits that are causally related by $|t_i - t_{\text{max}}| \leq (\vec{r}_i - \vec{r}_{\text{max}})/v_g + 100\,\text{ns}$, with t_i and $\vec{r}_i$ the time and position of the hit i and t_{max} and $\vec{r}_{\text{max}}$ the time and position of the hit with the largest amplitude. The parameter v_g is the group velocity of light in water.

In order to estimate the event direction, the position of the track at a time t_0 should also be determined. Therefore, there are five free parameters to estimate. A fitting procedure in multiple steps is used, each step being the starting point of the following one. The final step account for all L0-hits and is the maximization of a likelihood function to obtain this set of hits with their time and amplitude, accounting for the optical background and the light scattering.

The fitted value of the logarithm of the likelihood per degrees of freedom Λ_{Tr} is used as an estimator of the fit quality, indeed lower is the likelihood less likely is the fitted value. This is combined with the information of the number of times the same value has been obtained from fits with different starting points. An estimation of the angular error of the reconstruction β_{Tr} is also computed from the second derivative of the likelihood function at the fitted point, which corresponds to the standard deviation of the minimum of the likelihood in the Gaussian approximation.

Event Energy

A simple estimator of the event energy is the number of hits (N_{hits}) selected for the direction reconstruction, as an estimation of the number of hits produced by the track. But this is not

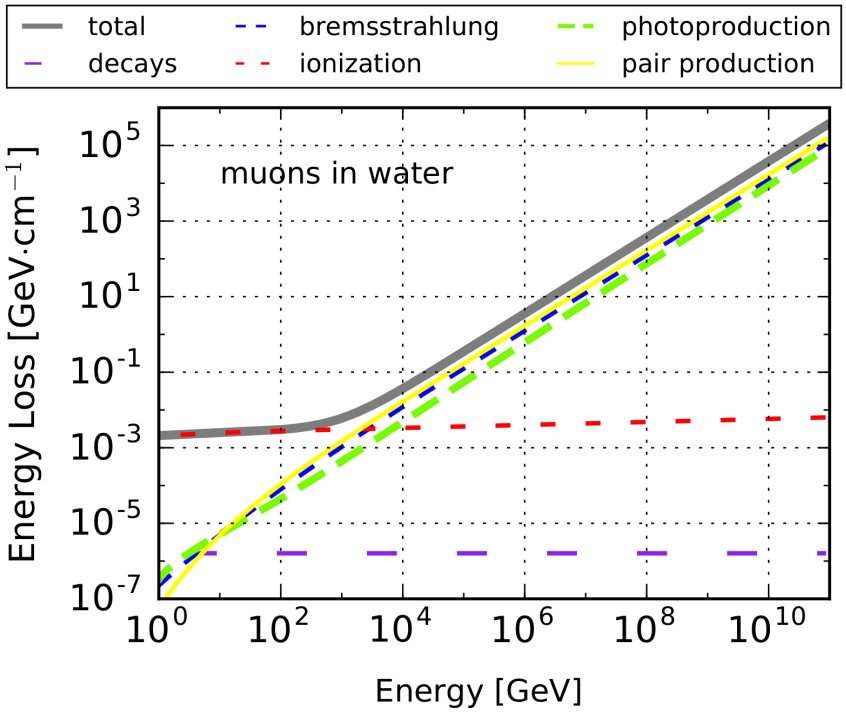

Figure 2.14 – Muon energy losses for propagation in water. Figure taken from [44].

accurate. Several algorithms have been developed to better estimate the energy of the events, I describe here the *dEdX* algorithm which is used in chapter 6.

Track events detected by ANTARES are not contained in the detector. Therefore, most of the energy of the particles is not deposited in the detector and the neutrino energy is not easy to estimate. The dEdX algorithm uses the fact that the energy losses of muons increase with energy as can be seen in figure 2.14. However, dEdX is not efficient at energies lower than 100 GeV as the energy losses are dominated by ionisation which is constant with energy.

2.6.2 Shower Reconstruction

A detailed description of the shower reconstruction algorithm can be found in [13]. The reconstruction is divided into two algorithms, one for the position of the event, the vertex, and an other one for the direction and energy.

Position Reconstruction

As for the tracks, the algorithm start by selecting the hits causally correlated. Every pair of hits has to fulfil the criterion $\vec{r}_i - \vec{r}_j \geq v_g \cdot |t_i - t_j|$ with t_i and $\vec{r}_i$ the time and position of a hit i and v_g is the group velocity of light in water.

The estimation of the shower position is done making the assumption that all the light is emitted by a point-like source at an instant t_{Sh}. In this hypothesis, all hits should follow the

Table 2.2 – Event pre-selection.

Event Type	Criterion	Condition
Track	Upward-going	$\cos(\theta_{\text{Tr}}) < 0.2$
	Quality	$\Lambda_{\text{Tr}} >$ -6
	Error Estimate	$\beta_{\text{Tr}} < 1.5°$
	or	
Shower	Upward-going	$\cos(\theta_{\text{Sh}}) < 0.2$

relation $(\vec{r}_i - \vec{r}_{\text{Sh}})^2 = v_g^2 \cdot (t_i - t_{\text{Sh}})^2$. This system of equation is linearised and solved using the linear least square fit method [57].

This is used as a starting point for the M-estimator (M_{Est} in chapter 6) fit which is a modified χ^2 minimizing the residual time and accounting for the amplitude of the hits [13]. The residual time is defined as $t_{\text{res}\,i} = t_i - t_{\text{Sh}} - |\vec{r}_i - \vec{r}_{\text{Sh}}|/v_g$ for a hit i.

Direction and Energy Reconstruction

The direction and energy reconstruction is performed with a likelihood function which accounts for the probability of each hit to come from the shower or the optical background. The probability that an unhit optical module does not see light is also used. These probabilities depend on the shower characteristics, therefore the likelihood is maximized by fitting the energy and direction. This estimated energy will be used is the following of this work, it will be called E_{TANTRA} in chapter 6.

An estimator of the angular error is also computed. After the direction has been fitted, the likelihood landscape around the fit is scanned by increasing the angular distance to the best fit direction by steps of one degree. The angular distance which decreases the log-likelihood value of more than one in respect to the best fit value is taken as angular error.

As for tracks, the number of hits selected for the reconstruction (N_{hits}) can also be used as an energy estimator.

2.6.3 Pre-selection

Both reconstructions are applied on each event, then a pre-selection is applied before writing events to the data files used in the upward-going analyses as the one presented in part II. The pre-selection conditions are given in table 2.2. The zenith θ is defined in figure 2.15, θ_{Tr} and θ_{Sh} being the reconstructed zenith from the track and shower algorithms respectively.

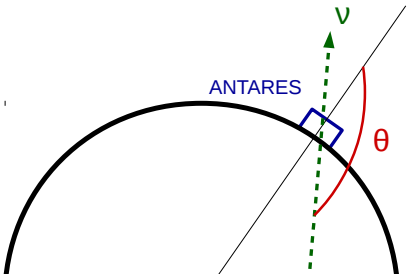

Figure 2.15 – Definition of the zenith θ. The green arrow is the direction of the neutrino and the black line the vertical axis of the detector.

Chapter 3

Other Neutrino Telescopes

The other neutrino experiments which took part to the follow-up of the gravitational wave event GW170817, IceCube and Pierre Auger, are presented in this chapter as well as KM3NeT, the successor of Antares.

The Gigaton Volume Detector in Lake Baïkal (Baïkal-GVD) [58] is the only neutrino telescope not presented as not being part of the GW170817 follow-up. However, it is larger than Antares since few months and we can hope it will join the gravitational wave follow-up for the next observation run.

3.1 The IceCube Experiment

The IceCube experiment [59] relies on the same detection principle as Antares, however the two detectors are distinct and complementary.

IceCube is much larger than Antares with a total instrumented volume of about 1 km^3 and it is located in the deep ice of the South Pole glacier. The smaller absorption length in ice than in water leads to a better energy resolution than Antares, while the larger diffusion degrades the angular resolution, and its location in the South pole gives to IceCube a good visibility of the Northern hemisphere which is complementary with the Antares one. IceCube can also exploit downward-going events by selecting contained events at the price of a smaller effective area. The detector is also covered by IceTop as can be seen in figure 3.1, which is an array of Cherenkov detector tanks that measures atmospheric showers occurring on top of the detector. It is used to reject the vertical atmospheric muons, and is also one of the leading experiment in the study of very high energy cosmic rays in the so-called knee region [60]. The optical background is almost inexistant since there is no ^{40}K and bioluminescence. More details on the layout can be found in figure 3.1.

In the coming years, IceCube should be extended by IceCube-Gen2. IceCube-Gen2 should be a less dense but ten times larger array surrounding IceCube, increasing by one order of magnitude the effective area at high energies.

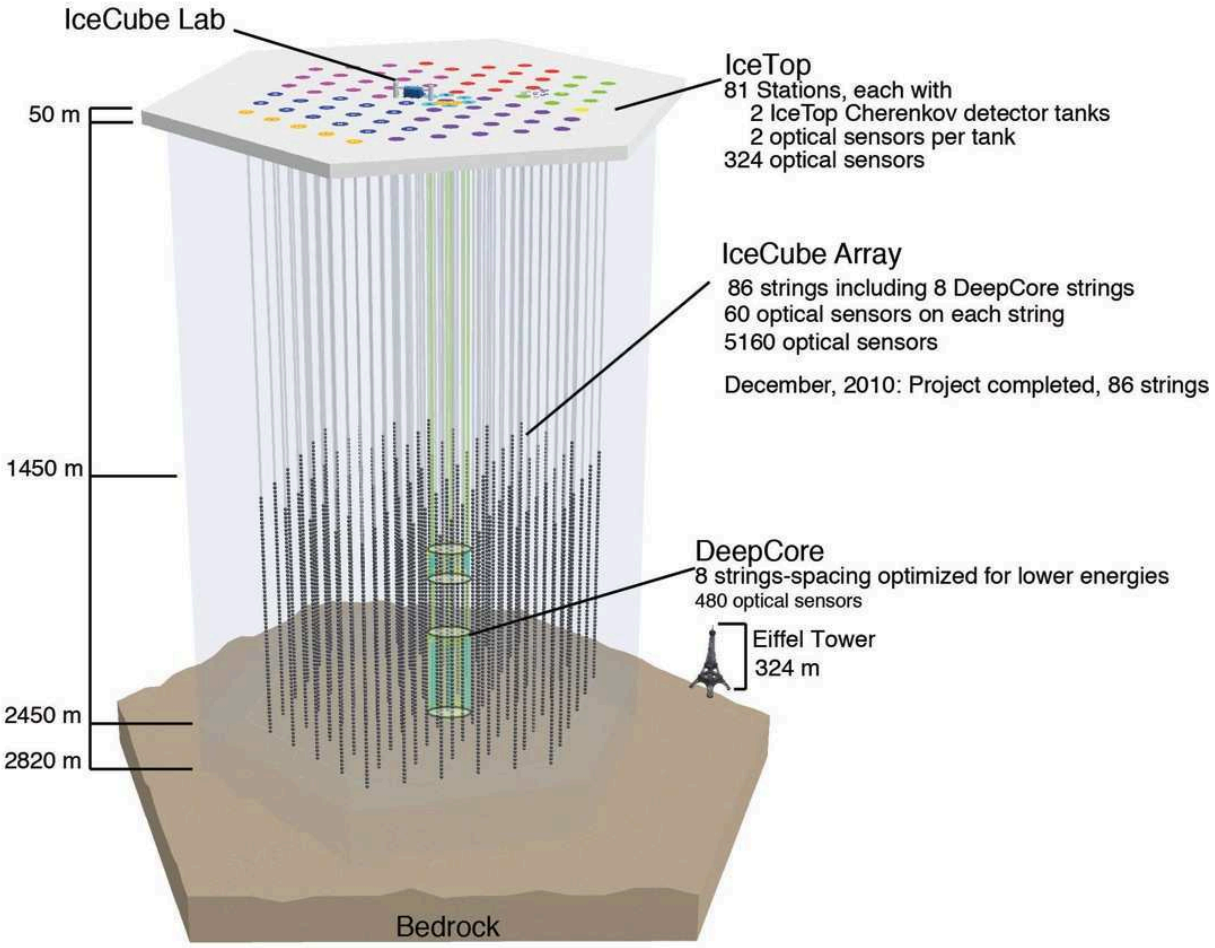

Figure 3.1 – Schematic view of the IceCube detector layout.

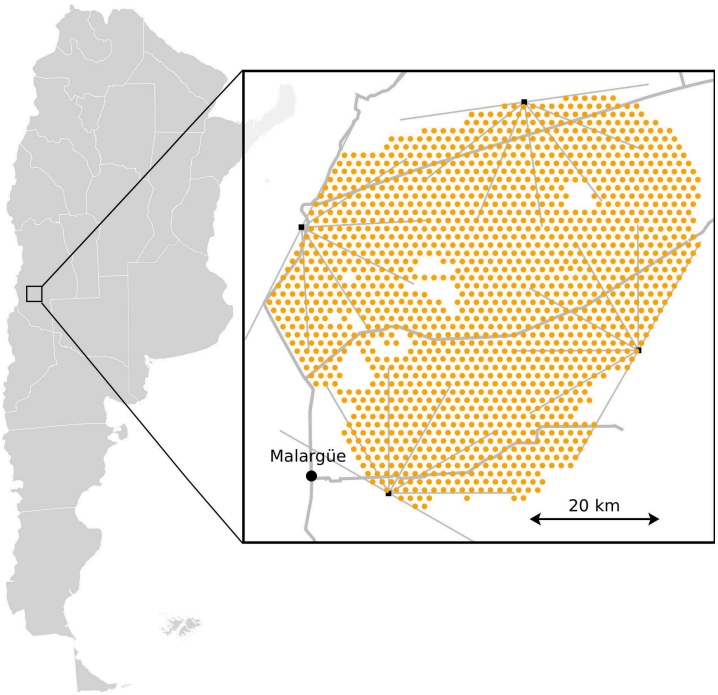

Figure 3.2 – Location and layout of the Pierre Auger detector. The water Cherenkov stations (orange dots) form the surface detector array while the four fluorescence buildings (black squares) form the fluorescence detector.

3.2 The Pierre Auger Observatory

The Pierre Auger Observatory [61] has been built in order to measure the ultra-high-energy cosmic ray flux at Earth. However, it can also be used to detect ultra-high-energy neutrinos from cosmic origin.

The Pierre Auger Detector Layout

Auger is located in Argentina at an altitude of 1 420 m in order to profit from the optimal air shower development. As can be seen in figure 3.2, Auger is composed of an array of 1 660 water Cherenkov stations covering a surface of 3 000 km², the *surface detector*, and four stations housing six fluorescence telescopes each, the *fluorescence detector*.

Only the surface detectors are used for the neutrino detection. The picture of a water Cherenkov station of the surface detector is shown in figure 3.3. These tanks are filled with water and contain three photomultiplier tubes each, in order to detect Cherenkov light produced by muons and electrons of the extensive air showers.

Neutrino Detection Principle of the Pierre Auger Observatory

Like cosmic rays, neutrinos interacting within the atmosphere produce air showers. The main challenge of the neutrino detection with Auger is to distinguish neutrinos from cosmic rays.

Figure 3.3 – Water Cherenkov station. It contains 12 000 liters of pure water and three photomultiplier tubes.

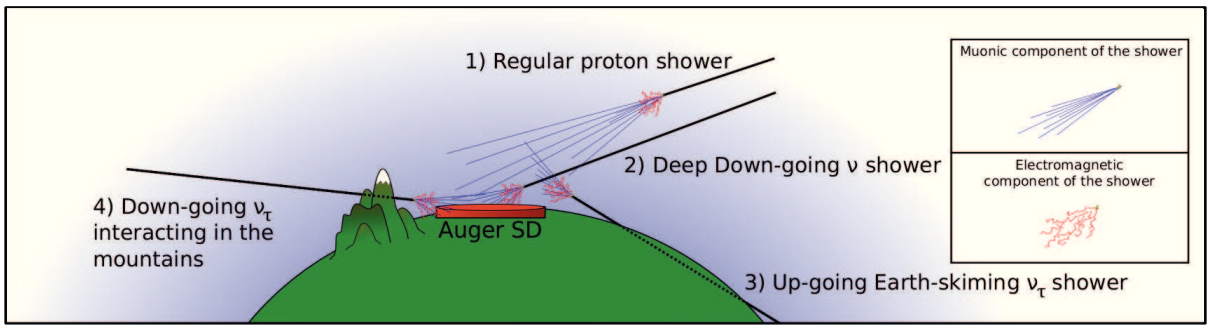

Figure 3.4 – Detection principle of neutrinos with the Pierre Auger Observatory. Horizontal regular proton showers (1) are seen as dominated by muons at the surface detector (in red), while the amount of electromagnetic component is important for the deep downward-going neutrino showers (2) or the showers from Earth-skimming ν_τ (3) and ν_τ interacting in the mountains (4).

These two types of particles can be distinguished from the deepness of the interaction within the atmosphere. Indeed, cosmic rays always interact shortly after entering the atmosphere while neutrinos can interact deeply [62]. If the interaction occurred close enough to the detector, the shower still have a considerable amount of electromagnetic components when reaching the surface detector. These events are called *young* showers. It is the case for vertical cosmic rays interacting on top of the detector. But for cosmic ray induced showers that are close to the horizontal, the *old* shower front is dominated by muons as represented in figure 3.4.

Thereby, horizontal young showers will be recognised more easily as resulting from neutrino interactions. From this idea, two type of events, illustrated in figure 3.4, can be distinguished:

- *Earth-skimming* events are events induced by ν_τ travelling in the upward direction close to the horizontal. If the neutrino interacts with the Earth relatively close to the surface, the tau produced can escape the Earth, decay in flight and induce a shower in the atmosphere close to the detector.

  Earth-skimming events can be identified if they have a zenith angle in the range $90° < \theta < 95°$.

- *Downward-going* neutrinos close to the horizontal can interact in the atmosphere close to

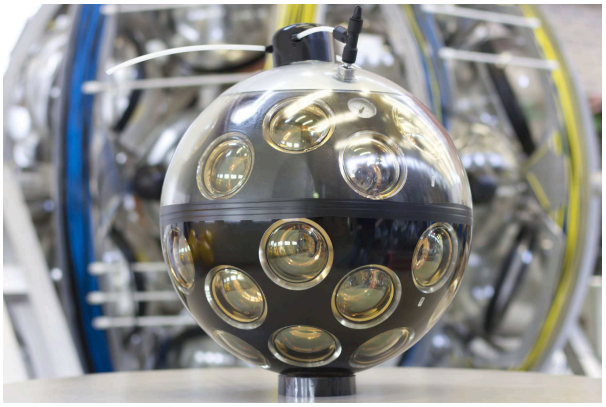

Figure 3.5 – Photograph of a KM3NeT digital optical module.

the detector. They have a zenith angle in the range $75° \leq \theta \leq 90°$.

A ν_τ interacting in the mountains surrounding the Pierre Auger Observatory can also produce a tau which can decay close to the detector. This is equivalent to an Earth-skimming event but it cannot be distinguished from other downward-going events.

3.3 Outlook of the KM3NeT Detector

The **km³ N**eutrino **T**elescope (KM3NeT) [63] is the successor of ANTARES. It will be formed of building blocks of 115 lines, each line housing 18 digital optical modules. For KM3NeT the optical modules have been improved compared to the previous generation telescopes. Each module houses 31 3-inch photomultiplier tubes as shown in figure 3.5 and digitisation electronics. This new design will allow to better reject the background and a better event reconstruction.

KM3NeT will be divided in two parts dedicated to different physics, ARCA (**A**stroparticle **R**esearch with **C**osmics in the **A**byss) for high energy astrophysics and ORCA (**O**scillation **R**esearch with **C**osmics in the **A**byss) for neutrino oscillation studies. An artist view of KM3NeT is represented in figure 3.6. The phase 2 of the project is presented here, a third phase with a total of six building blocks is expected on a longer time-scale.

ARCA will be a km³ scale telescope in the Mediterranean sea off coast of Sicily at a depth of 3 500 m. It will be made of two building blocks with 90 m inter-line spacing and a vertical spacing between optical modules of 36 m.

ORCA is optimized for the GeV scale energies. It will be made of one denser block with 20 m inter-line and 9 m inter-module spacing. ORCA plans to use atmospheric neutrinos in order to determine the neutrino mass hierarchy and to measure the θ_{23} neutrino mixing angle with improved precision. It will also have some potential for low energy astrophysical signals like supernova or gamma ray bursts. It will be located close to the ANTARES site. The ORCA performances will not be detailed here but the interested reader can refer to [63].

Three KM3NeT lines have already been deployed and the deployment of the ORCA and two ARCA building blocks should end in 2022.

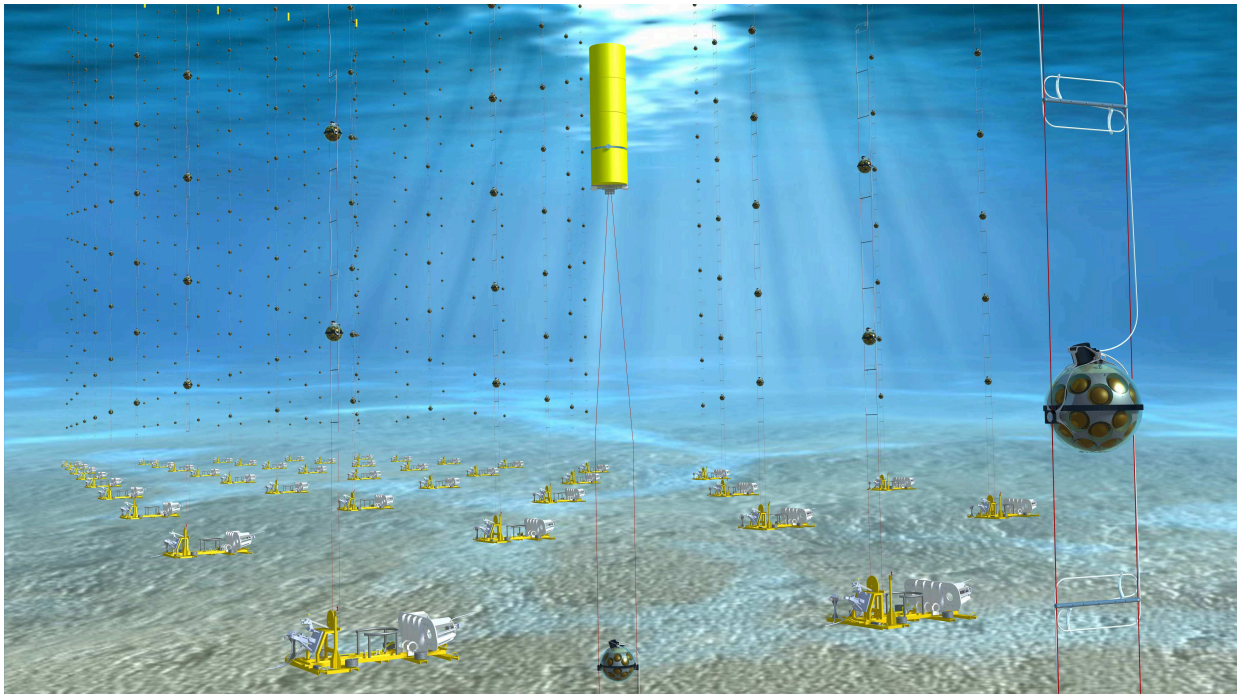

Figure 3.6 – Artist view of the KM3NeT detector.

Prospects for ARCA

The excellent angular resolution of ARCA combined to its huge volume and good coverage of the central part of the Milky Way will allow unprecedented results. We present quickly here the sensitivity studies for a diffuse Galactic neutrino flux and point sources. This allows to compare the results presented in this thesis with the KM3NeT capabilities, moreover these subjects also correspond to the sources for which ARCA has been optimized.

A KM3NeT sensitivity study has been performed looking for a Galactic diffuse flux [64] per neutrino flavour of $5 \cdot 10^{-6} \left(\frac{E_\nu}{1\,\text{GeV}}\right)^{-2.3} \times \exp\left(-\sqrt{\frac{E_\nu}{1\,\text{PeV}}}\right)$ $\text{GeV}^{-1}\,\text{cm}^{-2}\,\text{s}^{-1}\,\text{sr}^{-1}$ from the Galactic center region $|b| < 4°$ and $|l| < 30°$. This flux prediction comes from the KRAγ model [36], the one which is presented and analysed with ANTARES and ICECUBE data in the part II of this thesis. This analysis uses a likelihood ratio method using the events energy and their estimated signalness from a multivariate analysis. As can be seen in figure 3.7, ARCA has a 50 % probability to make a 5σ discovery of this flux in four years independently for tracks and showers. Moreover, we can stress that this analysis does not account for the model morphology, therefore an analysis combining tracks and showers and accounting for the model morphology could improve these results.

A sensitivity study to Galactic sources has also been done with some of the most powerful Galactic γ-ray sources [65]. Their expected neutrino fluxes have been derived from the γ-ray data under the assumption that the γ-ray flux has a fully hadronic origin. These fluxes are

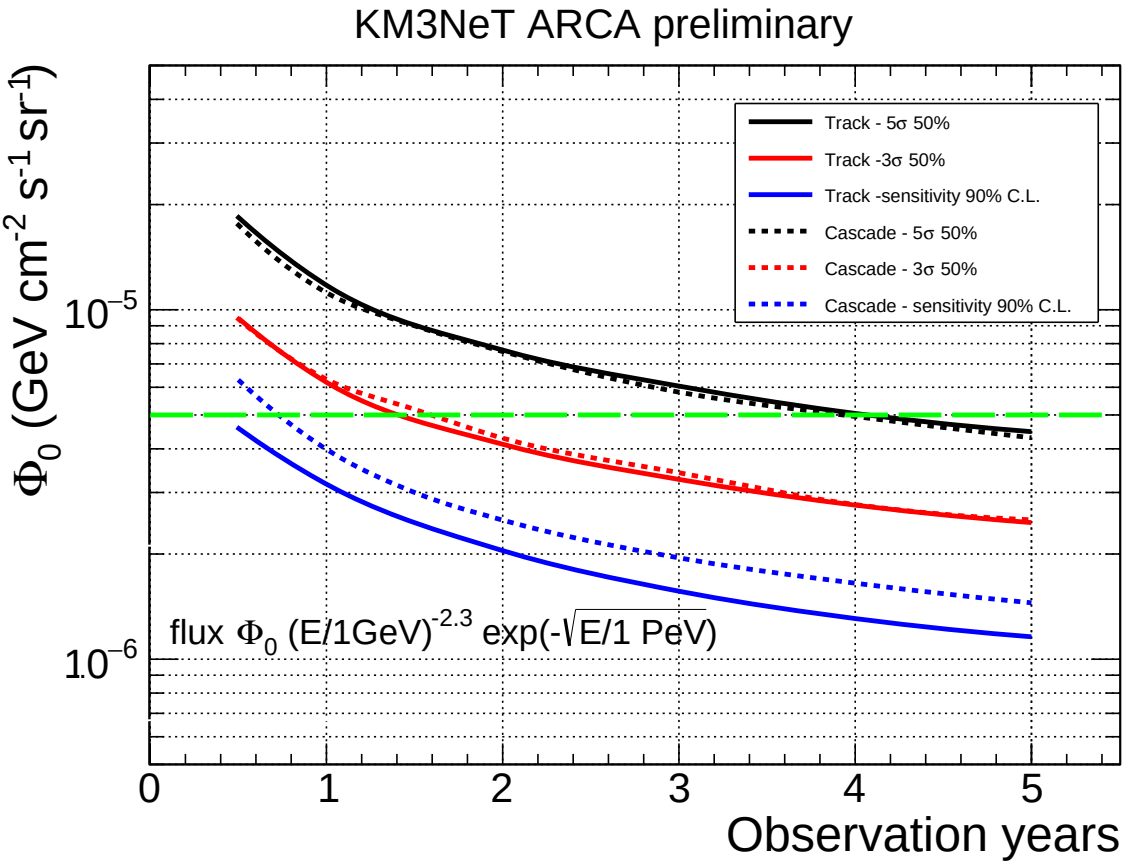

Figure 3.7 – KM3NeT Galactic Plane study. 5σ (black) and 3σ (red) discovery fluxes as well as the sensitivity (blue) to a diffuse neutrino flux from a selected region of the Galactic Plane as a function of the ARCA observation time. Both the track (solid lines) and shower (dashed lines) samples results are presented.

Table 3.1 – Flux parameters of the Galactic point sources studied in [65]. The flux is expressed according to equation 3.1 with Φ_0 in units of $10^{-11}\,\mathrm{TeV}^{-1}\,\mathrm{s}^{-1}\,\mathrm{cm}^{-2}$.

Source	δ	Extension	Φ_0	Γ	E_{cut}	β
RX J1713.7−3946 (1)	-39.77°	0.6°	1.68	1.72	2.1	0.5
RX J1713.7−3946 (2)	-39.77°	0.6°	0.89	2.06	8.04	1
Vela Jr	-46.36°	1°	1.30	1.87	4.5	1
HESS J1614−518 (1)	-51.82°	0.42°	0.26	2.42	-	-
HESS J1614−518 (2)	-51.82°	0.42°	0.51	2	3.71	0.5
Galactic Centre	-28.87°	0.45°	0.25	2.3	85.53	0.5

described by

$$\Phi_\nu(E) = \Phi_0\, E^{-\Gamma} \exp\left(-(E/E_{\mathrm{cut}})^{\beta}\right)\ \mathrm{TeV}^{-1}\,\mathrm{s}^{-1}\,\mathrm{cm}^{-2} \tag{3.1}$$

with δ the declination, Φ_0 the flux normalisation, Γ the spectral index and E_{cut} the energy cutoff. The values of these parameters are given in the table 3.1. Some of the sources have two different parametrizations, denoted (1) and (2).

A multivariate analysis is used to estimate the *signalness* of the neutrino events, this signalness is then used in a likelihood ratio test. The sensitivity flux at 90 % confidence level in function of the observation time is shown in figure 3.8. For all these sources, the fully hadronic scenario can be constrained in less than five years. There is a 50 % probability to have a 3σ discovery after six years for half of these sources. However, only the track sample is exploited in this analysis, the results can be improved by adding the shower sample.

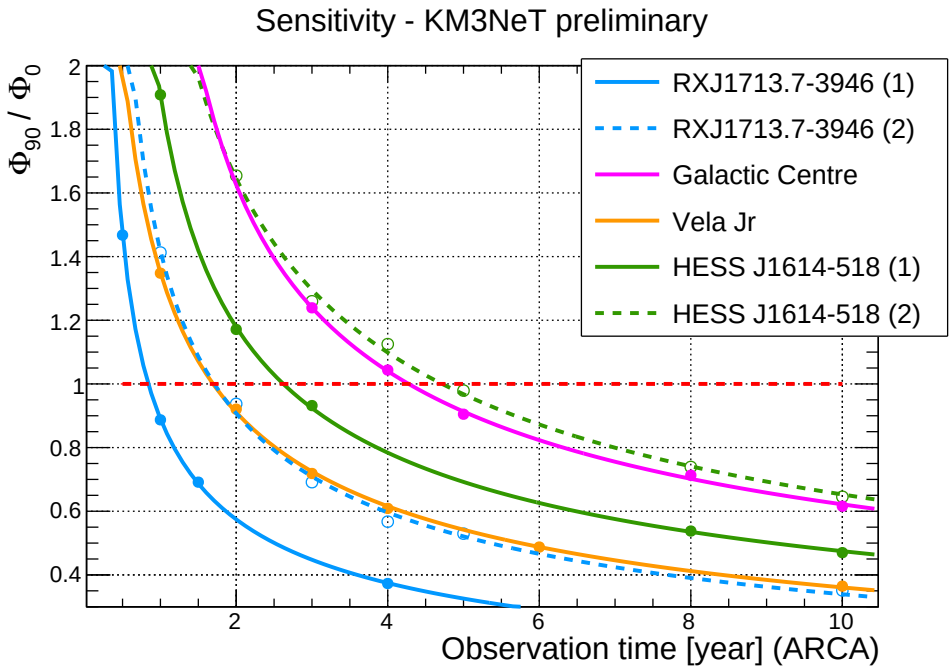

Figure 3.8 – KM3NeT point source study. Sensitivity flux at 90 % confidence level Φ_{90} divided by the normalisation flux in function of the ARCA observation time for the sources listed in table 3.1. Figure taken from [65].

Part II:

Galactic Plane Search

Chapter 4

Diffuse Galactic Neutrino Emission

The interaction of cosmic rays with the interstellar medium in the Milky Way is the source of a diffuse Galactic neutrino emission. This chapter starts by presenting the Milky Way characteristics influencing the cosmic ray propagation which is described afterwards, in order to understand this neutrino emission. Then the so-called *KRAγ* model [36, 66], studied in the following chapters, is presented as well as the associated neutrino flux prediction.

4.1 The Milky Way

In 1925, Hubble built a galaxy classification based on their morphologies [67]. This classification results in mainly three *Hubble types* as illustrated in figure 4.1. The majority of known galaxies have smooth featureless matter distribution, they are called *elliptical galaxies*, while others have spiral arms. Two third of the *spiral galaxies* are shaped with a central bar which is the case of the Milky Way. There is also few percent of irregular galaxies.

The Milky way is composed of a disk, a bulge and presumably a dark matter halo [68]:

- *The disk* contains most of the stars as well as the gas and dust populating the interstellar medium. The solar system is in the disk, located in the local Orion-Cygnus arm. It is at a distance from the Galactic center of about 8.5 kpc as shown in figure 4.3 and at 15 pc above the midplane. It is difficult to define the disk radius as we are located within the disk, however we can estimate that the apparent radius of the stellar disk is roughly 15 kpc while the gas extends to about 25 kpc. The disk width is about 1 kpc.

- *The bulge* is located around the center of the Galaxy, it corresponds to a much denser zone. It has an elongated shape (figure 4.3) extending on about 3 kpc with a width of 2 kpc as can be seen in figure 4.2.

- *The dark matter halo* has a mass ten times larger than the disk, it gravitationally holds the Galaxy together. It has an oblate spheroid shape, in other words, a flattened sphere shape. From its effect on the Magellanic Clouds, its diameter is estimated to be at least 100–120 kpc.

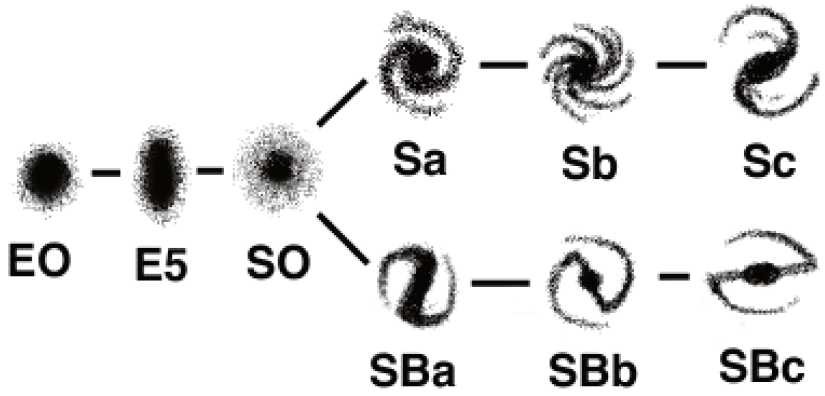

Figure 4.1 – Diagram of Hubble classification. Elliptical galaxies are denoted with a "E" and a number corresponding to their ellipticity. Spiral galaxies are denoted "S" with a letter (a, b or c) representing how tightly wound the arms are and a letter "B" if they are barred galaxies.

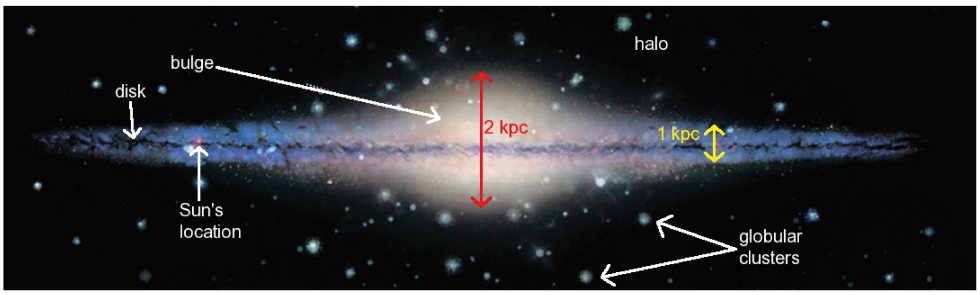

Figure 4.2 – Edge-on artistic view of the Milky Way. Figure taken from [69].

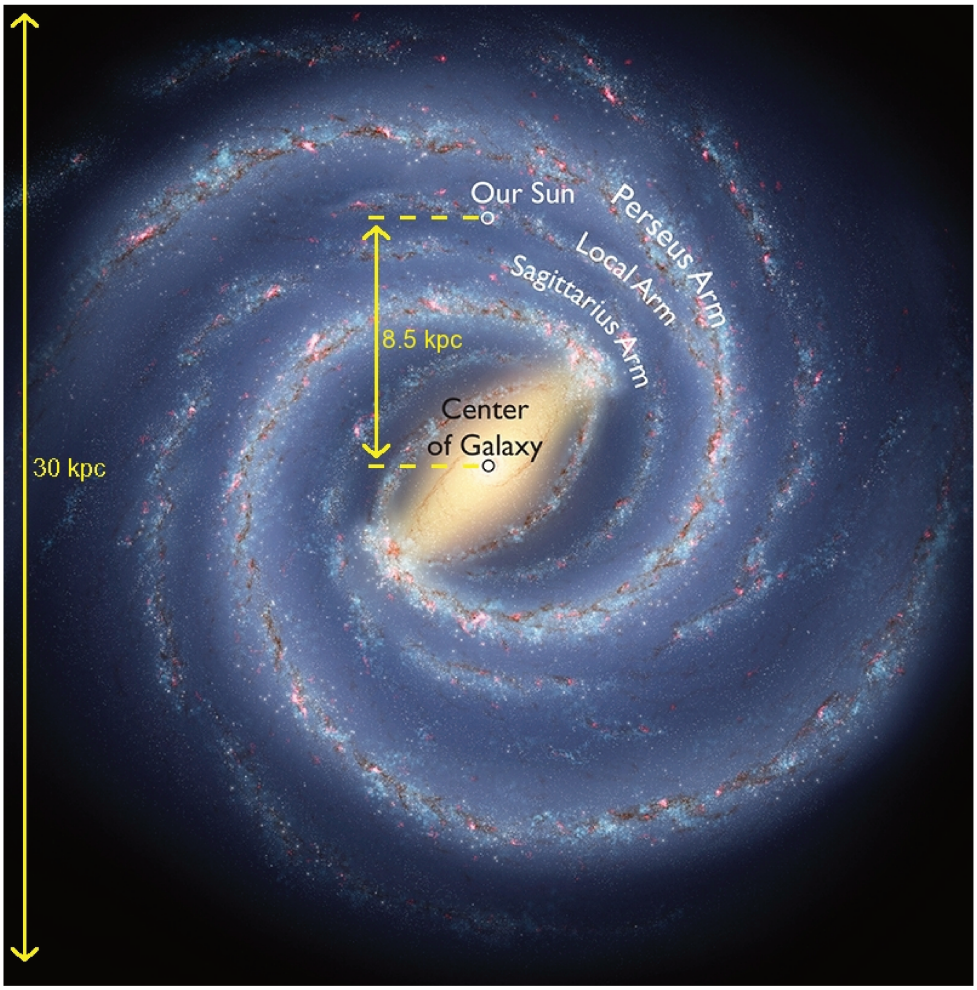

Figure 4.3 – Face-on artistic view of the Milky Way. Credit: Robert Hurt, IPAC; Bill Saxton, NRAO/AUI/NSF.

The Interstellar Medium

The interstellar medium is composed of 70.4 % (resp. 90.8 %) of hydrogen in term of mass (resp. number of nuclei) and 28.1 % (9.1 %) of helium, with only 1.5 % of heavier elements. These chemical elements are present in the form of atomic, ionized and molecular gas as well as dust. They are concentrated in the spiral arms and within the 150 pc surrounding the Galactic plane. The clouds present in the interstellar medium occupy 1–2 % of the volume but contain about half of the interstellar medium mass. The different components of the interstellar medium are described below for hydrogen as it is the most abundant element. See [70] and references therein for more details.

- *The neutral atomic gas* (denoted H_I) is present in two thermal phases, the cold phase with temperatures of 50–100 K and the warm one at 6 000–10 000 K. The cold phase is located in dense clouds (called H_I regions) with 20–50 hydrogen atoms per cm³. Located in the *inter-cloud medium*, the density of the warm phase is much lower (~0.3 cm^{-3}).

- *The ionised gas* is due to ultraviolet radiations emitted by hot and massive stars. The free electrons and ions continuously recombine and ionise again. The equilibrium between recombination and ionisation rates determines the size of the ionised region. The ionised gas is also present in two phases, a warm one at 6 000–10 000 K and a hot one with temperatures above 10^6 K. Their densities are respectively 0.04 cm^{-3} and 0.003 cm^{-3}. The warm phase is mainly located in inter-cloud regions while the hot phase extends into the Galactic halo. Indeed, the hot ionised gas is generated by supernova explosion and stellar winds that can eject the gas on large scales.

- *The molecular gas* is located in cool (> 100 K) and dense (100–1 000 cm^{-3}) *molecular clouds* where there is a higher chance of atom meeting each other and low chance of collisional disruption. The ultraviolet flux must be low to prevent ionisation. The molecular clouds are mostly located along the spiral arms and particularly at a distance of 4–7 kpc from the Galactic center.

- *The dust* is mainly made of carbon, oxygen and silicon with a typical size of a dust particle of 0.1 to 1 µm. It represents 0.1 % of the total mass of the stars.

The Magnetic Fields

The magnetic fields in the Galaxy have a strong influence on cosmic ray propagation. They consist in two components, a regular and an irregular one. Their strengths being of the same order of magnitude, the Galactic cosmic ray propagation takes place under highly turbulent conditions.

The regular component has a local intensity of ~1.4 µG. It evolves slowly with a small radial component whose magnitude is not known and a strong azimuthal component. As viewed from the North Galactic Pole, the direction of this azimuthal component is clockwise. It is stronger toward the Galactic centre reaching ~4.4 µG at a radius of 4 kpc. The regular field is composed of two layers, one localised in the disk and the other one in the Galactic halo. The transition occurs roughly at a distance of ± 0.4 kpc from the midplane [71]. The regular magnetic field of

the Galactic halo is weaker and extends until ~1.4 kpc. It is not known if it is symmetric (forming a quadrupole) or anti-symmetric (a dipole) above and below the Galactic plane.

The irregular component has a local strength of ~5 µG, it is associated with turbulent interstellar plasma. It is also thought to consist of two layers, in the disk and halo. The strength of the disk component varies in each spiral arm and is inversely proportional to the distance to the Galactic center for radii larger than 5 kpc. The halo component decreases exponentially in the radial direction and is Gaussian in the vertical one. Its vertical extension is comparable to the halo layer of the regular magnetic field. The irregular field has a coherence length scale of typically 100 pc.

Despite being one order of magnitude weaker than in the disk, the halo magnetic field has a great influence on the cosmic ray propagation because of its extension in height.

4.2 Galactic Cosmic Ray Transport

As described in section 1.2, cosmic rays are charged particles, mostly protons. Most of them are produced in the Galaxy (except at very high energies) however their is no consensus on their origin.

Cosmic rays propagating in the Milky Way gyrate around the magnetic field lines following a circular orbit with a so-called *Larmor radius* $r_L = p/(qB)$ with p their momentum, q their charge and B the intensity of the magnetic field. Therefore, considering a Galactic magnetic field of ~3 µG, protons with energies lower than ~10^8 GeV are contained in the Galaxy.

For a given particle species, the cosmic ray transport can be described by [72]

$$\begin{aligned}\frac{\partial\Phi\left(\vec{r},p,t\right)}{\partial t} = Q\left(\vec{r},p,t\right) &+ \overrightarrow{\nabla}\cdot\left(D_{xx}\overrightarrow{\nabla}\Phi\right) \\ &- \overrightarrow{\nabla}\cdot\left(\vec{V}\Phi\right) + \frac{\partial}{\partial p}\left[\frac{p}{3}\left(\overrightarrow{\nabla}\cdot\vec{V}\Phi\right)\right] + \frac{\partial}{\partial p}\left(p^2 D_{pp}\frac{\partial}{\partial p}\frac{\Phi}{p^2}\right) \\ &- \frac{\partial}{\partial p}\left(\frac{\partial p}{\partial t}\Phi\right) - \frac{\Phi}{\tau_f} - \frac{\Phi}{\tau_d}. \quad (4.1)\end{aligned}$$

Here $\Phi(\vec{r},p,t)$ is the cosmic ray density at a position $\vec{r}$, time t and momentum p. Each term of the equation is described in more detail below.

- $Q\left(\vec{r},p,t\right)$ is the source term, including primary and secondary cosmic rays.

  Galactic cosmic ray sources, like supernovae remnants, are expected to be mostly concentrated in the Galactic disk. A more detailed description of the Galactic sources is given in [72].

  Secondary cosmic rays are produced by spallation of nuclei on the interstellar medium and by radioactive decay. This way, light elements are produced from heavier ones. Both mechanisms are described below.

- $\overrightarrow{\nabla}\cdot\left(D_{xx}\overrightarrow{\nabla}\Phi\right)$ is the diffusion term, with D_{xx} the diffusion coefficient. Cosmic rays are deflected by the irregular component of the Galactic magnetic field. This irregular compo-

nent is coherent over a scale of ~100 pc which is small compared to the size of the Galaxy, therefore cosmic rays diffuse, explaining the cosmic ray isotropy.

- $-\vec{\nabla} \cdot \left(\vec{V}\Phi\right)$ is the convection term, with $\vec{V}$ the convection velocity. Galactic winds can be due to ejecta from massive stars, supernovae or to supermassive black holes. They are observed in other galaxies and could play a role in the Milky Way too.

- $\frac{\partial}{\partial p}\left[\frac{p}{3}\left(\vec{\nabla} \cdot \vec{V}\Phi\right)\right]$ is the term for adiabatic momentum loss due to the convection, the wind speed increasing away from the disk.

- $\frac{\partial}{\partial p}\left(p^2 D_{pp} \frac{\partial}{\partial p}\frac{\Phi}{p^2}\right)$ is the diffuse re-acceleration term, also called *second order Fermi mechanism*, which is described here as diffusion in the momentum space with D_{pp} the diffusion coefficient. It is due to the magnetic reflection of cosmic rays on interstellar clouds moving in random directions, the clouds transferring their kinetic energy to the cosmic rays.

- $-\frac{\partial}{\partial p}\left(\frac{\partial p}{\partial t}\Phi\right)$ is the momentum loss term accounting mostly for ionization, bremsstrahlung, synchrotron emission and inverse Compton scattering.

- $-\frac{\Phi}{\tau_f}$ is the nuclear fragmentation term, or *spallation*, τ_f being the timescale for loss by fragmentation. It is due to inelastic collisions of nuclei with the interstellar medium, breaking heavy nuclei into lighter ones. High-energy neutrinos can also be produced in this process.

- $-\frac{\Phi}{\tau_d}$ is the term accounting for radioactive decays of unstable nuclei, τ_d being the radioactive decay timescale. As for the spallation process, light nuclei are produced when heavier unstable nuclei decay.

Equation 4.2 can be solved analytically or numerically. The numerical solution offers more accurate estimations as less simplifications are needed, moreover it allows to tune the model to match to observations. It is what has been done in the KRAγ model.

4.3 The KRAγ Model

Few models have been proposed to simulate the cosmic ray propagation in the Milky Way, most of them extrapolate the local transport properties to the whole cosmic ray confining volume [73, 74, 75, 76, 77]. In the following these models will be referred to as *conventional models*. In contrast, in the KRAγ model, radially dependent cosmic ray transport properties are used in order to better reproduce *Fermi*-LAT γ-ray data as well as the local cosmic ray observables. It is physically conceivable to have different diffusion coefficients in the Galactic center because of the stronger star forming activity and peculiar field strength and geometry.

4.3.1 Method

The KRAγ model is a phenomenological model based on a data-driven approach. Indeed, the authors noticed that the conventional models do not reproduce the high γ-ray flux measured by *Fermi*-LAT in the inner Galactic region and consequently built this model to correct for this.

The authors used the model described in [78] as a starting point. This model is similar to the conventional models as it uses a diffusion coefficient D constant as a function of the galactocentric radius R. D is defined as $D(\rho) = D_0(\rho/\rho_0)^{\delta}$ with the rigidity ρ, the scaling factor δ, D_0 and ρ_0 being constants. Then, this is modified and the final KRAγ model can be described with

- $\delta = AR + B$, a radial dependence of the scaling factor of the diffusion coefficient which saturates above $R = 11\,\text{kpc}$ in order to avoid unrealistic values. The parameters A and B are fitted on the [5 GeV, 50 GeV] energy range γ-ray data along the Galactic disk with the additional constraint to have locally $\delta(R_{\text{Sun}}) = 0.5$.

  This allows to correctly reproduce the γ-ray spectrum except at low energies where it overshoots the data, therefore an advective wind is added.

- $\frac{dV_c}{dz} = 100\,\text{km}\,\text{s}^{-1}\,\text{kpc}^{-1}$, an advective wind along the vertical axis z, with a uniform gradient in the central region of the Galaxy ($R < 6.5\,\text{kpc}$). These two values are fitted on the low-energy data $E_\gamma < 1\,\text{GeV}$. The advective wind is also motivated by the X-ray ROSAT observations [79].

- $D(z) \propto \exp(z/z_t)$ an exponential vertical dependence of the diffusion coefficient.

- a conventional halo size of 4 kpc for all values of R. It has been checked that the results do not change significantly if larger values are considered.

Then, the authors check a posteriori that the local observables are not spoiled. Only a small tuning of the normalisation of the diffusion coefficient D_0 and of the source spectral index are done [66].

To account for the maximum energy reachable by the cosmic ray accelerators, an exponential cutoff is applied in the cosmic ray spectrum. In order to match CREAM [80] and bracket KASCADE [81] and KASCADE-Grande [82] data, two values of the energy cutoff at 5 and 50 PeV/nucleon have been chosen. In the following these two versions of the model will be called KRAγ^5 and KRAγ^{50}. However, the presence of an extragalactic component in the KASCADE-Grande data seems more and more credible, therefore the KRAγ^{50} model represents an extreme tuning of the model. A new version of the KRAγ model with a cutoff at ~1 PeV should be published in the coming months.

4.3.2 Results

Finally, the KRAγ model reproduces well the *Fermi*-LAT data, as expected, in particular in the inner Galactic region. This is shown in figure 4.4 which represents the γ-ray spectrum in ($|l| < 1°$ and $|b| < 0.3°$). The hypothesis of dark matter annihilation in this part of the Galaxy, used

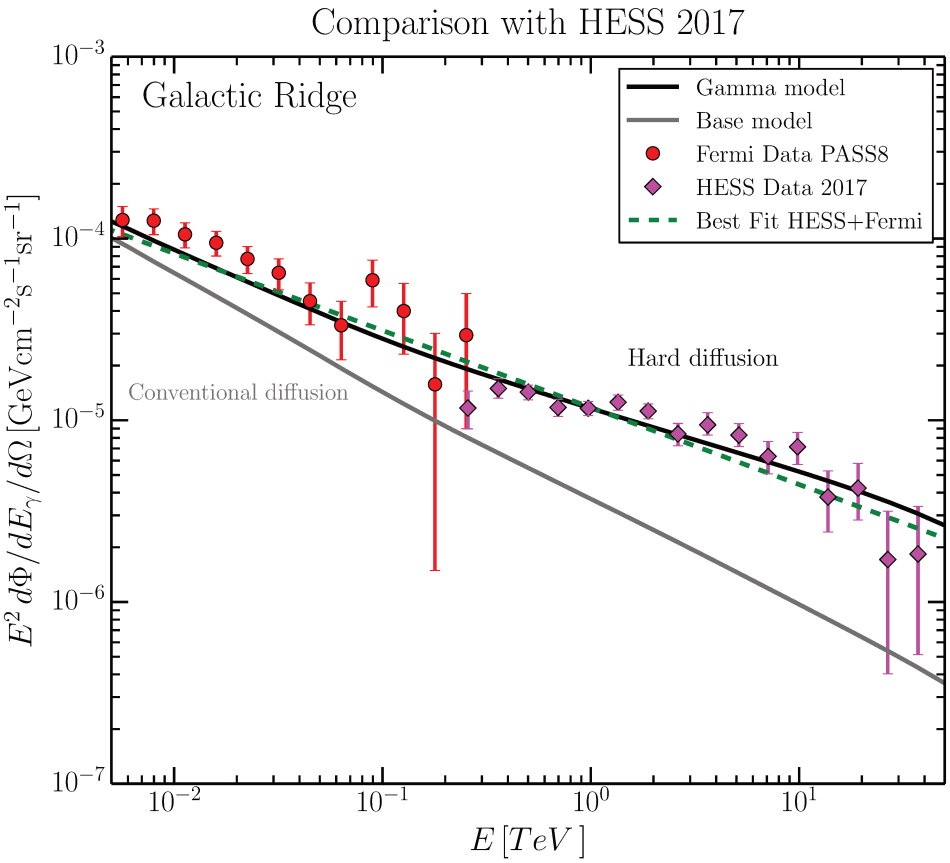

Figure 4.4 – γ-ray spectrum in the inner Galactic plane ($|l| < 1°, |b| < 0.3°$) of the KRAγ (or *Gamma* in black) model and the conventional (or *base* in grey) model. The *Fermi*-LAT PASS8 data to which the point source component has been subtracted (red) are shown as well as the HESS data from [87] (pink). The best fit of the *Fermi*-LAT and HESS data is also shown (green). At these energies the energy cutoff in the cosmic ray spectrum is not visible. Figure taken from [86].

to explain the difference between the conventional models and the data [83, 84, 85], is no more needed with the KRAγ model.

Similarly, the HESS data as seen in figure 4.4, are also well reproduced by the KRAγ model while they are not used in the fit. As for the conventional (base) model, it underestimates the data. However, in the conventional model, the HESS data from the Central Molecular Zone (CMZ) are interpreted as originating from a PeVatron, this hypothesis is not necessary with the KRAγ model as shown in [86].

The long-standing MILAGRO anomaly is also well reproduced by this model [88, 36], this anomaly is an excess with respect to the conventional models, measured by the MILAGRO experiment at 15 TeV median energy.

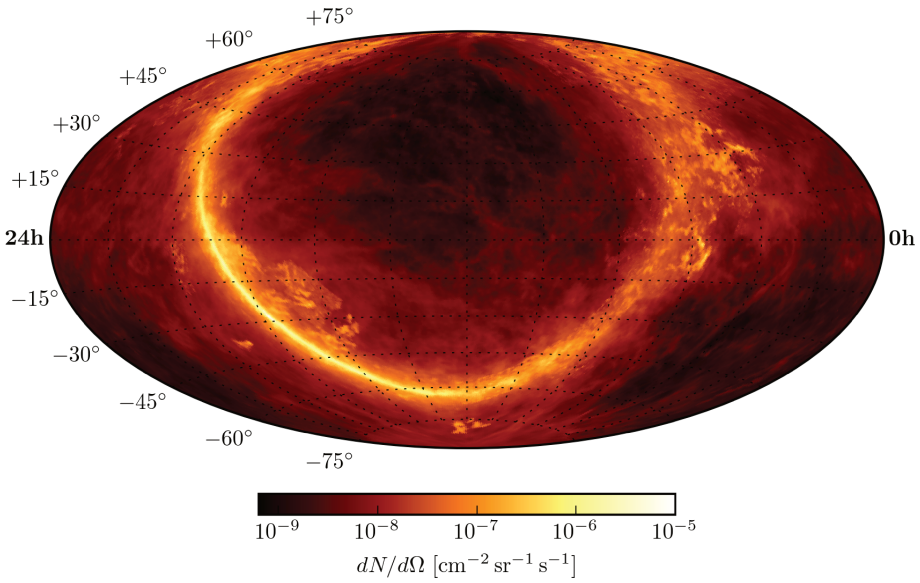

Figure 4.5 – KRAγ morphology. Hammer projection of the neutrino flux per unit of solid angle of the KRAγ[5] model in equatorial coordinates. M. Richman (IceCube) private communication.

Neutrino Flux Predictions

The diffuse neutrino flux resulting from cosmic ray propagation in the Galaxy following the KRAγ model has been computed in [36]. As the heavier species have a minor contribution, only proton and helium are considered. The ν_e and ν_μ emissivities are tuned on accelerator and cosmic ray data [89] below ~500 TeV, while an analytical parametrisation [90] is used above. As many neutrinos as antineutrinos are emitted and the neutrino oscillations almost equally redistribute the flavours.

This results in a neutrino spectrum dependent on the position in the sky with a full-sky flux higher than the conventional models of cosmic ray diffusion. In particular, a very strong neutrino emission is expected from the inner Galactic region as can be seen in figure 4.5. These results give a possible interpretation of the so-called IceCube *spectral anomaly* [27, 91]. The latter refers to a difference in the IceCube fitted spectra between the track and the High-Energy Starting Events (HESE) sample as can be seen in [32]. The track events are selected as upward-going, so they come from the Northern sky where the Galactic center is not visible while the high-energy starting events (HESE) are contained events coming from the full-sky. The difference in the fitted spectrum can be interpreted by a Galactic component of the signal. The KRAγ model having the strongest North/South asymmetry, it could explain this anomaly. However, the IceCube signal is compatible with isotropy and the presence of a Galactic component is still under debate.

The KRAγ full-sky neutrino flux prediction being higher than the conventional models, it is easier to test. However, the limit of the previous Antares search for a signal from the Galactic Ridge [92] is still above the model predictions as can be seen in figure 4.6. This search was a

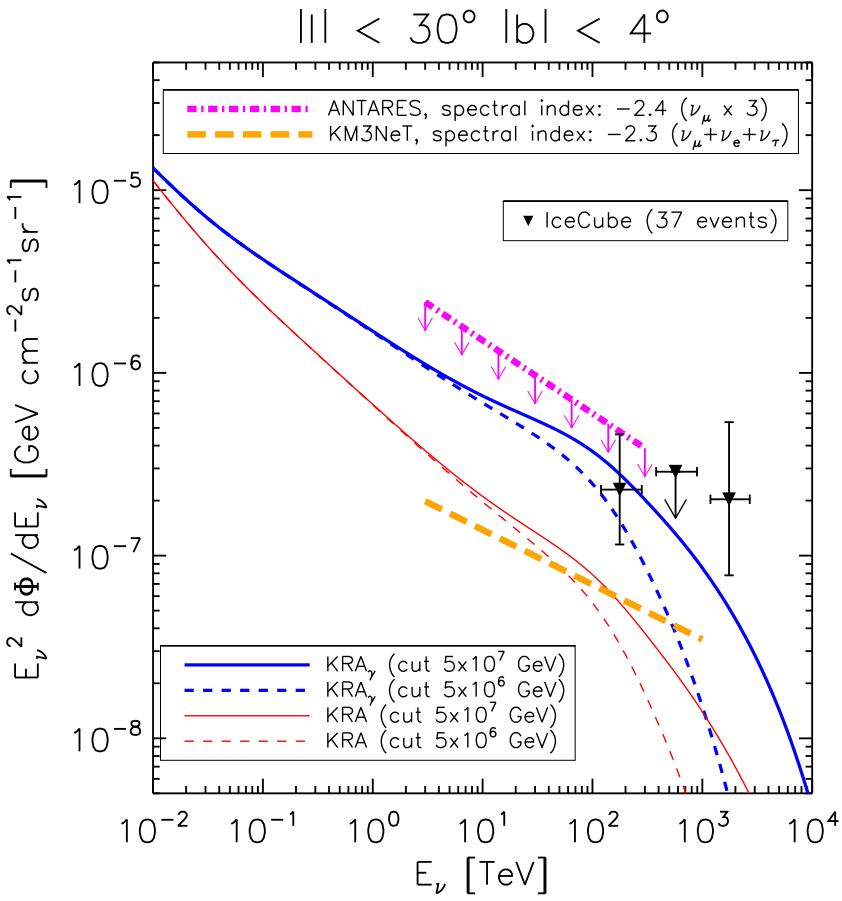

Figure 4.6 – Neutrino spectrum in the inner Galactic plane region ($|l| < 30°, |b| < 4°$) for the KRAγ^5 and KRAγ^{50} models (blue) as well as the conventional model, called KRA [78] here (red) as it is the same model but with a constant diffusion coefficient and not fitted on γ-ray data. The ANTARES upper limit from [92] is shown for comparison as well as the KM3NeT sensitivity corresponding to four years of observation time (orange). The maximal flux estimated by [93] considering three years of ICECUBE high-energy starting events is also shown (black). Figure taken from [36].

model-independent *on-off* analysis, counting the number of events in the Galactic Ridge (on-zone) in comparison with the number of events in equivalent off-zones. But the peculiar morphology of the KRAγ model peaked in the Galactic center as illustrated in figure 4.5 has not been taken into account by such on-off analysis. This is the reason why we decided to test this model with the method described in chapter 6 accounting for the morphology of the model.

Figure 4.6 also shows that the KM3NeT experiment sensitivity after four years of data taking will be well below the model flux as presented in section 3.3.

Chapter 5

Data Set

In this chapter, the ANTARES data sets used in the standalone analysis and in the combination with ICECUBE are described. They are mostly identical except for an additional year in the combination. The selection of good quality runs is the first step presented, it is followed by a comparison between data and Monte Carlo simulation to check their agreement. Then, the event selection and optimization are described.

5.1 Run Selection

For the ANTARES standalone analysis, we used data from the beginning of 2007 up to the end of 2015 and we added 2016 data to this sample for the analysis combined with ICECUBE.

The run selection aims at selecting runs with a good quality of data taking, the variables used here are detailed in section 2.4.4. In these analyses, runs with data quality equal or greater than 1 are selected. The so-called *sparking runs* are excluded as well as the *SCAN runs* that have not been recovered. On top of that, to improve the data-Monte Carlo agreement, Monte Carlo production of a certain run is used only if the corresponding data are available.

This run selection results in a total live-time of 2 404 days for the ANTARES standalone analysis to which are added 347 extra days for the combination. Annual live-times of data and Monte Carlo are shown in Table 5.1. One can see that there is around 31 % more data than Monte Carlo, the discrepancy being much smaller in recent years. This comes from computational reasons and is not problematic as the coverage of each time period is sufficient. This problem should be solved in the following months.

5.2 Data-Monte Carlo Comparison

Monte Carlo simulations are used to optimize selection cuts and to produce the ingredients of the analyses, therefore it is crucial to have a reliable Monte Carlo. This is tested by looking at the agreement between Monte Carlo and data for different cut variable distributions. The agreement of the distributions of the main quality variables before the selection cuts is presented here

Table 5.1 – Live-time and number of runs per year for data and Monte Carlo. The data-Monte Carlo live-time ratio is also presented.

Period	MC		Data		$\frac{\text{data live-time}}{\text{MC live-time}}$
	Runs	Live-time [Days]	Runs	Live-time [Days]	
2007	982	126.1	1 583	200.3	1.59
2008	1 445	131.0	2 336	213.5	1.63
2009	952	129.1	1 792	229.4	1.78
2010	1 805	178.7	2 496	244.4	1.37
2011	2 198	192.4	3 356	292.1	1.52
2012	1 782	166.9	2 750	261.9	1.57
2013	946	228.6	1 137	268.9	1.18
2014	743	297.3	848	339.7	1.14
2015	1 010	303.9	1 175	354.2	1.17
2016	1 375	356.6	1 377	356.8	1.00
Total	13 238	2 110.5	18 850	2 761.1	1.31

and the agreement after the cuts will be presented in section 5.4. A description of the quality variables Λ_{Tr}, β_{Tr} and β_{Sh} can be found in section 2.6, the muon veto, $\mathcal{L}_{\mu}$, is described in the following section. Some precuts have been applied in the track and shower samples used for the distributions shown here in order to reject the obvious muon background, they are presented in table 5.2. The parameter ρ_{Sh} being the radial distance of the reconstructed shower vertex from detector's central axis and z the height with respect to the detector centre.

Figure 5.1 shows the comparison between data and Monte Carlo for track reconstruction quality variables and figure 5.2 for the optimized shower cuts.

One can see that the data and Monte Carlo distributions before final cuts are in good agreement, therefore these variables can be used for optimisation. Only the muon veto on the shower sample does not have a good agreement on all the range, however the selection cut will be applied in a region where the agreement is still good. Moreover, the distribution after all the other cuts that will be shown in section 5.4 is in good data-Monte Carlo agreement.

The distributions of the ingredients shown in section 6.2 will also be represented with data and Monte Carlo for comparison when needed.

5.3 Event Selection

Event selection aims at improving the sensitivity of the analyses by maximizing the signal over background ratio.

Background atmospheric neutrinos cannot be distinguished from cosmic neutrinos on an event by event basis as explained in section 2.2. As a consequence the event selection focuses on rejecting atmospheric muons that are only downward-going, as a consequence upward-going events are rejected. Nevertheless, there are so many atmospheric muons, that a lot of badly

Table 5.2 – Pre-cuts used for data-Monte Carlo comparison.

Criterion	Condition
Upward-going	$\cos(\theta_{\mathrm{Tr}}) < 0.1$
Quality	$\Lambda_{\mathrm{Tr}} > -6$
Error Estimate	$\beta_{\mathrm{Tr}} < 1.5°$

(a) Track events.

Criterion	Condition
Containment	$\rho_{\mathrm{Sh}} < 300\,\mathrm{m}$, $\lvert z\rvert < 250\,\mathrm{m}$
Upward-going	$\cos(\theta_{\mathrm{Sh}}) < 0.1$
Error Estimate	$\beta_{\mathrm{Sh}} < 50$
Muon Veto	$\mathcal{L}_{\mu} > -100$

(b) Shower events.

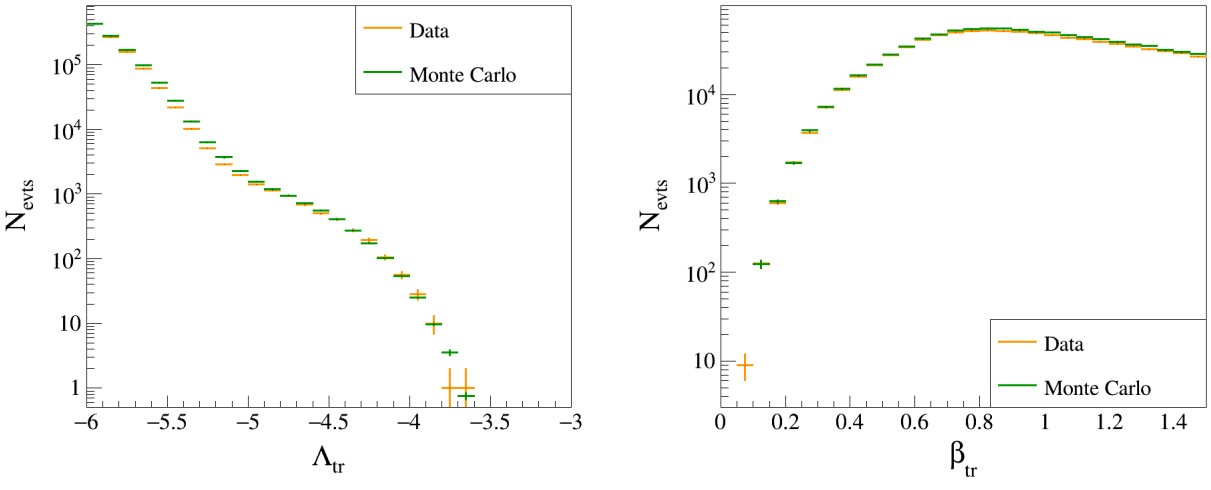

(a) **(b)**

Figure 5.1 – Distributions of Λ_{Tr} (a) and β_{Tr} (b) for data and background Monte Carlo simulations of atmospheric muons and neutrinos.

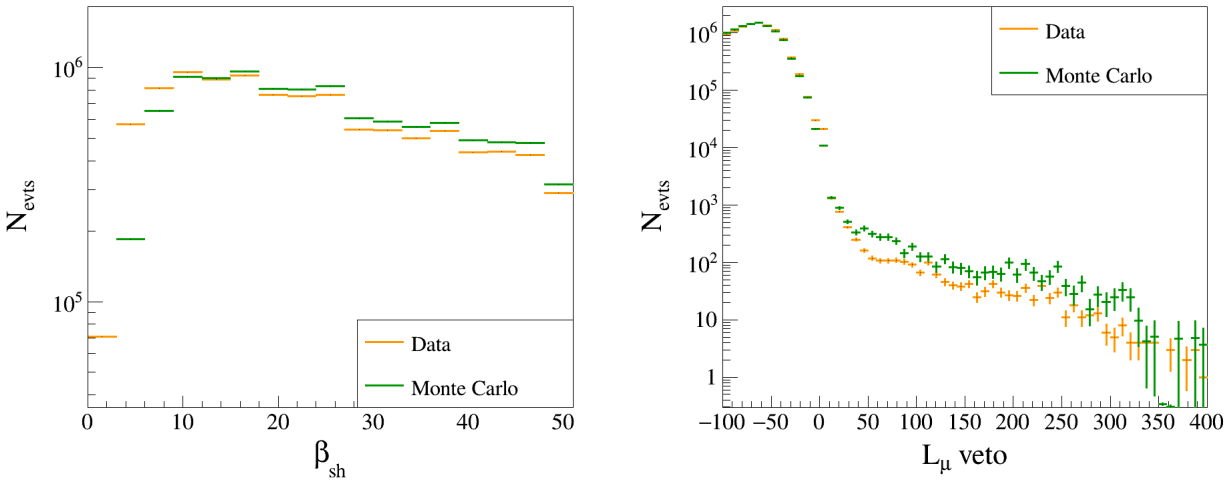

Figure 5.2 – Distributions of β_{Sh} (a) and $\mathcal{L}_{\mu}$ veto (b) for data and background Monte Carlo simulations of atmospheric muons and neutrinos.

reconstructed ones remain after this cut. To further improve the selection, we reject badly reconstructed events, this also improves the angular and energy resolution of the reconstructed events, but rejects some signal. So we optimize the cut on the reconstruction quality in order to find the best trade-off.

5.3.1 Track Selection

The track selection presented here is adapted from the track-only point source search [94].

From Monte Carlo simulations, we estimate that after the precuts described in section 2.6.3, the track sample contains a total of only 61 signal events, with 65 000 atmospheric neutrinos and 173 millions of atmospheric muons. This corresponds to a background event every two seconds and a signal event every two months. At this stage the signal over background ratio is $4{\cdot}10^{-7}$.

Table 5.3 shows the proportion of events remaining after each cut. The Monte Carlo files only contain pre-selected events as described in section 2.6.3. To reject most of the atmospheric muon background, events should be reconstructed as upward-going, i.e. with $\cos(\theta) < 0.1$, θ being the zenith angle defined as the angle between the *incoming* direction of the neutrino (the source direction) and the vertical axis of the detector as illustrated in figure 5.3. Events in $0 < \cos(\theta) < 0.1$ are downward-going events close to the horizon that are selected too. Indeed, adding this direction increases the background of only ~5 % as well reconstructed atmospheric muons are not expected from this part of the sky and the signal of ~5 % too, as it corresponds to a large solid angle.

The selection also requires a high value of the quality parameter (Λ_{Tr}) and a low value of the angular error estimate (β_{Tr}) in order to reject badly reconstructed atmospheric muons. Atmospheric neutrinos are also rejected by these cuts more often than signal events as shown in table 5.3. Indeed, having a spectrum softer than cosmic neutrinos, the corresponding tracks are

Table 5.3 – Efficiencies of each cut on atmospheric muons ($\varepsilon_{\mu}^{\text{Atm}}$), neutrinos ($\varepsilon_{\nu\to\text{any}}^{\text{Atm}}$), cosmic neutrinos giving muon tracks ($\varepsilon_{\nu\to\mu}^{\text{KRAγ}^5}$) and showers ($\varepsilon_{\nu\to\text{Sh}}^{\text{KRAγ}^5}$). The efficiency is defined as the ratio of the number of events passing the cuts over the number of pre-selected events, the pre-selection cuts are defined in section 2.6.3.

Criterion	Condition	$\varepsilon_{\mu}^{\text{Atm}}$	$\varepsilon_{\nu\to\text{any}}^{\text{Atm}}$	$\varepsilon_{\nu\to\mu}^{\text{KRAγ}^5}$	$\varepsilon_{\nu\to\text{Sh}}^{\text{KRAγ}^5}$
Pre-selected	see section 2.6.3	1	1	1	1
Upward-going	$\cos(\theta) < 0.1$	0.12	0.90	0.87	0.89
Quality	$\Lambda_{\text{Tr}} > -5.15$	$1.2{\cdot}10^{-5}$	0.12	0.28	$3.9{\cdot}10^{-2}$
Error Estimate	$\beta_{\text{Tr}} < 1°$	$4.4{\cdot}10^{-6}$	0.11	0.27	$1.2{\cdot}10^{-2}$

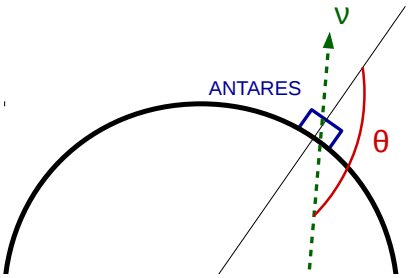

Figure 5.3 – Definition of the zenith θ. The green arrow is the direction of the neutrino and the black line the vertical axis of the detector.

less bright in average and more often badly reconstructed.

Table 5.4 displays the number of selected signal and background events in the Monte Carlo simulation from each of the channels described in section 2.1.1. A total of ~10 signal events classified as tracks are expected, mostly from ν_{μ} and ν_{τ}, with low contamination of other channels. ν_{μ} charged-current events represent 91 % of the background and 9.1 % is due to atmospheric muons.

In the end, 7 300 events selected as tracks remain in the data sample used for the ANTARES standalone analysis and 7 850 for the combination among which 10 are expected from the signal.

Table 5.4 – Remaining number of track events after the cuts for neutral current (NC) and charged current (CC) interactions for each neutrino flavours for a signal with the KRAγ^5 model characteristics and the atmospheric background.

Channel	KRAγ^5	Atmospheric
ν_{μ} NC	$2.1{\cdot}10^{-2}$	15.2
ν_{μ} CC	9.1	7 448.0
ν_{e} NC	$2.2{\cdot}10^{-2}$	0.61
ν_{e} CC	0.14	7.0
ν_{τ} CC + NC	0.92	
μ_{atm}		746.3
total	10.2	8 229.3

Table 5.5 – Efficiencies of each cut on atmospheric muons ($\varepsilon_{\mu}^{\text{Atm}}$), neutrinos ($\varepsilon_{\nu\to\text{any}}^{\text{Atm}}$), cosmic neutrinos giving muon tracks ($\varepsilon_{\nu\to\mu}^{\text{KRA}\gamma^5}$) and showers ($\varepsilon_{\nu\to\text{Sh}}^{\text{KRA}\gamma^5}$). The efficiency is defined as the ratio of the number of events passing the cuts over the number of pre-selected events, the pre-selection cuts are defined in section 2.6.3.

Criterion	Condition	$\varepsilon_{\mu}^{\text{Atm}}$	$\varepsilon_{\nu\to\text{any}}^{\text{Atm}}$	$\varepsilon_{\nu\to\mu}^{\text{KRA}\gamma^5}$	$\varepsilon_{\nu\to\text{Sh}}^{\text{KRA}\gamma^5}$
Pre-selected	see section 2.6.3	1	1	1	1
Track Veto	Not selected as a track	1.00	0.88	0.73	0.99
Containment	$\rho_{\text{Sh}} < 300\,\text{m}$, $\lvert z\rvert < 250\,\text{m}$	0.65	0.76	0.61	0.93
Upward-going	$\cos(\theta) < 0.1$	0.39	0.59	0.45	0.71
M-Estimator	$M_{\text{Est}} < 1\,000$	0.38	0.56	0.44	0.69
Error Estimate	$\beta_{\text{Sh}} < 26$	$7.1{\cdot}10^{-2}$	0.21	0.20	0.46
RDF from Dusj	$\mathcal{L}_{\text{Dusj}} > 0.3$	$4.7{\cdot}10^{-4}$	$5.4{\cdot}10^{-2}$	$6.2{\cdot}10^{-2}$	0.28
Muon Veto	$\mathcal{L}_{\mu} > 40$	$5.4{\cdot}10^{-7}$	$3.7{\cdot}10^{-3}$	$1.3{\cdot}10^{-2}$	0.10

The signal over background ratio has been improved by a factor of $\approx 4{\cdot}10^3$. More details about the final sample are given in section 5.5.

5.3.2 Shower Selection

The shower event selection cuts have been adapted from the point source search combining tracks and showers [94].

From Monte Carlo simulations, we estimate that after the precuts described in section 2.6.3, the shower sample contains a total of only 48 signal events, with 39 500 atmospheric neutrinos and 130 millions of atmospheric muons. At this stage, the signal over background ratio is roughly the same than for tracks, $4{\cdot}10^{-7}$.

The selection cuts for shower events are listed in Table 5.5 with their efficiency. One can see that much more cuts are used for showers than for tracks. Indeed, the low number of signal shower events due to the lower effective volume as explained in section 2.1.1 forces us to reduce background more than for tracks. Although background is mostly tracks, it is still hard to reject as muons radiating through bremsstrahlung can produce shower-like events in the detector. Moreover, shower direction reconstruction is less precise because of the spherical shape of the events, as a consequence it is harder to reject downward-going events.

Monte Carlo files contain only pre-selected events as described in section 2.6.3. An event reconstructed as shower is selected if it has not been selected as a track. Shower events should be contained inside of the detector to be well reconstructed: $\rho_{\text{Sh}} < 300\,\text{m}, \lvert z\rvert < 250\,\text{m}$, with ρ_{Sh} the radial distance of the reconstructed shower vertex from detector's central axis and z the height with respect to the detector centre.

As for tracks, events should be upward-going or close to horizontal to reject atmospheric muons.

As described in section 2.6, the M-estimator and β_{Sh} variables represent the quality of the reconstruction, lower they are better is the reconstruction.

Dusj Random Decision Forest In order to distinguish better atmospheric muons from cosmic showers, a random decision forest method is used based on the Dusj shower reconstruction. It uses the values of the fitted χ^2 or likelihood of the different stages of the reconstruction, more details can be found in [95].

Muon Veto An extended likelihood ratio is also used [96] to distinguish atmospheric muons from cosmic showers but using lower level informations than the random decision forest, the hits. It is defined as

$$\mathcal{L}_{\mu\text{Veto}} = \sum_{\text{hits}} \left[\log\left(P_{\text{shower}}/P_{\text{muon}}\right) + P_{\text{shower}} - P_{\text{muon}}\right]. \tag{5.1}$$

The sum is on the hits that are coincident with an other hit of the same storey within a time window of 20 ns.

The probability density functions being $P_{\text{shower}} = P(t_{\text{res}}, d, N|\text{shower})$ and $P_{\text{muon}} = P(t_{\text{res}}, d, N|\text{muon})$ with

- t_{res}, the time residual of a hit with respect to the reconstructed shower,
- d, the distance of a hit to the reconstructed shower position, and
- N, the total number of hits on-time with respect to the reconstructed shower time ($-20\,\text{ns} < t_{\text{res}} < 60\,\text{ns}$).

These probability density functions are based on Monte Carlo simulations using atmospheric muons and an E^{-2} energy spectrum for the showers. Only events reconstructed as upward-going are selected to produce these probability density functions.

The number of remaining signal and background events from each channel is shown in Table 5.6. A total of 2.57 signal showers are expected, mostly from ν_e and ν_τ producing electromagnetic showers by charged current interaction. Background is due to muon tracks from ν_μ charged-current interactions or atmospheric muons at 71 % as they are more abundant than other type of events.

In the data, 208 events persist after the selection cuts for the ANTARES standalone analysis and 218 for the combination among which 2.6 are expected from signal. The signal over background ratio has been improved by a factor of $3{\cdot}10^4$. The final sample is described in more details in section 5.5.

5.3.3 Optimization

In order to improve the sensitivity of the analysis, some of the cuts described above have been optimized. The optimization aims at improving the sensitivity which is defined as the average upper limit that could be obtained in the background-only hypothesis[1]. The variables chosen for the optimization are the ones having the biggest impact on the signal and atmospheric muons.

[1] The upper limit and sensitivity are defined with more details in section 6.4.

Table 5.6 – Number of remaining shower events after the cuts for each channel for a signal with the KRAγ[5] model characteristics and the atmospheric background.

Channel	KRAγ[5]	Atmospheric
ν_μ NC	0.16	43.5
ν_μ CC	0.33	83.7
ν_e NC	0.16	1.4
ν_e CC	1.2	17.3
ν_τ CC + NC	0.76	
μ_{atm}		68.9
total	2.57	214.9

Table 5.7 – Λ_{Tr} optimization. Number of selected tracks and showers in data, number of expected signal events and values of the average upper limit for different values of the cut on Λ_{Tr} and a constant value of the cut on β_{Sh} and $\mathcal{L}_\mu$ of 30 and 50 respectively. n_{Sh} is variable here because an event can be selected as a shower only if it has not been selected as a track. The bold line is the optimum.

Λ_{Tr} cut	n_{Tr}	n_{Sh}	$n_{\text{KRA}\gamma^5}$	Average UL	
				$[\Phi_{\text{KRA}\gamma^5}]$	$[\langle N_{\text{evts}}\rangle]$
-5.13	7 016	188	13.01	1.068	13.89
-5.15	**7 391**	**187**	**13.30**	**1.059**	**14.08**
-5.17	7 723	184	13.60	1.059	14.40
-5.20	8 373	181	14.03	1.073	15.06
-5.22	8 843	181	14.33	1.084	15.53
-5.25	9 600	175	14.76	1.074	15.85

It is Λ_{Tr} for tracks and β_{Sh} and $\mathcal{L}_\mu$ for showers, as can be seen in Tables 5.3 and 5.5. The optimization has been done for the ANTARES standalone analysis and kept as is for the combination.

The optimization is done sequentially in three steps that are represented in Tables 5.7 and 5.8, the bold line corresponding to the optimum. The first step has been to optimize the cut on Λ_{Tr}, as the track veto influences the shower sample. The value of the cut on β_{Sh} was fixed to 30 and 50 for $\mathcal{L}_\mu$ (distributions before cuts can be seen on Figure 5.2). The second step has been to optimize β_{Sh} with the same value of 50 for $\mathcal{L}_\mu$ and keeping the optimized value of Λ_{Tr}. Finally, the optimization of $\mathcal{L}_\mu$ has been done using the optimized values of Λ_{Tr} and β_{Sh}.

5.4 Data-Monte Carlo Agreement After Selection

The same distributions as in section 5.2 are represented in figures 5.4 and 5.5 after all selection cuts. The statistic is lower here, in particular for showers where not enough atmospheric muons are simulated. This results in few bins containing one or two simulated events with large weights in the shower Monte Carlo distributions. Nevertheless the agreement is very good.

Table 5.8 – β_{Sh} and $\mathcal{L}_\mu$ optimizations. Number of selected showers in data, number of expected signal events and values of the average upper limit for different values of the optimized cut. The bold lines are the optima.

β_{Sh} cut	n_{Sh}	$n_{\text{KRA}\gamma^5}$	Average UL	
			$[\Phi_{\text{KRA}\gamma^5}]$	$[\langle N_{\text{evts}} \rangle]$
22	184	13.39	1.042	13.95
26	**186**	**13.42**	**1.033**	**13.86**
30	187	13.43	1.039	13.96
34	191	13.44	1.039	13.97
38	197	13.45	1.050	14.12

(a) Optimization of β_{Sh} cut with a constant value of the cut on $\mathcal{L}_\mu$ of 50.

$\mathcal{L}_\mu$ cut	n_{Sh}	$n_{\text{KRA}\gamma^5}$	Average UL	
			$[\Phi_{\text{KRA}\gamma^5}]$	$[\langle N_{\text{evts}} \rangle]$
25	382	14.32	1.041	14.90
30	307	14.07	1.019	14.34
35	248	13.82	1.017	14.05
40	**210**	**13.62**	**1.006**	**13.70**
45	195	13.49	1.035	13.97
50	186	13.42	1.033	13.86

(b) Optimization of $\mathcal{L}_\mu$ cut.

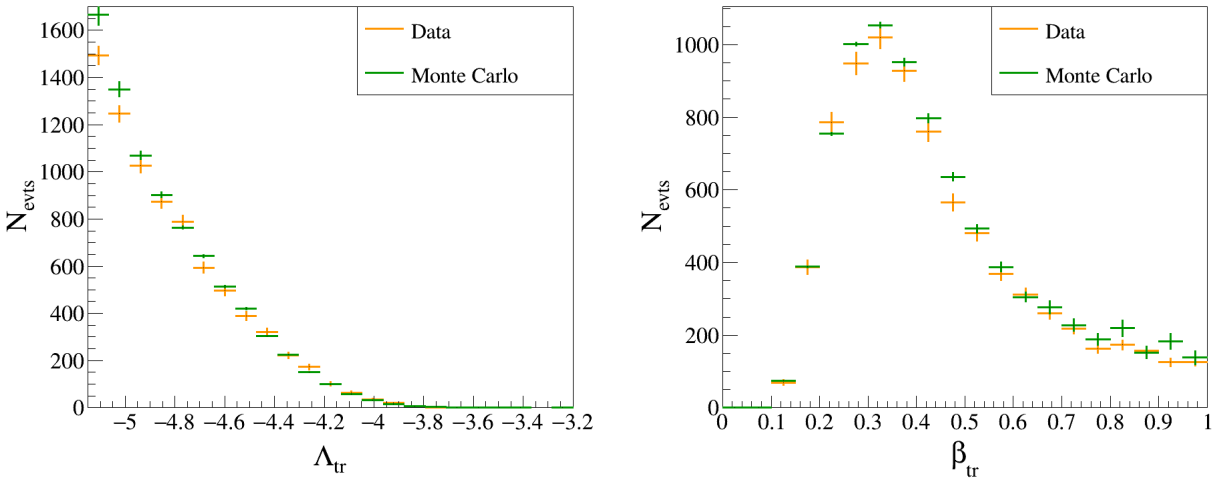

(a) **(b)**

Figure 5.4 – Distributions of Λ_{Tr} (a) and β_{Tr} (b) for data and background Monte Carlo simulations of atmospheric muons and neutrinos.

In the simulations, the total number of events is overestimated by 5% for tracks and less than 2% for shower events. This is within the atmospheric flux normalisation uncertainty. In the analysis, the normalisation of the Monte Carlo is never used, so this should have no impact.

5.5 Final Sample

A total of 18 850 runs from early 2007 to end of 2016 have been selected to form the ANTARES 10 years sample used for the combination. It corresponds to a total live-time of 2 761 days with 7 850 tracks among which 10.2 are expected from the model. Signal tracks have a very good median angular resolution of 0.5° as can be seen in figure 5.6b and an energy range of [360 GeV, 130 TeV]. This energy range is defined as the one containing 90 % of the expected signal events and is higher ([2 TeV, 150 TeV]) for the 2.6 signal showers expected among the 218 events in data. The median angular resolution of showers is 2.4° as can be seen in figure 5.6a.

The properties of the ANTARES alone sample as well as the ICECUBE track sample used for the combination are described in Table 5.9.

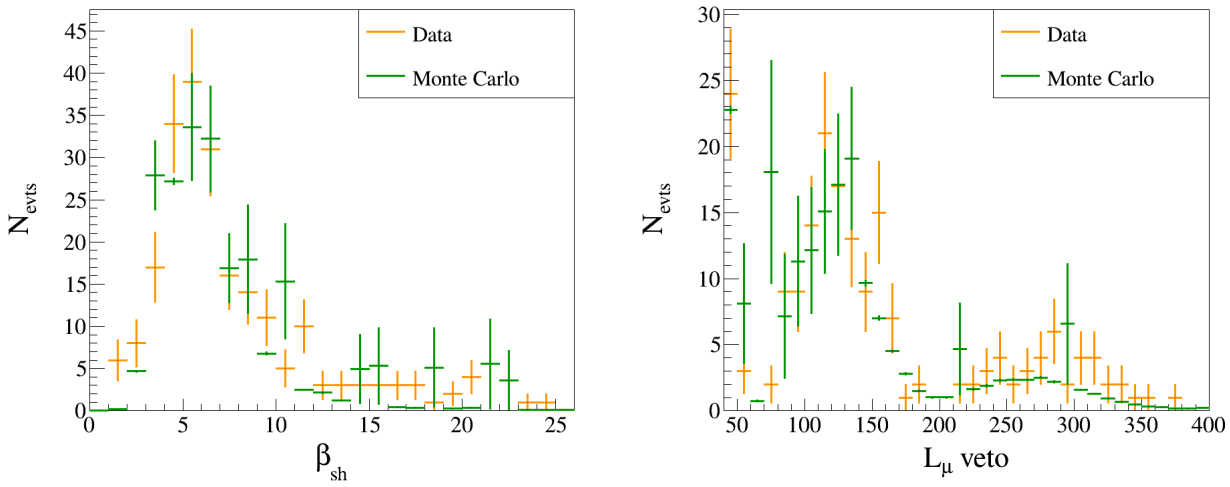

(a) **(b)**

Figure 5.5 – Distributions of β_{Sh} (a) and $\mathcal{L}_{\mu}$ veto (b) for data and background Monte Carlo simulations of atmospheric muons and neutrinos.

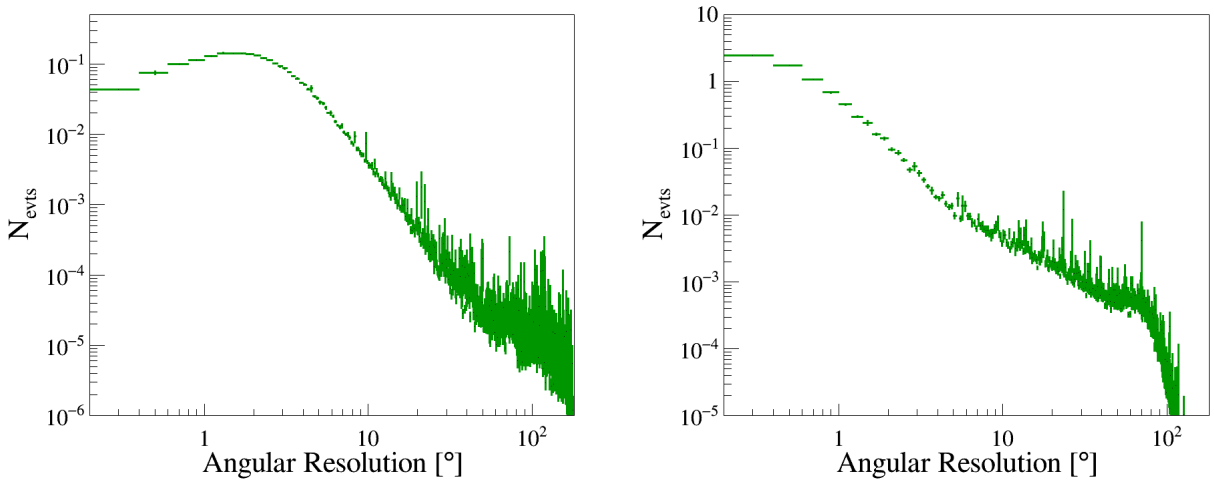

(a) Shower events. **(b)** Track events.

Figure 5.6 – Distribution of the angular resolution of signal events for tracks and showers

Table 5.9 – Properties of each event sample for both combined and independent analyses and for both versions of the model. Energy range is defined as the one containing 90 % of the events expected from the signal.

Model	Sample properties		ANTARES analysis		Combined analysis		
			Showers	Tracks	Showers	Tracks	IceCube
	Live-time [days]		2 424		2 780		2 431
	Events in data		208	7 300	218	7 850	730 130
5 PeV	Expected signal		2.3	9.3	2.6	10.2	191
	Median angular resolution		2.4°	0.5°	2.4°	0.5°	0.8°
	Energy range	Min [TeV]	2.0	0.35	2.1	0.36	0.39
		Max [TeV]	150	130	150	130	110
50 PeV	Expected signal		2.8	10.9	3.1	11.9	213
	Median angular resolution		2.4°	0.5°	2.4°	0.5°	0.7°
	Energy range	Min [TeV]	2.2	0.40	2.3	0.41	0.39
		Max [TeV]	260	230	260	230	170

Chapter 6

Search Method

In this chapter, the implementation of the likelihood function and the maximum likelihood method are detailed step by step as well as the ingredients used in the ANTARES standalone and combined analyses.

We remind that the ANTARES standalone analysis has been built independently from the ICECUBE Collaboration which was developing an equivalent analysis on its own [97]. After the ANTARES publication followed by the ICECUBE publication, we combined the two analyses. The combined analysis is very similar to the ANTARES one with few differences due to improvements (adding one year of data) or adaptation to the ICECUBE analysis. For this reason this chapter describes the method used by ANTARES for both analyses distinguishing the few elements that are different. The main differences with the ICECUBE standalone analysis are also mentioned.

Here follows a simplified overview of the maximum likelihood ratio method used.

Overview The goal of this analysis is to test the KRAγ model. More precisely it aims at estimating the probability that there is some signal with the model characteristics in the data set.

To distinguish between data with and without signal, pseudo-data samples are produced, some containing signal other not. Then, the *characteristics* of data are compared to these pseudo-data sets to see how close or distinct they are from signal and background-only hypotheses.

We have built a quantity used to compare signal and data in order to maximize the sensitivity of this analysis. This quantity takes into account most of the characteristics of the events to describe how signal-like are the data, it is an unbinned likelihood function. It evaluates the similarity of the data sample to pseudo-data containing signal. In other words, it describes how likely data contain signal, hence the name *likelihood* function. To improve even more the sensitivity, the likelihood to have some signal is weighted against the likelihood to have only background by using a likelihood ratio. This likelihood ratio is a function of the tested signal hypothesis. The amount of signal in a sample is fitted by maximizing the likelihood ratio, this maximum being used as the *test statistic* that quantifies how signal-like is the sample.

6.1 Maximum Likelihood Method

To estimate if a data set contains some signal on top of background, a likelihood function $\mathcal{L}_{S+B}$ is built. $\mathcal{L}_{\text{Tr}}$ is computed for the track sample or $\mathcal{L}_{\text{Sh}}$ for the shower one with different ingredients.

$$\mathcal{L}_{S+B} = \prod_{i=1}^{N} [n_S \cdot \mathcal{S}(\alpha_i, \delta_i, E_i) + n_B \cdot \mathcal{B}(\delta_i, E_i, \theta_i)] \tag{6.1}$$

Here $\prod_{i=1}^{N}$ is the product over all events i of the sample, n_S and n_B are respectively the number of signal and background events, with $n_B = N - n_S$, N being the total number of events. α and δ are the reconstructed equatorial coordinates, respectively right ascension and declination. E is the reconstructed energy and θ the zenith as defined in figure 5.3. $\mathcal{S}$ and $\mathcal{B}$ are the likelihood functions of an *event*[1] in the signal and background hypotheses respectively.

They are defined as

$$\mathcal{S}(\alpha_i, \delta_i, E_i) = \mathcal{A}_S(\alpha_i, \delta_i) \cdot \mathcal{E}_S(E_i, \delta_i, \alpha_i), \tag{6.2}$$

$$\mathcal{B}(\delta_i, E_i, \theta_i) = \mathcal{A}_B(\delta_i) \cdot \mathcal{E}_B(E_i, \theta_i). \tag{6.3}$$

$\mathcal{A}$ and $\mathcal{E}$ being respectively the spatial (angular) and energy probability density functions (pdfs). $\mathcal{A}_S$, represented in figure 6.1, depends on equatorial coordinates when figure 6.2 illustrates the background pdf, $\mathcal{A}_B$, which depends only on declination. Indeed, background is expected to be flat in azimuth due to the Earth rotation. As the energy spectrum of the model is position dependent, $\mathcal{E}_S$ depends on the position in the sky as represented in figure 6.3. $\mathcal{E}_B$ is shown in figure 6.4, it accounts for the dependence of energy reconstruction on the zenith angle. The distributions used for the signal come from Monte Carlo simulations while background distributions are taken from blinded data when possible. The blinding is done by randomizing the azimuth of the events using a flat hypothesis. This is a conservative approach as the signal is mixed with the background which is consequently overestimated. These probability density functions are described in more details in section 6.2.

6.1.1 Test Statistic

From now on, the likelihood to have some signal in data is estimated by $\mathcal{L}_{S+B}$. To better distinguish signal and background only hypotheses it should be weighted against the likelihood to have only background. The test statistic $\mathcal{Q}$ is built as the well known log-likelihood ratio on this purpose

$$\mathcal{Q} = \ln\left(\frac{\mathcal{L}_{S+B}}{\mathcal{L}_B}\right), \tag{6.4}$$

where $\mathcal{L}_B = \mathcal{L}_{S+B}(n_S = 0)$ is the likelihood to have only background. The use of logarithm simplifies the computations by changing products into sums.

[1] The likelihood function of an event ($\mathcal{S}$ and $\mathcal{B}$) should not get mixed up with the likelihood function of the full data set ($\mathcal{L}_{S+B}$).

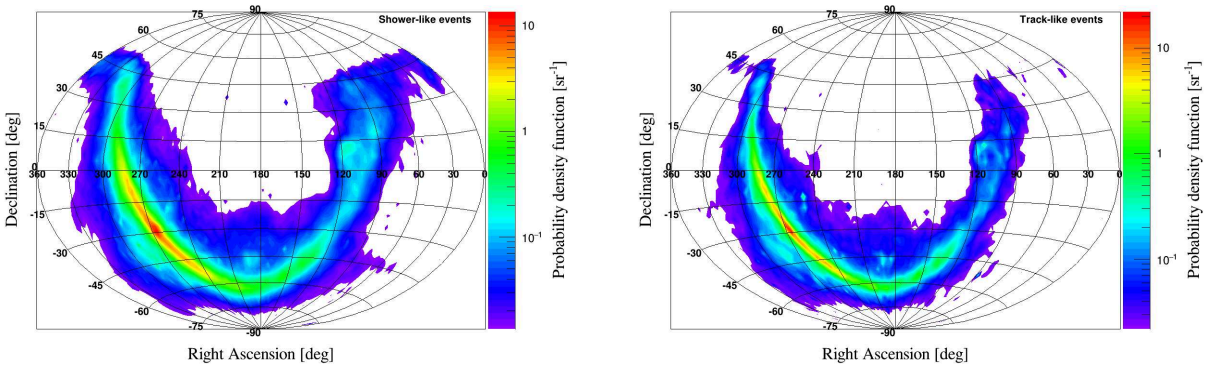

(a) Shower events. **(b)** Track events.

Figure 6.1 – Signal probability density function of the reconstructed position of the events in equatorial coordinates. It corresponds to $\mathcal{A}_S$ in the likelihood.

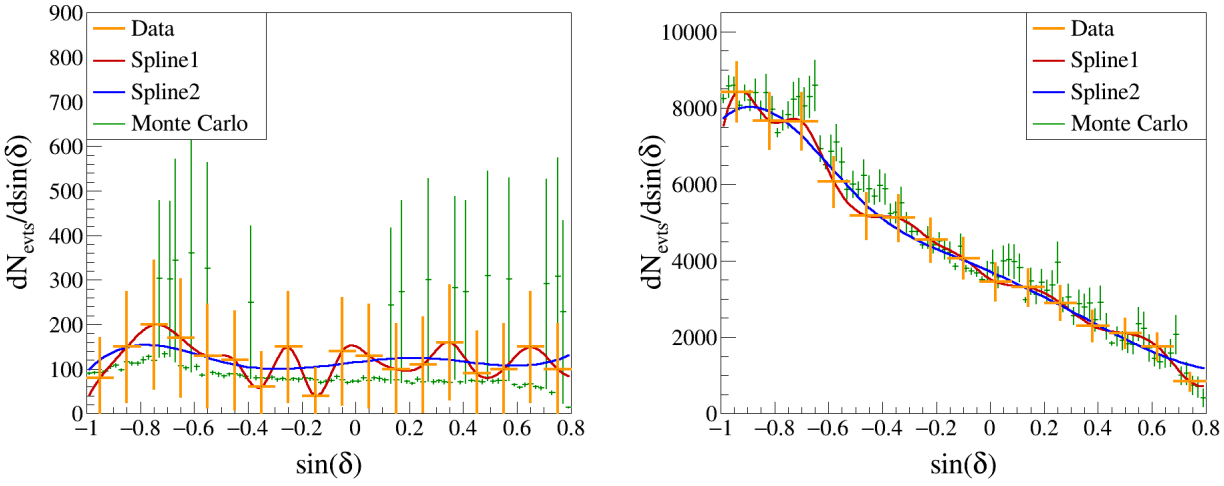

(a) Shower events. **(b)** Track events.

Figure 6.2 – Background probability density function of the sine of the reconstructed declination from data and Monte Carlo. Red and blue curves are two different spline parametrizations of data, a combination of both is used as $\mathcal{A}_B$. Peaks in these distributions are due to low statistics of the remaining atmospheric muon events that have a large weight compared to neutrinos.

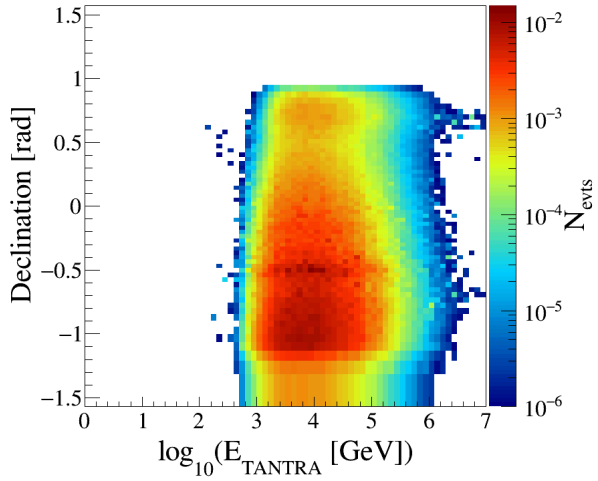

(a) Showers, declination vs. energy.

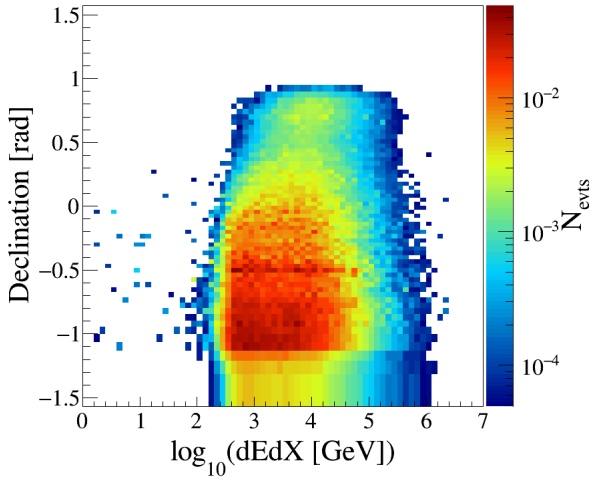

(b) Tracks, declination vs. energy.

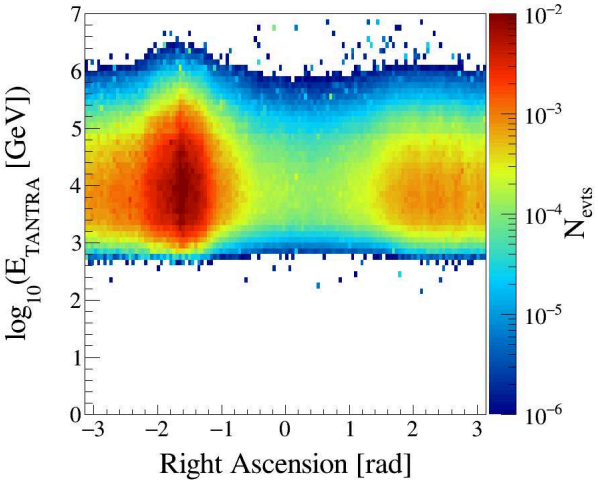

(c) Showers, energy vs. right ascension.

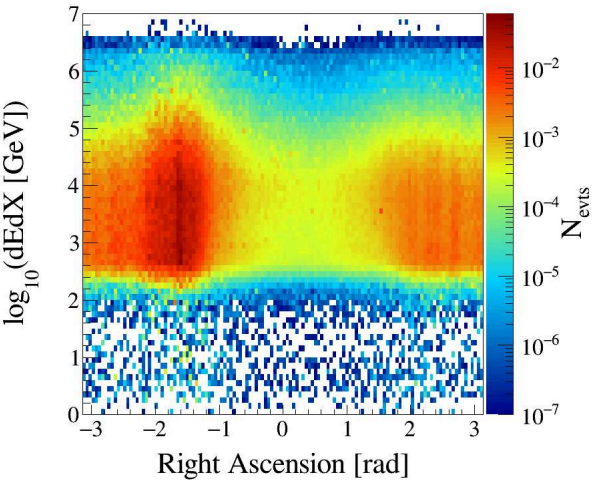

(d) Tracks, energy vs. right ascension.

Figure 6.3 – Signal probability density function of the logarithm of the reconstructed energy versus declination (left) and right ascension (right) for showers (up) and tracks (down). It corresponds to $\mathcal{E}_S$ in the likelihood.

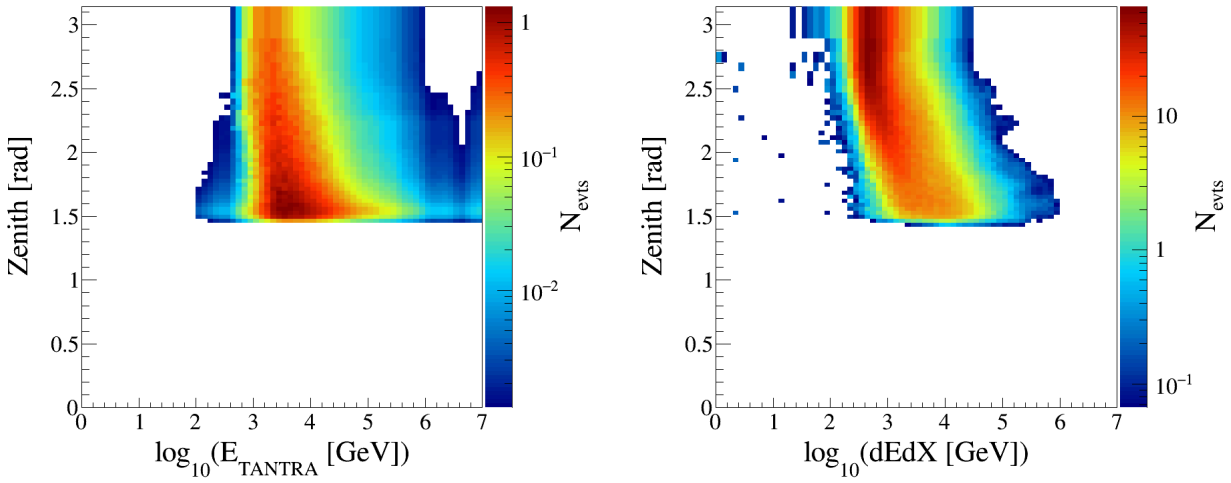

(a) Shower events.

(b) Track events.

Figure 6.4 – Background probability density function of the energy estimator versus reconstructed zenith from Monte Carlo simulations. It corresponds to $\mathcal{E}_B$ in the likelihood.

6.1.2 Signal Fit

At this point, the number of signal events n_S is missing to compute the likelihood ratio[2]. It is fitted by getting the value which is the most likely, i.e. the positive value that maximizes the likelihood.

This maximization has been done in a different manner for the ANTARES standalone and combined analyses.

ANTARES Standalone Analysis

In the standalone analysis, n_S is fitted for showers and for tracks separately, then the likelihood ratio of both data sets are added. The maximization is done using the TMinuit algorithm within the ROOT framework [98]. It can be expressed as

$$\mathcal{Q}_{\text{ANT}} = \sum_{\text{samples}} \left\{ \max_{n_S} \left(\ln \left(\frac{\mathcal{L}_{S+B}(n_S)}{\mathcal{L}_B} \right) \right) \right\}. \tag{6.5}$$

Combined Analysis

In the combined analysis, to get better results, the log-likelihood ratios of each data sets are first summed as illustrated in figure 6.5 and a unique flux is fitted for the whole data afterwards. It can be expressed as

$$\mathcal{Q}_{\text{Comb}} = \max_{\Phi_S} \left(\sum_{\text{samples}} \left\{ \ln \left(\frac{\mathcal{L}_{S+B}(\Phi_S)}{\mathcal{L}_B} \right) \right\} \right). \tag{6.6}$$

[2]Let me stress that it is the fit of n_S that allows to compute the likelihood ratio and not the contrary. $\mathcal{Q}$ is the interesting variable on which is based the analysis, not n_S.

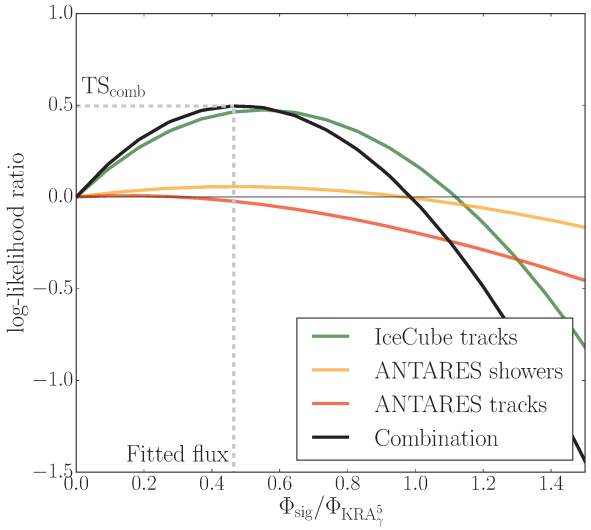

Figure 6.5 – Log-likelihood ratio curves and fitting of the flux for the combined analysis. The black curve is the sum of the three other ones. These curves correspond to unblinded data using the likelihood for the model with the 5 PeV cutoff.

In this case, the log-likelihood ratios are expressed as a function of the signal flux (Φ_S) instead of n_S which depends on the signal acceptance of each sample. It is done with a simple cross-multiplication: $\Phi_S = n_S \frac{\Phi_{\text{KRA}\gamma}}{n_{\text{KRA}\gamma}}$.

It is not the purpose of this thesis to describe the details of the IceCube part of the analysis, however the main distinctions are presented here:

IceCube's Likelihood

IceCube's likelihood is slightly different from the Antares one (equation 6.1).

$$\mathcal{L}^{\text{IC}}_{S+B} = \prod_{i=1}^{N} [n_S \cdot \mathcal{S}(\alpha_i, \delta_i, \sigma_i, E_i; \gamma) + (1 - n_S) \cdot \mathcal{B}(\delta_i, E_i)] \tag{6.7}$$

Here the spatial distributions of the signal depends on the angular resolution σ. The KRAγ spectrum is approximated by a power law with a spectral index γ chosen as the one that maximizes the sensitivity. This is because the IceCube alone paper was testing three models, the KRAγ being the only one to have a spectrum different to a simple power law. Moreover, the spectrum does not depend on the position in the sky. Nevertheless, this approximation is only in the likelihood, in pseudo-experiments, injection was done using the original KRAγ spectrum.

The other difference between Antares and IceCube likelihoods is that data are considered as a mixture of signal and background in IceCube, so

$$(1 - n_S) \cdot \mathcal{B}(\delta_i, E_i) = \mathcal{D}(\delta_i, E_i) - n_S \cdot \tilde{\mathcal{S}}(\delta_i, E_i), \tag{6.8}$$

where $\tilde{\mathcal{S}}$ and $\mathcal{D}$ are the distributions of signal and scrambled data respectively, in (δ_i, E_i). As explained above, in Antares we consider the signal in the blinded data negligible which can be expressed as $\mathcal{B} = \mathcal{D}$.

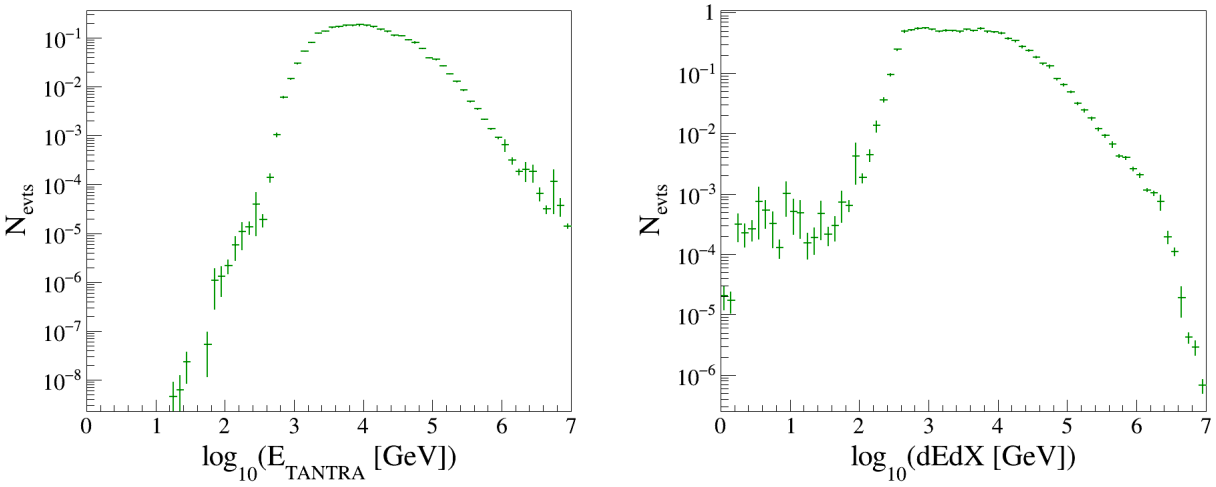

(a) Shower events.

(b) Track events.

Figure 6.6 – Signal distribution of the energy estimator integrated over the whole sky.

6.2 Inputs of the Likelihood

In this section the ingredients used to build the ANTARES likelihood function are described. Every quantity corresponds to reconstructed events.

Signal Angular Probability Density Function

$\mathcal{A}_S$ (figure 6.1) is the angular distribution of the reconstructed Monte Carlo signal events in equatorial coordinates.

Signal Energy Probability Density Function

$\mathcal{E}_S$ is the Monte Carlo distribution of logarithm of the energy estimator as a function of equatorial coordinates. The track and shower energy estimators are described in section 2.6.

To avoid a large statistical uncertainty from the use of a three dimensional histogram, we project it into two bi-dimensional histograms, marginalizing right ascension in one case (figures 6.3a and 6.3b) and declination in the other one (6.3c and 6.3d). Then we extract a slice in the angle of each histogram, this slice is renormalized to get the energy pdf at a certain right ascension on one side and at a certain declination on the other side. Then, the pdfs are combined by taking the square root of the product of these two energy pdfs to obtain $\mathcal{E}_S = \sqrt{\text{pdf}_\delta(E_i) \times \text{pdf}_\alpha(E_i)}$.

The distribution of the energy estimator integrated over right ascension and declination is represented in figure 6.6. One can see that the reconstructed energy is higher in average for showers than for tracks as can be seen in figure 7.4b.

Background Angular Probability Density Function

$\mathcal{A}_B$ is taken from the data distribution of the sine of the declination.

Systematic uncertainties on the acceptance of ANTARES optical modules [99] can affect this distribution. To account for them, $\mathcal{A}_B$ is a combination of two spline parametrizations of the (same) data distribution, $\mathcal{R}(\delta)$ and $\mathcal{B}(\delta)$ in red and blue respectively in figure 6.2.

The difference between both parametrizations is only the binning which is finer for $\mathcal{R}$.

The combination is done by

$$\mathcal{A}_B = \mathcal{R}(\delta) + r_\delta \cdot (\mathcal{B}(\delta) - \mathcal{R}(\delta)), \tag{6.9}$$

with r_δ a random number drawn from a Gaussian distribution with a mean of 1 and a standard deviation of 15 %. The standard deviation coming from the uncertainty on the effective area of the detector due to the uncertainty on the optical modules acceptance. If the value of r_δ gives $\mathcal{A}_B < 0.1 \cdot \mathcal{R}(\delta)$, we use $\mathcal{A}_B = \mathcal{R}(\delta)$.

Background Energy Probability Density Function

$\mathcal{E}_B$ depends on the zenith as the estimated energy also does as can be seen in figure 6.7. But the number of events in data is too small to avoid statistical uncertainties on a bi-dimensional distribution, so Monte Carlo simulations are used instead provided they show reasonable agreement. However, the high weight of the remaining Monte Carlo muon events (due to the large CPU time consumption of these events as explained in section 2.5.1) results in peaks in the distribution shown in figure 6.7. The muons represent around 35 % of the events in the shower Monte Carlo sample and around 10 % for tracks. To correct for this, the muon distribution is estimated by relaxing the quality cuts in order to extrapolate the obtained distributions. A marginalization is also used for showers as explained in the following.

Estimation of the muon distribution for tracks. The muon distribution in (E, θ) with a value of Λ_{Tr} relaxed to -5.5 can be seen in figure 6.8a. In figure 6.8b, it is smoothed and rescaled to the number of expected muons in the Monte Carlo track sample. This is added to the neutrino only distribution to obtain $\mathcal{E}_B^{\text{Tr}}$ that can be seen in figure 6.4b.

Estimation of the muon distribution for showers. For showers the idea is basically the same, the β_{Sh} and $\mathcal{L}_{\text{Dusj}}$ cuts are suppressed to obtain the distribution shown in figure 6.9. But the number of events is still too low, so this distribution is projected along the zenith on one side and along the energy estimator on the other side. The projections are smoothed. Then a bi-dimensional distribution where each bin contains the product of the two projections is produced. The projections and the final distribution can be seen in figure 6.10.

Then, this distribution is rescaled to the number of muons selected in the Monte Carlo shower sample and added to the neutrino-only distribution to obtain $\mathcal{E}_B^{\text{Tr}}$ that can be seen in figure 6.4a.

At this level, the test statistic $\mathcal{Q}$ gives an estimation of the signalness of the full data set. But without any point of comparison this value is hard to interpret quantitatively. Here come the pseudo-experiments.

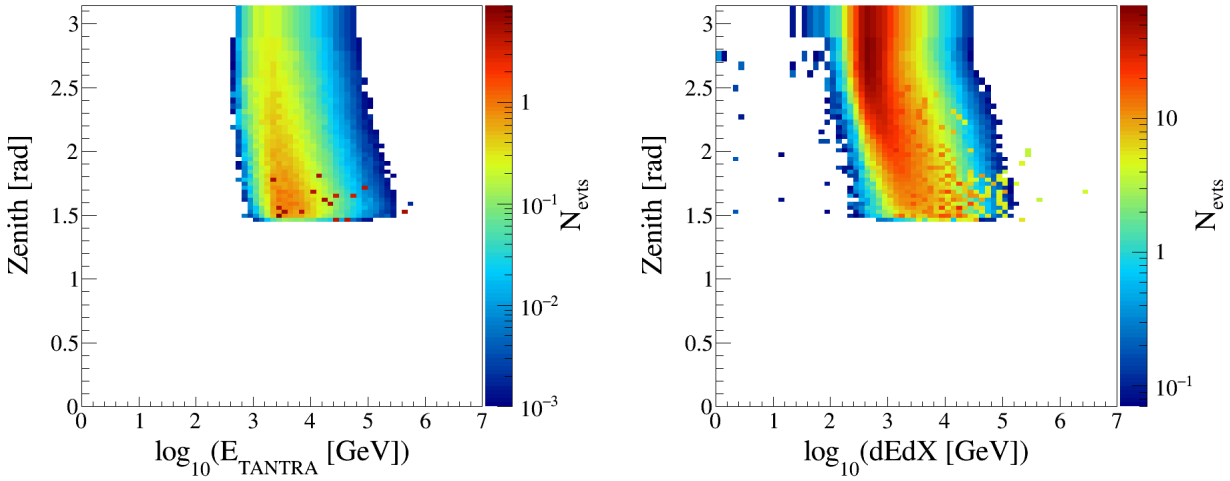

(a) Shower events.

(b) Track events.

Figure 6.7 – Background distributions of the energy estimator versus reconstructed zenith from Monte Carlo simulations. Peaks in these distributions are due to low statistics of the remaining atmospheric muon events that have a large weight compared to neutrinos. **(a)** Shower-like events, **(b)** Track-like events.

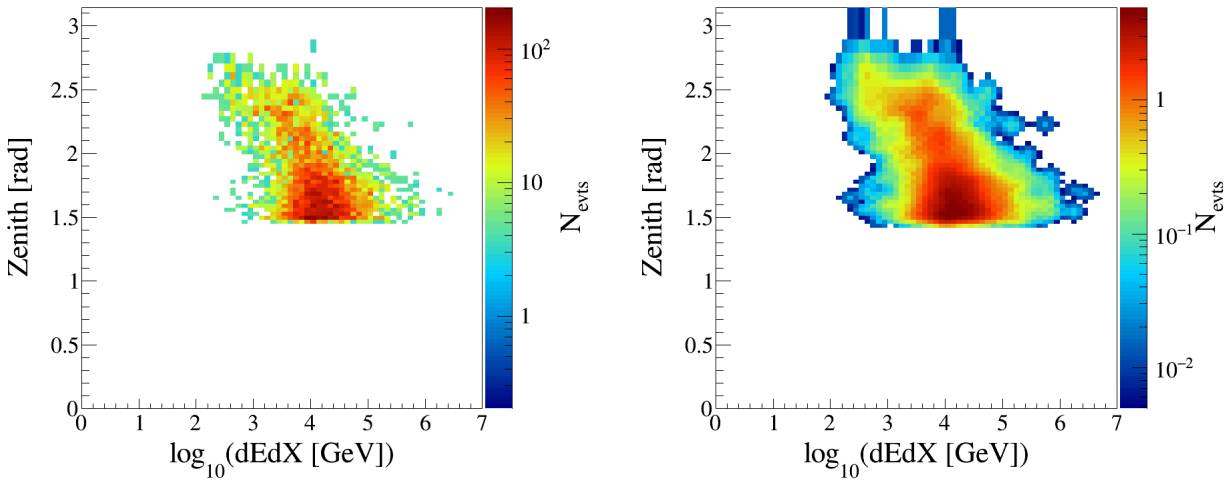

(a)

(b) After smoothing and rescaling

Figure 6.8 – Distribution of the number of atmospheric muon events selected as track-like events with smoother cuts as a function of the energy estimator and reconstructed zenith from Monte Carlo. **(b)** being smoothed and rescaled.

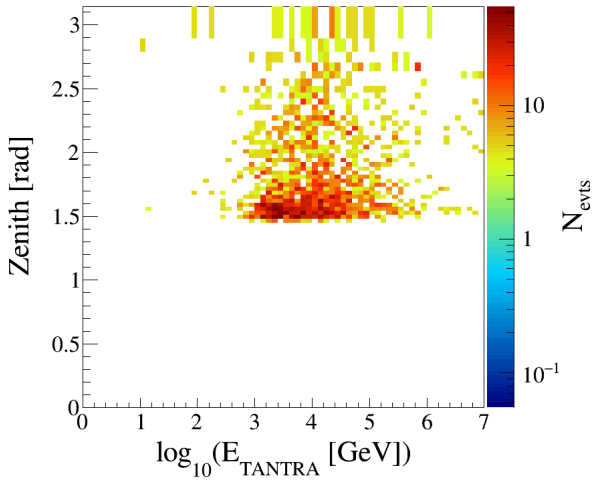

Figure 6.9 – Distribution of the number of atmospheric muons selected as showers with smoother cuts as a function of the energy estimator and the reconstructed zenith from Monte Carlo.

6.3 Pseudo-experiments

To evaluate the probability that our data contain or not some signal, a large quantity of independent replications of the same experiment is required. Therefore, pseudo-experiments are simulated by generating pseudo-data from the data and Monte Carlo distributions of the variables used in the analysis. For the ANTARES standalone analysis, 100 000 pseudo-experiments are produced in the background-only case, and 10 000 for numbers of signal events injected between 1 and 55. For the combined analysis, 10 000 pseudo-experiments are produced for 0 to 75 signal events injected. These quantities are chosen as a trade-off between CPU-time consumption and necessary statistics to put upper limits at a 3σ level or claim a discovery.

Signal Injection

Signal events are injected by drawing a value of the energy estimator from $\mathcal{E}_S$ (figure 6.3). The position is drawn from the same distribution as $\mathcal{A}_S$ (figure 6.1) with a binning twice finer in both axes as the signal injection is not as CPU-time consuming as the likelihood computation due to the low number of signal events injected. Then, it is converted into local coordinates by drawing a random time between 2007 and 2016 giving an upward-going event[3].

The ratio of showers over tracks injected is chosen by drawing a random number in [0, 1] for each signal event, if this number is larger than the fraction of showers in the Monte Carlo signal, this event is a track, else it is a shower. This method is equivalent to draw the number of tracks or showers from a Poisson distribution.

Background Injection

The number of background events is drawn from a Poissonian distribution with a mean value being the number of events in data. The energy estimator is drawn from $\mathcal{E}_B$ (figure 6.4). Zenith

[3]The analysis being integrated in time, it is not needed to account for annual variations of the acceptance of the detector.

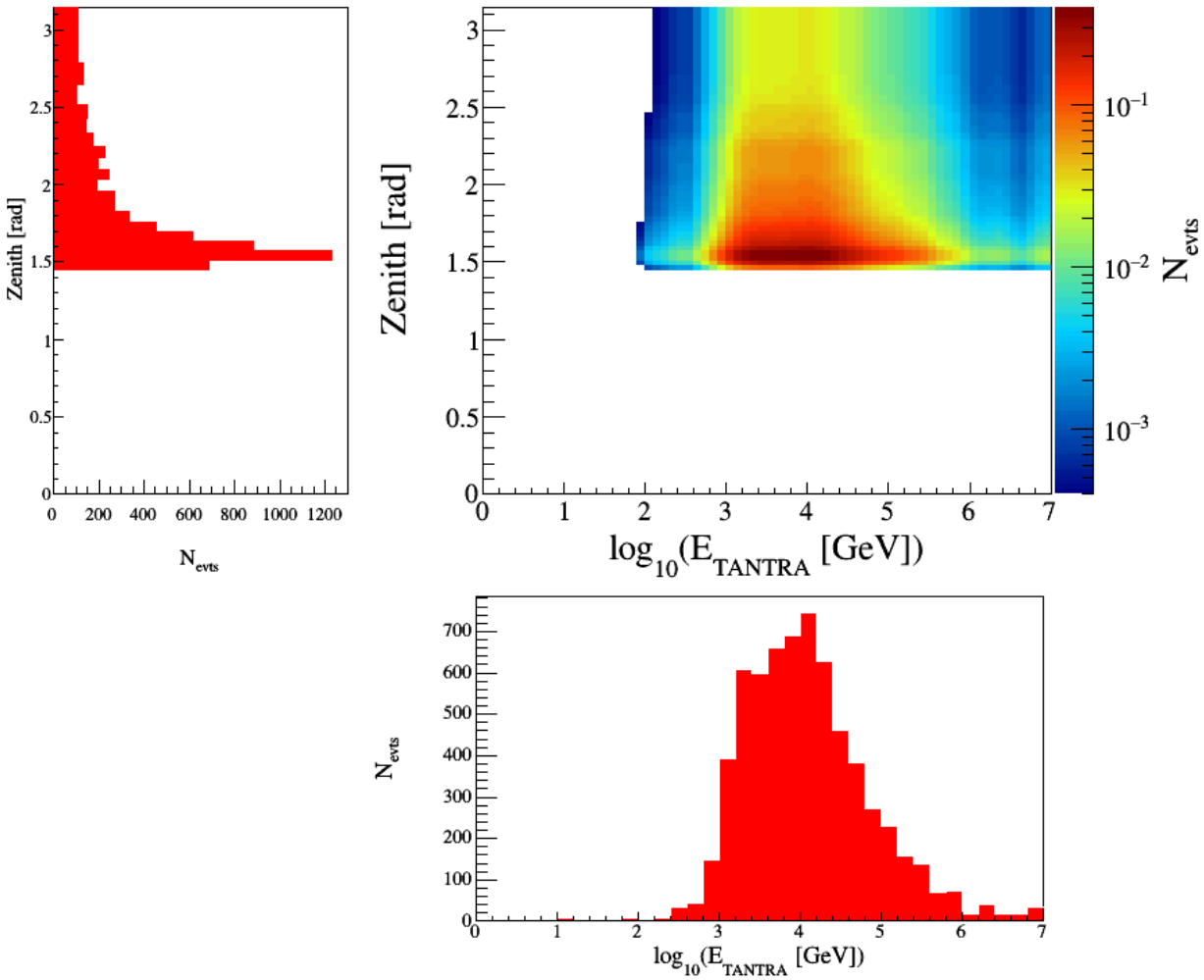

Figure 6.10 – Final distribution of the number of atmospheric muons selected as showers with smoother cuts. Plots in red are the smoothed x and y projections of figure 6.9. Each bin of the two dimension histogram corresponds to the product of the corresponding bins of the projections. This distribution is normalized to the number of atmospheric muon events selected as shower-like events in Monte Carlo. This histogram is used as the distribution of the atmospheric muons selected as shower-like events.

and azimuth angles are drawn accounting for systematics as described in 6.2 using the same value of r_δ. Data and Monte Carlo distributions with the splines are represented in figure 6.11.

6.4 Hypothesis Rejection

For each pseudo-experiment the test statistic $\mathcal{Q}$ is computed to obtain its distributions χ_Φ for each value of the injected signal flux, as represented in figure 6.12. The peak at $\mathcal{Q} = 0$ is due to pseudo-experiments with an under-fluctuation that fit 0 signal events which is the minimum value allowed by the fit.

The pseudo-experiments provide the *values* of the test statistic corresponding to a number of injected signal events $\mathcal{Q}_{n_{\text{inj}}}$. To get the *distribution* χ_Φ corresponding to an injected flux Φ, different methods are used in the two analyses.

In the combined analysis, χ_Φ is built by drawing $\mathcal{Q}_{n_{\text{inj}}}$ from a mixture of pseudo-experiments having n_{inj} injected signal events with $n_{\text{inj}} \in [0, 75]$. The proportion p of pseudo-experiments with n_{inj} injected events is

$$p(n_{\text{inj}}) = \sum_{n=0}^{N=75} \text{Gauss}(n; n_{\text{expect}}, \sigma_{15\,\%}) \times \text{Poiss}(n_{\text{inj}}; n). \tag{6.10}$$

The Gaussian accounts for the systematic uncertainty of 15 % on the effective area due to the uncertainty on the optical modules acceptance. The parameter n_{expect} is the mean number of signal events expected for a flux Φ. The Poissonian distribution accounts for statistical fluctuations.

In the ANTARES standalone analysis, the idea is the same except that the distributions $\chi_{n_{\text{inj}}}$ of $\mathcal{Q}_{n_{\text{inj}}}$ with n_{inj} in [1, 55] are first computed. Then χ_Φ results of weighted sums of $\chi_{n_{\text{inj}}}$ with weights $p(n_{\text{inj}})$.

The sensitivity can be computed from the χ_Φ distributions and comparing the value of the test statistic of the data $\mathcal{Q}_{\text{data}}$ to χ_Φ allows to compute the p-value and the upper limit at 90 % confidence level.

The p-value is defined as the probability to have a value of $\mathcal{Q}$ higher than $\mathcal{Q}_{\text{data}}$ in the background-only hypothesis. It is the blue area in figure 6.13, which is a zoom of figure 6.12. To simplify, one could say that the p-value is the *backgroundness* of the data. A low p-value means a low probability that the data set contains only background as a consequence it implies a high significance of signal, it is used to claim a discovery.

The upper limit is defined as the smallest flux having a probability smaller than 10 % to yield to a test statistic value lower than $\mathcal{Q}_{\text{data}}$ as represented in green (resp. red) in figure 6.13 for $\Phi_{\text{KRA}\gamma^5}$ (resp. $2 \times \Phi_{\text{KRA}\gamma^5}$). In other words, it is the smallest flux that can be excluded with a 90 % confidence level.

In the ANTARES standalone analysis (resp. combined analysis) the sensitivity is defined as the average (resp. median) upper limit obtained in the background-only case, i.e. obtained from the values of $\chi_{\Phi=0}$. Average and median upper limits are different as the test statistic is required

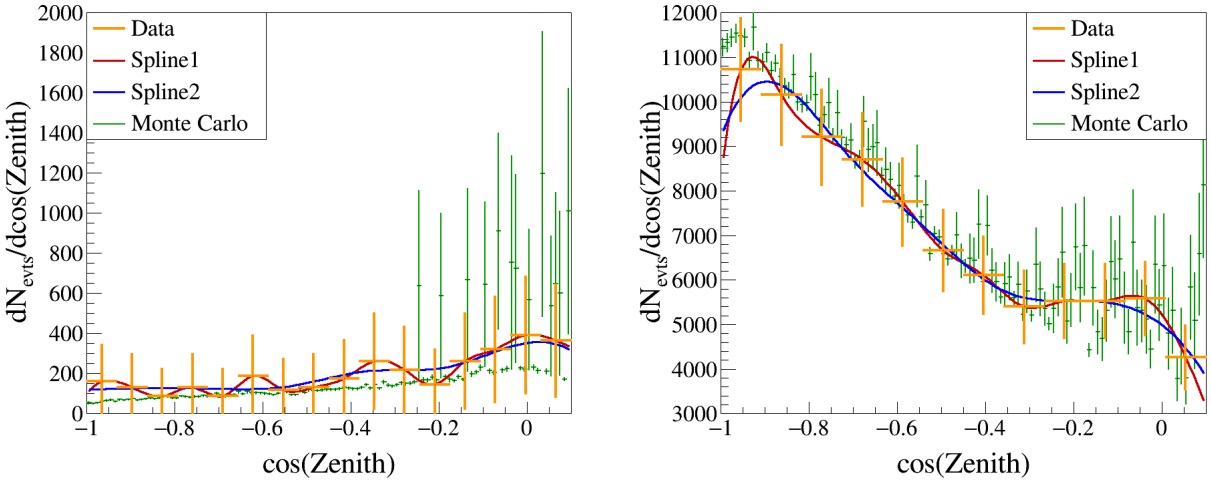

(a) Showers, cosine of zenith.

(b) Tracks, cosine of zenith.

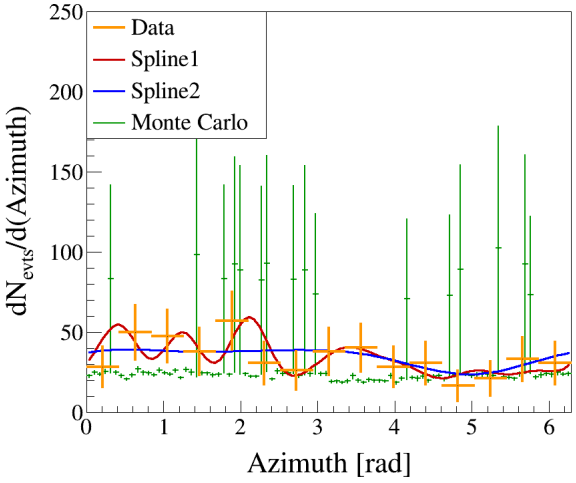

(c) Showers, azimuth.

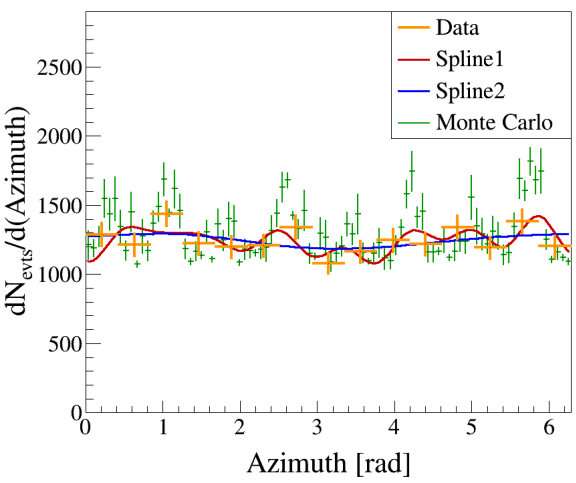

(d) Tracks, azimuth.

Figure 6.11 – Background distribution of the cosine of the reconstructed zenith (top) and reconstructed azimuth (bottom) from data and Monte Carlo. Red and blue curves are two different spline parametrizations of the data, a combination of both is used to get the coordinates of injected background events. **Left**: Shower-like events, peaks in the Monte Carlo are due to atmospheric muons which have a large weight compared to neutrinos, **right**: Track-like events.

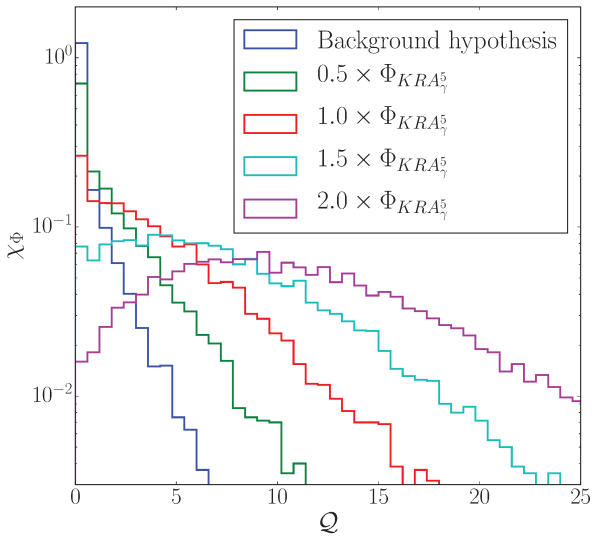

Figure 6.12 – Probability density functions of the test statistic obtained from pseudo-experiments for different amounts of signal injected.

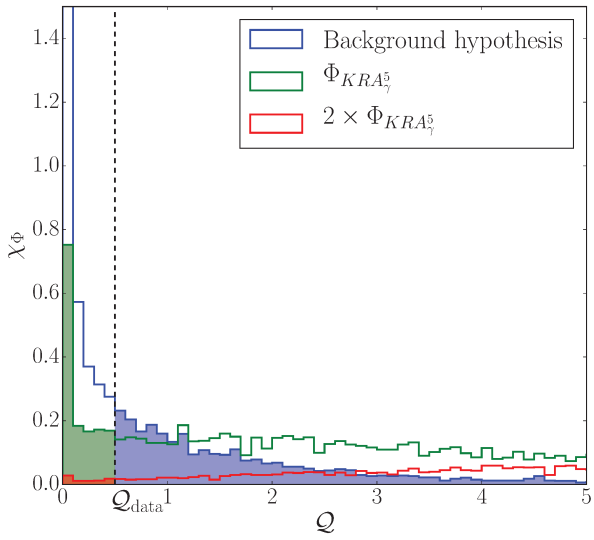

Figure 6.13 – Illustration of hypothesis testing with a zoom on the probability density functions of the test statistic for different signal and background only hypotheses. The blue area represents the p-value, the green and red areas represent the proportion of pseudo-experiments that have a value of the test statistic smaller than the one of data for fluxes $\neq 0$. Note that a bin can have a value higher than one if its width is small enough.

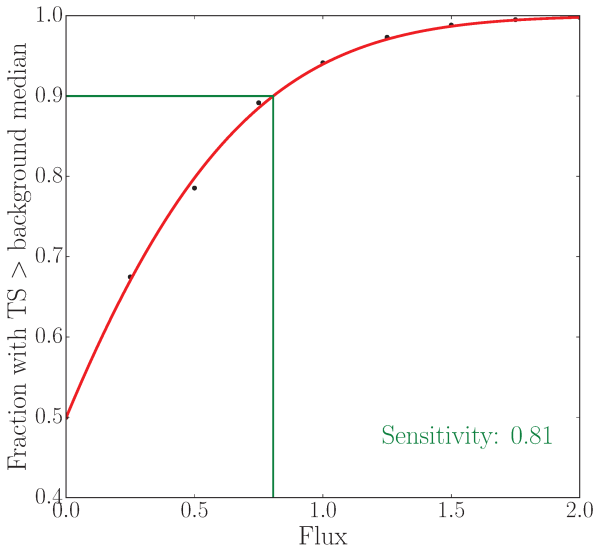

Figure 6.14 – Fit of the sensitivity from the fraction of pseudo-experiments with a test statistic greater than the median test statistic of background as a function of the injected flux.

to have a positive value. The average upper limit is more conservative, it was the choice of ANTARES but ICECUBE team preferred to use a median upper limit. Figure 6.14 represents the fraction of the pseudo-experiments with a test statistic $\mathcal{Q}$ higher than the median test statistic of background $(\mathcal{Q}_{\Phi=0})_{1/2}$. In other words it is the integral of χ_Φ above $(\mathcal{Q}_{\Phi=0})_{1/2}$ as a function of the flux, therefore it is fitted by a Gauss error function. Then, the sensitivity is the flux for which 90 % of the $\mathcal{Q}$ are above $(\mathcal{Q}_{\Phi=0})_{1/2}$.

6.5 Bias Correction

For each sample of the combined analysis, the plot of the flux injected in the pseudo-experiments versus the flux fitted is shown in figure 6.15. An unbiased sample should have medians along the dashed line, corresponding to a fitted flux equals to the true flux. It is not the case here, small biases are present. Nevertheless, the analyses take into account these biases as they are present in pseudo-experiments just like in data, they don't impact the results.

Biases have an impact on the fitted flux, by definition, but it can also affect the sensitivity in the combined analysis if two sets of pseudo-experiments have different biases. In particular, opposite biases in two samples would move away the maximum of the log-likelihood ratio of the two samples, this would lead to a smaller value of the test statistic, closer to the background case.

To minimize this effect the biases are fitted and corrected in the combined analysis. For each sample the bias is fitted by a linear function, using the median fitted fluxes as shown in figure 6.15. ANTARES showers have a bias of $\Phi_{\text{reco}} = 1.11 \times \Phi_{\text{inj}}$, it is $0.78 \times \Phi_{\text{inj}}$ for the tracks and $1.09 \times \Phi_{\text{inj}}$ for ICECUBE. Then the bias is corrected by scaling the flux (the abscissa) in the log-likelihood ratio curve as illustrated in figure 6.16. The use of a linear function passing by

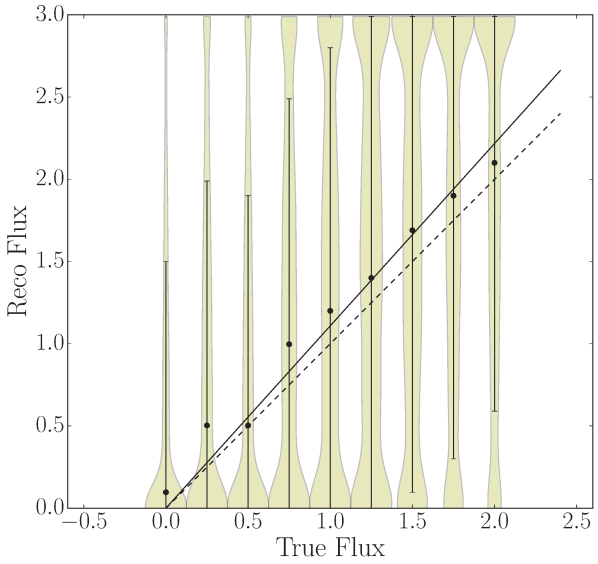

(a) ANTARES showers.

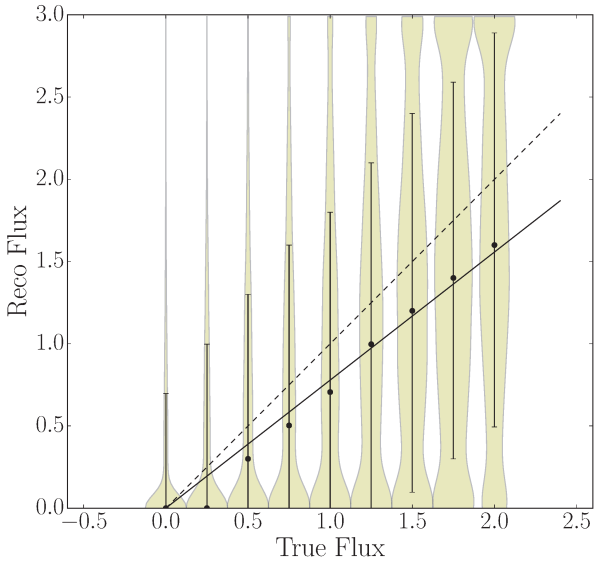

(b) ANTARES tracks.

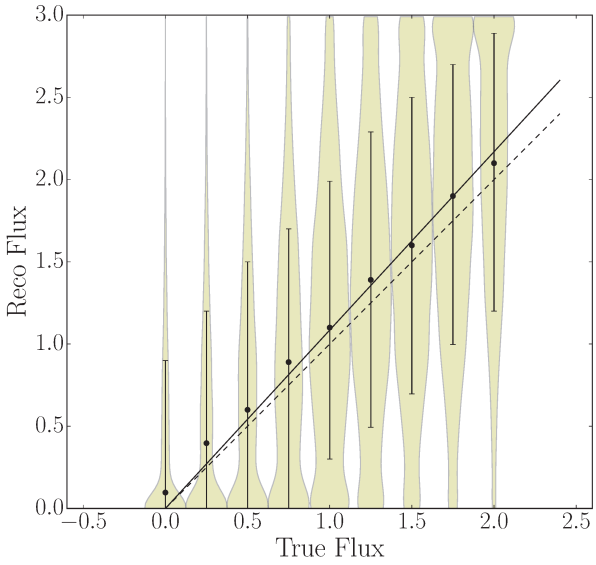

(c) IceCube tracks.

Figure 6.15 – Sample biases. Distributions of the fitted flux for different injected fluxes (brown areas). The dashed line corresponds to a fitted flux equals to the injected one and the solid line is the fit of the bias. The black dots correspond to the medians.

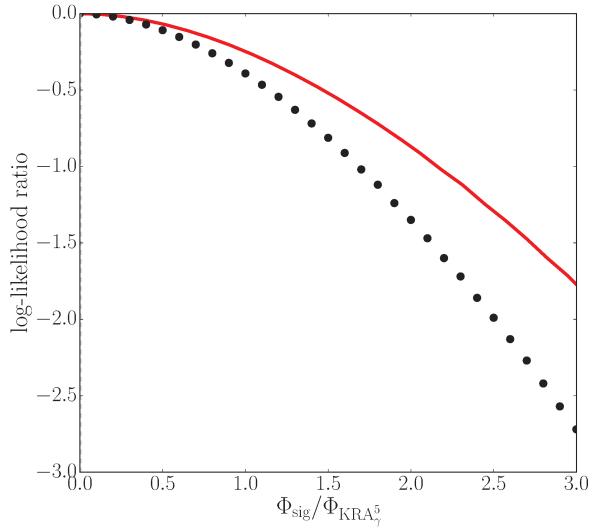

Figure 6.16 – Illustration of the bias correction for a pseudo-experiment of the ANTARES track sample. The points correspond to the the initial log-likelihood ratio values and the red line to the corrected ones.

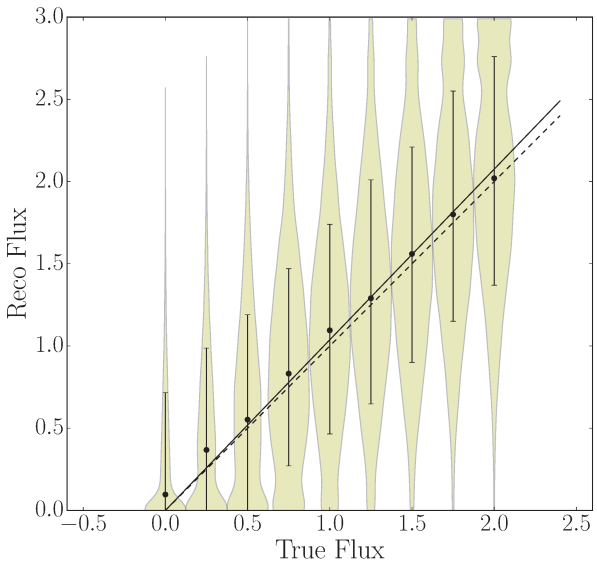

Figure 6.17 – Combined sample bias. Distributions of the fitted flux for different injected fluxes for the combined sample after correction. The dashed line corresponds to a fitted flux equals to the injected one and the solid line is the fit of the bias remaining after correction. The black dots correspond to the medians.

zero for the fit of the bias permits to keep a log-likelihood ratio of 0 when a null flux is fitted. However, it neglects the biases present at low values of the injected flux.

After correction, the combined sample has a negligible bias of $\Phi_{reco} = 1.04 \times \Phi_{inj}$ as can be seen in figure 6.17.

Chapter 7

Results

This chapter presents the unblinding process as well as the sensitivity and results of the two analyses. The physical implications are also detailed.

7.1 Unblinding

During the conception of the analysis, data are blinded by randomizing azimuth in order to hide a potential signal as explained in section 6.1. The purpose of the blinding is to avoid any influence of the data set on the choice of the event selection or the way the analysis is done. If any modification is done after the unblinding because of the results obtained, it biases the p-value.

Once the analysis method and the values of the quality cuts are defined and have been approved by the collaboration, it is time to unblind data to get the results. These results are produced for 5 000 different parametrizations of the spatial background distribution used in the likelihood. Indeed, as the spatial distribution of background is fluctuated in pseudo-experiments as explained in section 6.2 to account for the systematic uncertainty, the same should be done for the unblinded data. However, in the pseudo-experiments, the systematic effects injected are known which is not the case here. The two analyses solve this problem in different ways, the ANTARES standalone analysis uses an average value when in the Combined analysis the systematic effects are fitted. It is developed in the following paragraphs.

7.1.1 ANTARES Standalone Analysis

In the ANTARES standalone analysis, the test statistic is fitted for each parametrization of the background of the unblinded data, the distribution is shown in figure 7.1. Then, the average of these test statistics is used as the unblinded test statistic, $\langle Q^{\text{ANT}}_{\text{data}} \rangle = 0.65$. The number of fitted tracks and showers are obtained in the same way, $\langle n_{\text{Tr}} \rangle = 2 \cdot 10^{-3} \approx 0$ and $\langle n_{\text{Sh}} \rangle = 1.9$.

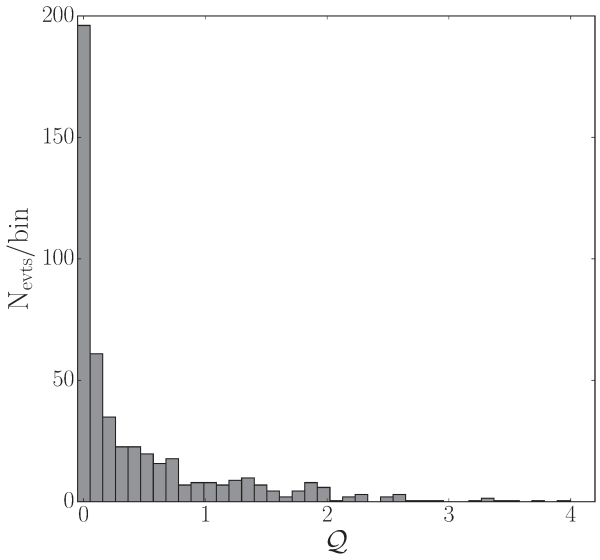

Figure 7.1 – Distribution of the test statistic for the different background parametrizations.

7.1.2 Combined Analysis

In the combined analysis, the method of the profile likelihood is used. It consists on fitting the parameters corresponding to the systematic effects. To do so, the flux is fitted by maximizing $\mathcal{L}_{S+B}$ for each background parametrizations and the one that maximizes $\mathcal{L}_{S+B}(\Phi_{\text{fitted}})$ is used.

N.B. It is not the likelihood ratio which is used, as

$$\frac{\mathcal{L}_{S+B}}{\mathcal{L}_{B}} = \prod_{i=1}^{N} \frac{n_S \cdot \mathcal{S} + n_B \cdot \mathcal{B}}{N \cdot \mathcal{B}} = \prod_{i=1}^{N} \frac{n_S \cdot \mathcal{S}}{N \cdot \mathcal{B}} + \frac{n_B}{N} \tag{7.1}$$

which would lead to favor the extreme value of the nuisance parameter minimizing the background $\mathcal{B}$.

The resulting curve is shown in figure 7.2 on top of 50 curves from different background parametrizations.

7.2 Sensitivities and Complementarity

For the Antares standalone analysis with nine years of data, the sensitivity is at 140 % of the flux normalization of the KRAγ[5] model. We remind that the sensitivity is defined as the average upper limit at 90 % confidence level. As expected, the sensitivity for KRAγ[50] is better since the flux normalization is larger, especially for highest energy events. It is at 105 % of $\Phi_{\text{KRA}\gamma^{50}}$.

The sensitivity improves down to 81 % of $\Phi_{\text{KRA}\gamma^{5}}$ with the combination. The sensitivities of each sample are shown in figure 7.3. The relative contribution of each event sample is defined as the improvement it brings to the sensitivity dividing this by the sum of all contributions. This way Antares tracks and showers contribute to 25 % and 14 % of the sensitivity, respectively and IceCube for 61 %.

The combination is an opportunity to benefit from the complementarity of the two detectors, as is illustrated by figure 7.4. While IceCube has much higher statistics than Antares,

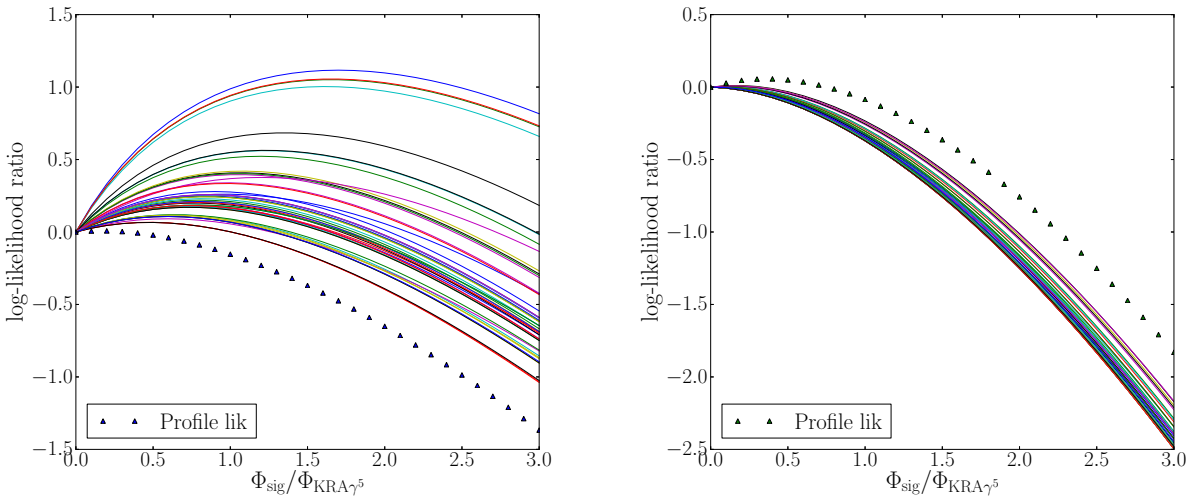

(a) ANTARES showers. **(b)** ANTARES tracks.

Figure 7.2 – Log-likelihood ratio curves as a function of the normalization of the flux for different background parametrizations. The curve corresponding to the fitted systematic effects is represented by triangles.

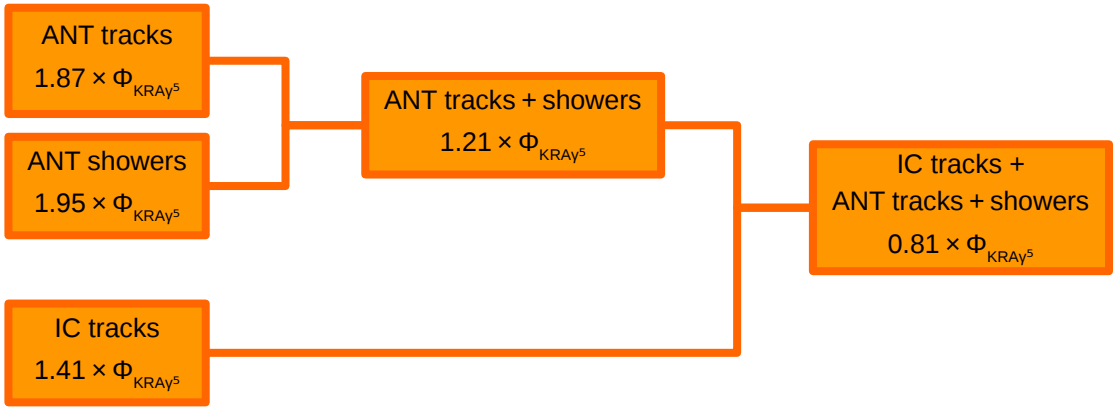

Figure 7.3 – Sensitivities of the combined analysis for each sample, each experiment, and the total.

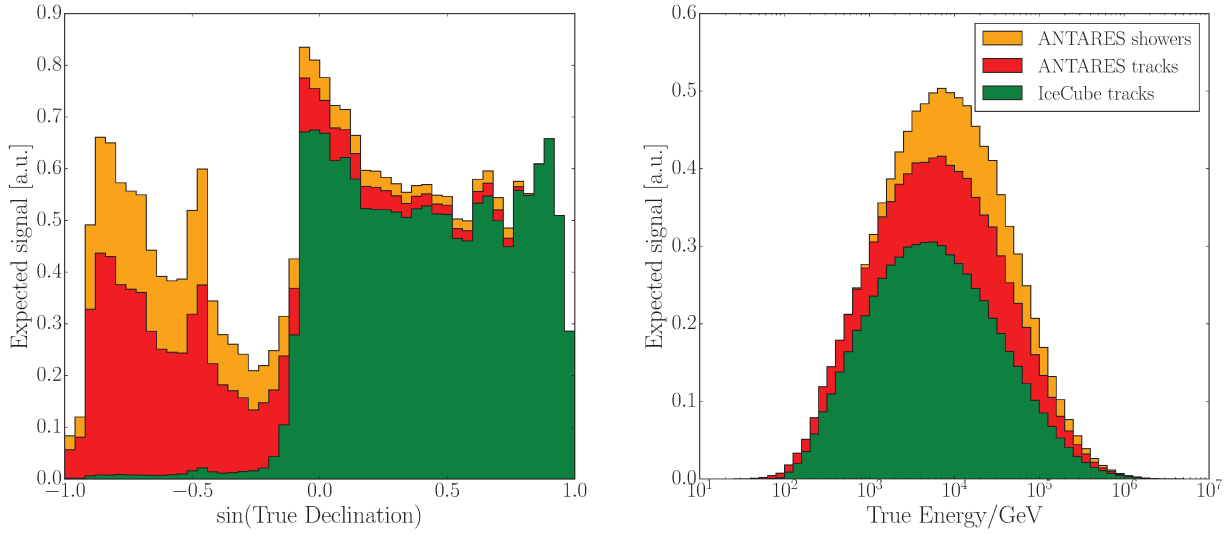

(a) (b)

Figure 7.4 – Stacked histograms (i.e. every bin shows the fractional contribution of every sample summed on top of each other) of the signal expected from the model with 5 PeV cutoff as function of the declination **(a)** and energy **(b)**. The colored area of each histogram represents the relative contribution to the sensitivity of the corresponding event sample. The relative contribution to the sensitivity is defined as the difference in the sensitivity flux resulting from the addition of a certain event sample divided by the combined sensitivity flux.

figure 7.4a shows that ANTARES offers enhanced sensitivity in the Southern sky where a larger flux is expected especially around the Galactic centre ($\sin(\delta) \approx -0.5$). This favourable view is coupled with a relatively better angular resolutions of the ANTARES tracks. Despite ICECUBE has a better sensitivity for higher energy events, figure 7.4b shows that both experiments test a similar energy range. This is due to the fact that the model yields to lower energy events in the Northern sky.

One can see that applying the same implementation of the analysis as in the combination to ANTARES data only, leads to better results than the ANTARES standalone analysis, this comes from two main reasons. An obvious reason is that one year of ANTARES data has been added to the combined analysis, but the definition of the sensitivity is also different as it is defined as the median upper limit in the combined analysis.

Remark on the Signal Hypothesis Considered: We would like to stress that the signal hypothesis tested here, the KRAγ model, does not account for potential extragalactic or point source components. Indeed, an isotropic extragalactic neutrino flux as well as numerous unresolved point sources could contaminate the searched signal. This is not problematic in the case of upper limits but would be problematic to claim a discovery. However, this analysis reduces the influence of an isotropic flux by accounting for the particular morphology of this model, peaked in the Galactic center. For what concerns the point source component, no Galactic point sources have been detected until now and a combined limit has been put on the expected point source

Table 7.1 – Sensitivity, expected flux and results of the combined, ANTARES alone [102] and ICECUBE alone [97] analyses on the KRAγ model with the 5 and 50 PeV cutoffs. The ANTARES alone sensitivity is defined as the average upper limit, the ICECUBE and combined ones are defined as the median upper limit. For the ANTARES standalone analysis the expected fluxes are given in a number of tracks (Tr) and showers (Sh).

Energy cutoff	Analysis	Sensitivity $[\Phi_{\mathrm{KRA}\gamma}]$	Expected flux	Fitted flux	p-value	Upper limit $[\Phi_{\mathrm{KRA}\gamma}]$
5 PeV	ANTARES	140 %	9.3 Tr, 2.3 Sh	0 % Tr, 83 % Sh	67 %	110 %
	Combined	81 %	$\Phi_{\mathrm{KRA}\gamma^5}$	47 %	29 %	119 %
50 PeV	ANTARES	105 %	11 Tr, 2.8 Sh	0 % Tr, 93 % Sh	54 %	120 %
	ICECUBE	79 %	213 Tracks	46 %	29 %	120 %
	Combined	57 %	$\Phi_{\mathrm{KRA}\gamma^{50}}$	37 %	26 %	90 %

flux [100]. In any case, as shown in the following section, only upper limits are put here so this is not an issue.

7.3 Results

The sensitivities and results obtained for both analyses as well as the ICECUBE standalone analysis [97] are summarized in Table 7.1. Systematic uncertainties on the acceptance of the ANTARES optical modules are included in the analysis as explained in section 6.2. For what concerns ICECUBE, systematic effects lead to an uncertainty on the fluxes of 11 % as described in [101], it is not included here.

Some signal is fitted in the shower channel of the ANTARES standalone analysis but not in the track channel. This could be an under-fluctuation in the track channel coupled to the bias that you can see in figure 6.15b when the signal is weak ($0.25 \times \Phi_{\mathrm{KRA}\gamma^5}$). As said earlier, this bias being present in the pseudo-experiments, it is taken into account in the upper limit.

Although the fitted number of shower is close to the expected flux, the p-value is still very background-like as most of the sensitivity comes from tracks. Nevertheless, the lower proportion of showers fitted for the KRAγ^5 model improves the upper limit in comparison with the KRAγ^{50} model, leading to $1.1 \times \Phi_{\mathrm{KRA}\gamma^5}$.

The ICECUBE standalone analysis did not test the KRAγ^5 model. Their sensitivity on the other model, KRAγ^{50}, is better than the ANTARES one but the limit is the same. This can be explained by the high number of events they fitted. Indeed, Table 7.1 shows that ICECUBE analysis has a p-value nearly twice lower than ANTARES.

The combination leads to much better sensitivities. The upper limit is under the flux normalization for the KRAγ^{50} model which is rejected with a 92 % confidence level. As explained in chapter 4, the 50 PeV cutoff represents an extreme tuning of the acceleration parameters for the Galactic cosmic rays, so the rejection of this version of the model might not be surprising.

On the other hand, the KRAγ^5 model is not rejected and the combined upper limit obtained is

actually worse than the ANTARES alone upper limit. This is partly due to the over-fluctuation in ICECUBE data, but also because of the difference in the definition of the test statistic explained in section 6.1.2. Indeed, the upper limit worsens[1] when changing only the combined test statistic $\mathcal{Q}_{\text{Comb}}$ to $\mathcal{Q}_{\text{ANT}}$ in the implementation of the analysis for the ANTARES samples. This is because $\mathcal{Q}_{\text{Comb}}$ uses the information of the shape of each curve and not only the maximum as does $\mathcal{Q}_{\text{ANT}}$. In the specific case of a null flux fitted in one of the two samples (tracks here), it can give distinct results depending on the slope of the curve of the null-flux sample. If the ANTARES tracks curve of the figure 6.5 was decreasing faster, $\mathcal{Q}_{\text{Comb}}$ would be lower while it would not influence $\mathcal{Q}_{\text{ANT}}$ if the maximum of the ANTARES track sample was zero (which is the case for the nine years sample [102]).

The upper limits are presented in figure 11.2 in comparison with the model predictions. The previous ANTARES upper limit on the KRAγ^5 model is also shown as well as the ICECUBE upper limit on KRAγ^{50}. The boxes represent the isotropic diffuse astrophysical neutrino fluxes measured by ICECUBE with starting events [35] and upward-going tracks [32]. The ICECUBE data combining different samples from the whole sky are shown simultaneously with the corresponding fit and the fit of the eight year muon sample from the Northern sky.

Considering that KRAγ^{50} is excluded, the KRAγ^5 model gives a more intense diffuse Galactic neutrino flux than all other available models. In particular, the flux in the central ridge where a hardening of the cosmic rays is reproduced is the most intense. As a consequence, the limits presented here further constrain the possible contribution of the Galactic diffuse emission to the ICECUBE spectral anomaly [32] (see section 1.6). In the six-year HESE sample[2], 47.0 events are expected to be of cosmic origin above 60 TeV [103]. The combined analysis implies that a maximum of 4.5 events originate from diffuse Galactic cosmic ray interactions. It corresponds to 9.6 % of the total HESE flux. This limit is more restrictive than the one previously derived by [27, 91].

With the rejection of the KRAγ^{50} version of the model, its constraints are extended in an energy range from tens of GeV with the *Fermi*-LAT data up to hundreds of TeV. This is the first combined constraint on diffuse Galactic neutrino emission by ICECUBE and ANTARES. While it is challenging to infer the energy break between Galactic and Extragalactic cosmic ray spectra with the gamma-ray observations, crucial informations can be expected with the incoming neutrino analyses including the ICECUBE shower events or, on a longer time-scale, with KM3NeT.

[1] But the sensitivity does not change significantly.

[2] HESE stands for High-Energy Starting Events, this sample corresponds to high-energy events whose interaction vertex is contained inside of the detector in order to reject at most the background. This sample is sensitive to the whole sky.

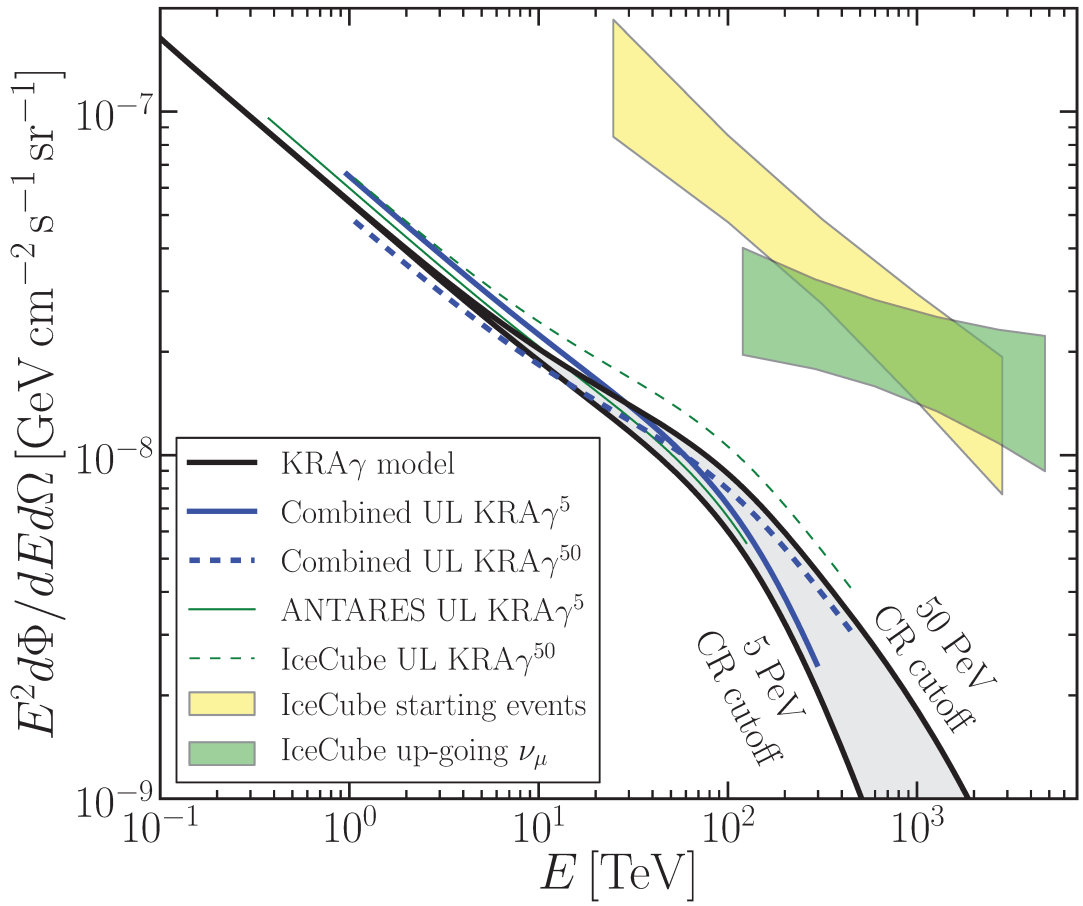

Figure 7.5 – Combined upper limits at 90 % confidence level (blue lines) on the three-flavor neutrino flux of the KRAγ model with the 5 and 50 PeV cutoffs (black lines). The green lines show previous upper limits by IceCube and Antares. The boxes represent the isotropic astrophysical neutrino fluxes measured by IceCube using starting events (yellow) and upward-going tracks (green).

Part III:

Gravitational Wave Follow-up

Chapter 8

Gravitational Waves and Binary Neutron Stars

This chapter gives the necessary background needed for the understanding of the neutrino follow-up analysis of the binary neutron star merger GW170817, its goal and its impact. It describes what is a binary neutron star, the potential high-energy neutrino emission expected from a binary neutron star coalescence and introduces gravitational waves and gravitational wave detectors.

8.1 Binary Neutron Stars

It is in 1934, only two years after the discovery of the neutron by James Chadwick [104] that Walter Baade and Fritz Zwicky [105] proposed the existence of the neutron stars resulting from a supernova. It is Jocelyn Bell and Antony Hewish [106] who observed for the first time a neutron star in the form of a pulsar in 1967.

A neutron star results from the evolution of a heavy star. As illustrated in figure 8.1, a star heavier than $10\,M_{\text{Sun}}$ becomes a red supergiant when nuclear fusion occurring in its core produces heavier elements up to iron and nickel. When the iron core reaches the Chandrasekhar mass, it starts collapsing. This step marks the beginning of a so-called *core-collapse supernova* which results in a neutron star if the degeneracy pressure of the neutrons balances the gravitational forces depending on the mass and the equation of state. If the mass is too high and consequently the gravitational force too strong, it results in a black hole. A complete review on core-collapse supernova can be found in [107].

Neutron stars are the smallest and densest known stars, a teaspoon of its material would contain 900 times the mass of the Great Pyramid of Giza which is of about six million tons.

Their core is composed of neutrons and protons and potentially an inner core of a quark gluon plasma as shown in figure 8.2. The core is covered by a solid crust above which exist both an ocean and atmosphere of much less dense material [108].

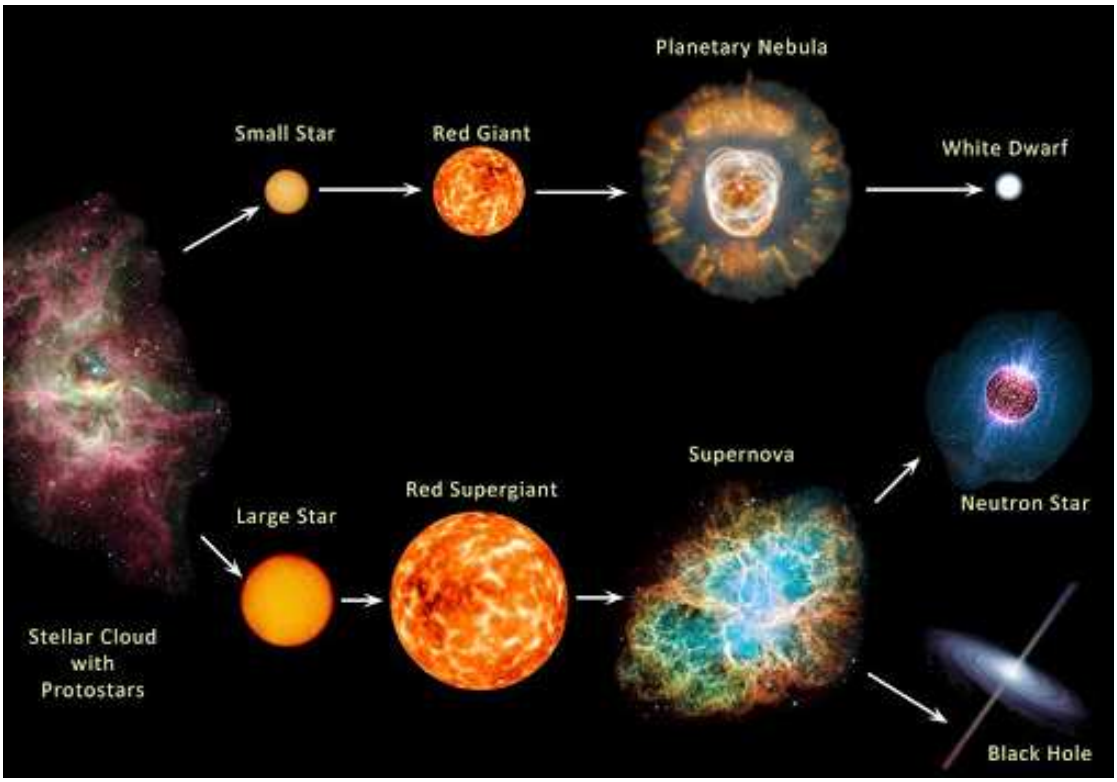

Figure 8.1 – Stellar evolution depending on the star mass.

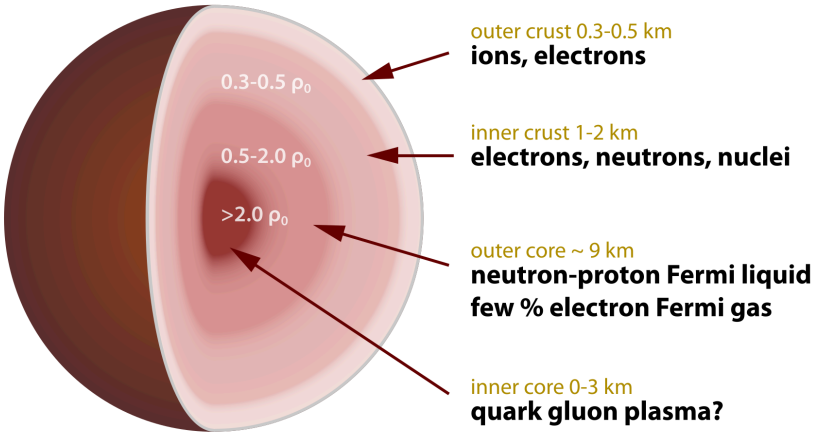

Figure 8.2 – Cross section of a neutron star. The parameter ρ_0 represents the saturation density of nuclear matter. Schematic by Robert Schulze, distributed under a a CC-BY 3.0 license.

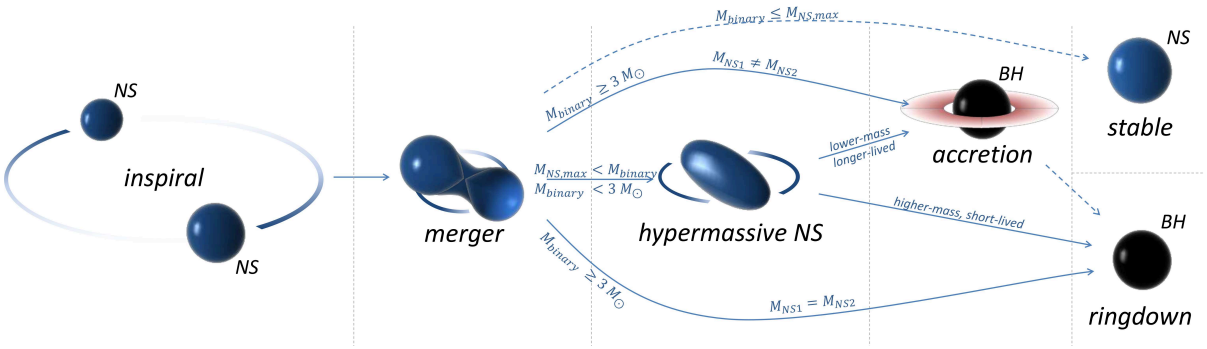

Figure 8.3 – Evolution of a binary neutron star coalescence. The total mass of the binary (M_{binary}) and the difference between the two masses (M_{NS1} and M_{NS2}) determine the evolution of the system. $M_{\text{NS, max}}$ is the Tolman–Oppenheimer–Volkoff limit on the mass above which a cold, non-rotating neutron star collapses into a black hole. Adapted from [113].

Neutron stars can sometimes be coupled to form a binary system. The formation of these systems is still under study but it could result from the evolution of a pair of massive stars [109]. We are interested in the coalescence of these binary systems, here.

The evolution of a binary neutron star coalescence is illustrated in figure 8.3. Depending on the total mass of the binary system and the equation of state of ultradense matter, it can collapse into a black hole. If both neutron stars have different masses the black hole is surrounded by an accretion disk. If the total mass is lower than or close to a characteristic mass, it can remain an indefinitely stable or long-lived neutron star. This mass is called the *Tolman-Oppenheimer-Volkoff limit* [110, 111] and it corresponds to 1.5–3.0 M_{Sun} with M_{Sun} the mass of the sun.

Such neutron star rotates very fast with an extremely powerful magnetic field that can be due to a magnetohydrodynamic dynamo process or other processes [112]. It is called a magnetar.

High-energy neutrino emissions can result from this coalescence as developed in the following sections.

8.2 Neutrino Emission from Binary Neutron Star Mergers

8.2.1 Prompt and Extended Emissions: Within Hundreds of Seconds

During the coalescence of two neutron stars or a black hole and a neutron star, part of the matter composing the neutron stars is ejected. Neutrino emissions can be expected from this mechanism as explained in the following, it will be qualified as *prompt emission*. The neutrino emission can even occur from the inside of the object before any electromagnetic emission. In contrast, we will call *extended emission* an emission on a longer time-scale of few hundreds of seconds. This extended emission is supposedly due to the fluctuations of the outflow caused by the fall-back of the ejecta on the central engine, this results in a lower Lorentz factor [114].

In more details, the high spin of the central engine induces very strong electromagnetic fields that collimate the ejected matter into a bipolar relativistic jet as can be seen in figure 8.4 [115].

This outflow of matter and energy is unsteady and causes internal shocks in the jet. Indeed, the matter ejected with a high Lorentz factor encounters layers of matter ejected earlier with a lower Lorentz factor, the relative motion of these two layers leads to a relativistic shock front.

As a consequence, [114] propose that electrons and protons of the jet experience Fermi acceleration and that γ-rays are emitted through synchrotron or inverse-Compton radiations generating a γ-ray burst. In the mean time, accelerated protons interact with photons or non-relativistic protons to produce charged pions and kaons which decay into muons and neutrinos. The resulting muons decay also, into neutrinos and electrons:

$$\begin{array}{lcccccc} p + p/\gamma & \rightarrow & \pi^0 & + & \pi^+ & + & \pi^- & + & \ldots \\ & & \downarrow & & \downarrow & & \downarrow & & \\ & & \gamma + \gamma & & \mu^+ + \nu_\mu & & \mu^- + \bar{\nu}_\mu & & \\ & & & & \downarrow & & \downarrow & & \\ & & & & e^+ + \nu_e + \bar{\nu}_\mu & & e^- + \bar{\nu}_e + \nu_\mu & & \end{array}$$

More details are given in section 1.4. As a consequence, two muon neutrinos are produced for one electron neutrino. However, we can assume equal fluence at Earth in all flavour because of neutrino flavour oscillation as explained in section 4.3.2.

The high-energy neutrino flux resulting from these processes has been computed in [114]. They described the photon density in the jet by a broken power-law function. For cosmic rays, the canonical E^{-2} power-law spectrum has been used. Then, the spectrum of neutrinos produced through the proton-proton or proton-gamma interactions described above is computed. Previous short γ-ray bursts observations are used to estimate typical values of the physical quantities like the magnetic field or the isotropic equivalent luminosity for each emission process. Figure 8.5 represents the resulting prompt and extended neutrino emission expected. The extended emission is the largest because its lower Lorentz factor results in interactions closer to the central engine where the photon density is larger, therefore the meson production efficiency is higher [116]. Two versions of the extended emissions are modelled with different assumptions on the parameter values, an optimistic and a moderate version.

A conservative time window in which the prompt neutrino emission from a typical γ-ray burst is expected has been estimated in [117]. This time window is of [- 350 s, + 150 s] around the burst, considering possible a prompt emission since the central engine is active until the end of the γ-ray burst. This window has been extended to ± 500 s in order to account for the extended emission and to be more conservative. It has been used in most of the previous searches for neutrino counterparts from gravitational wave events. A time window of ± 1 h looking for even more extended emissions has been used as well.

8.2.2 Late Emission: After Days

It has been predicted in [112] that a high-energy neutrino emission, peaking days after the merger can be expected if a long-lived millisecond magnetar results from the merger.

Depending on the signal to noise ratio, gravitational wave informations could probe the presence of such a magnetar for tenths of seconds following the merger. However gravitational wave data would not inform us on a potential collapse of the remnant into a black hole while

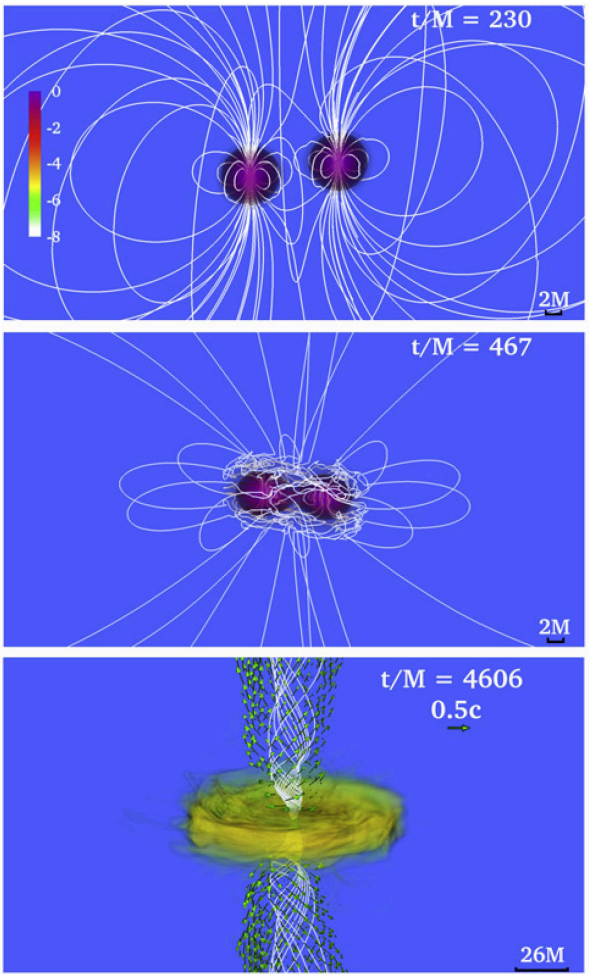

Figure 8.4 – Snapshots of the rest-mass density at selected times of a binary neutron star merger. The green arrows in the bottom panel indicate plasma velocity and the white lines show the B-field structure. The colorscale represents the density (in log scale) normalized to its initial maximum value of $5.9 \cdot 10^{14} \times (1.625 M_{\rm Sun}/M_{\rm NS})^2\,{\rm g\,cm^{-3}}$. The time and distance for each snapshot is expressed in natural unit of $M = 1.47 \cdot 10^{-2} \times (M_{\rm NS}/1.625 M_{\rm Sun})\,{\rm ms} = 4.43 \times (M_{\rm NS}/1.625 M_{\rm Sun})\,{\rm km}$. More details can be found in [115].

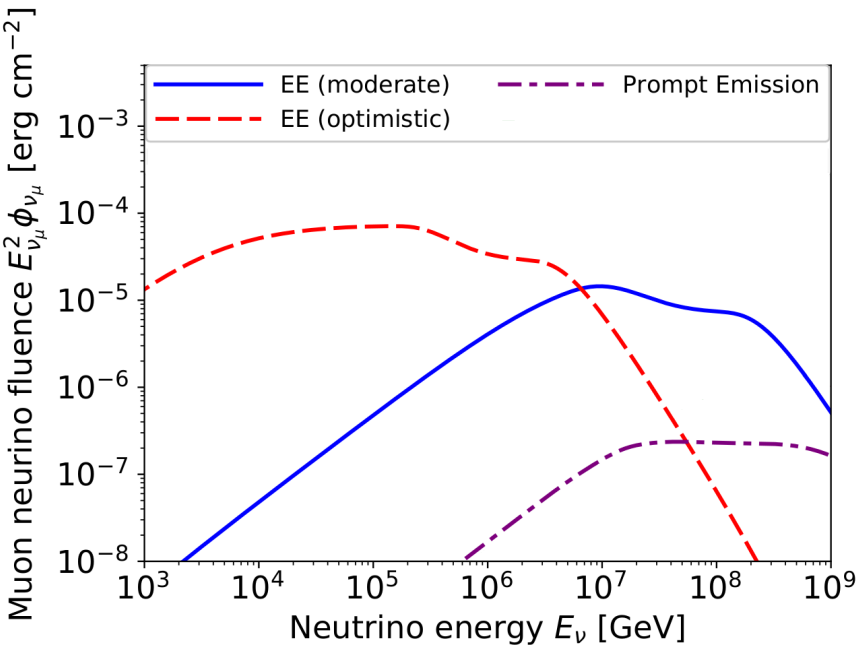

Figure 8.5 – Neutrino fluences from extended emission (EE) for the moderate and optimistic models as well as prompt emission from a short γ-ray burst seen on-axis at a distance of 300 Mpc. Adapted from [114].

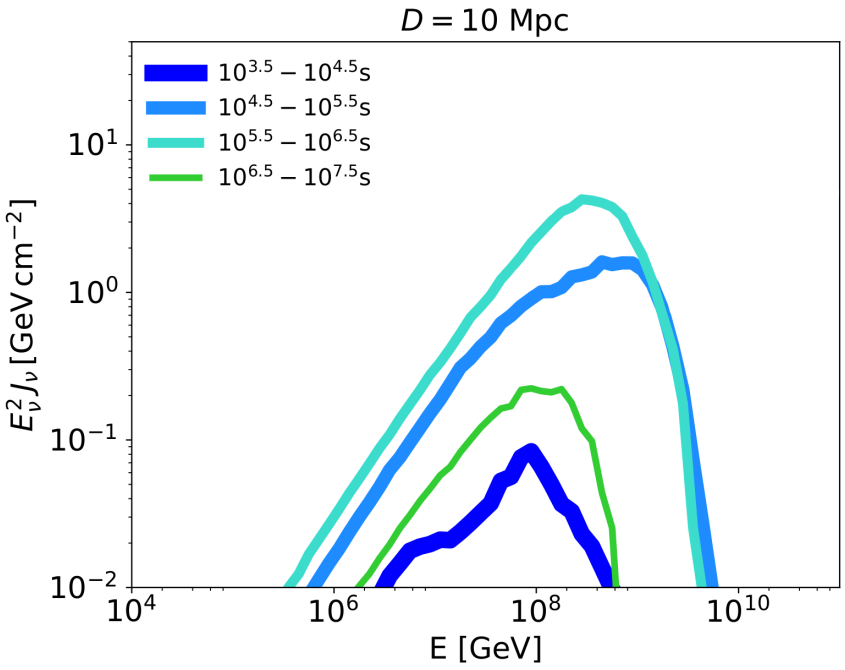

Figure 8.6 – Neutrino fluence from a stable millisecond magnetar on time-scales from an hour to a year. The fiducial magnetar model assumes an initial spin period of 1 ms, a surface dipole magnetic field of 10^{14} G, an ejecta mass of 0.01 M_{Sun} and a source distance of 10 Mpc. Adapted from [112].

a neutrino detection with a characteristic light curve would give evidence of the presence of a long-lived neutron star remnant [112]. X-rays could also point out the presence of a magnetar.

The matter ejected by the magnetar takes the form of a powerful magnetized wind thanks to the strong electromagnetic fields powered by the enormous rotational energy of the magnetar. In the hours to days following the coalescence, these relativistic winds inflate a magnetized nebula in which particles can be accelerated to ultra-high energies. Three processes are considered: the *surf-riding* of a particle on the magnetized wind, the magnetic reconnection process in the equatorial layer and later the Fermi acceleration at the termination shock.

At early times, synchrotron cooling of the protons is very important because of the strong magnetic fields, it suppresses neutrino production. It is after roughly a day that high-energy neutrinos are produced efficiently as $p\gamma$ interactions with thermal photons comes to dominate in the nebula. The emission peaks ~4 days after the merger with an energy of ~10^{18} eV. After a week or so, cosmic rays escape the source without secondary production as the thermal photon density decreases sufficiently. For this reason, we searched for late neutrino emissions in a time-window of 14 days following the merger. The predicted neutrino fluence can be seen in figure 8.6 for different time windows after the merger.

These prompt, extended and late neutrino emissions have been searched for by Antares, IceCube and the Pierre Auger Observatory for the GW170817 event presented in chapter 9.

8.3 Gravitational Waves

Gravitational waves are a prediction of the General Relativity theory published by Einstein in 1915 [118]. General Relativity describes gravity as a geometric property of spacetime with Einstein's equation

$$G_{\mu\nu} = -\frac{8\pi G}{c^4} T_{\mu\nu}, \tag{8.1}$$

$G_{\mu\nu}$ being the Einstein tensor which describes the geometry of spacetime. It is determined by the matter-energy distribution described by the stress-energy tensor $T_{\mu\nu}$. The row and column indices μ and ν are running from 0 to 3. The parameter G is the universal gravitational constant and c the light velocity in vacuum.

As an analogy with electromagnetic emissions of accelerating dipole, gravitational waves are emitted when the mass-energy quadrupole moment of a system is accelerating. For instance, a system formed of two close and large masses orbiting each other around a barycentre (e.g. a binary system of neutron stars or black holes) is an effective gravitational wave emitter. On the contrary, the rotation of a spherically symmetric system does not emit gravitational waves as its quadrupole moment is constant.

In the hypothesis of a small perturbation, which is valid for Gravitational waves, Einstein's equation can be linearised as

$$g_{\mu\nu} = \eta_{\mu\nu} + h_{\mu\nu}, \tag{8.2}$$

with $||h_{\mu\nu}|| \ll 1$ being the gravitational wave amplitude and $\eta_{\mu\nu}$ the flat space Minkowski metric.

One can show that the general solution is a superposition of monochromatic plane waves. For a gravitational wave propagating along the z axis, it can be written as

$$h_{\mu\nu} = \begin{pmatrix} 0 & 0 & 0 & 0 \\ 0 & h_+ & h_\times & 0 \\ 0 & h_\times & -h_+ & 0 \\ 0 & 0 & 0 & 0 \end{pmatrix} e^{i(\mathbf{k}\cdot\mathbf{x})}, \tag{8.3}$$

$\mathbf{x}$ being the four-vector position and $\mathbf{k}$ the four-wavevector. The parameters h_+ and $h_\times$ are the so-called *plus* and *cross* polarizations whose effect on free-falling masses is represented in figure 8.7. This spacetime distortion, amplified in the figure, is of the order of 10^{-21} which is equivalent to a distortion of the size of a hair width on the distance between Earth and Alpha Centauri.

The (rarely shown) combination of both polarizations in the case of the coalescence of a binary black hole is represented on Figure 8.8.

8.3.1 Gravitational Wave Detectors

The two advanced LIGO (aLIGO) interferometers were the first to detect a gravitational wave signal in September 2015 [18] and it is in collaboration with the advanced Virgo (aVirgo) detector that the first binary neutron star merger has been detected [19] along with its electromagnetic

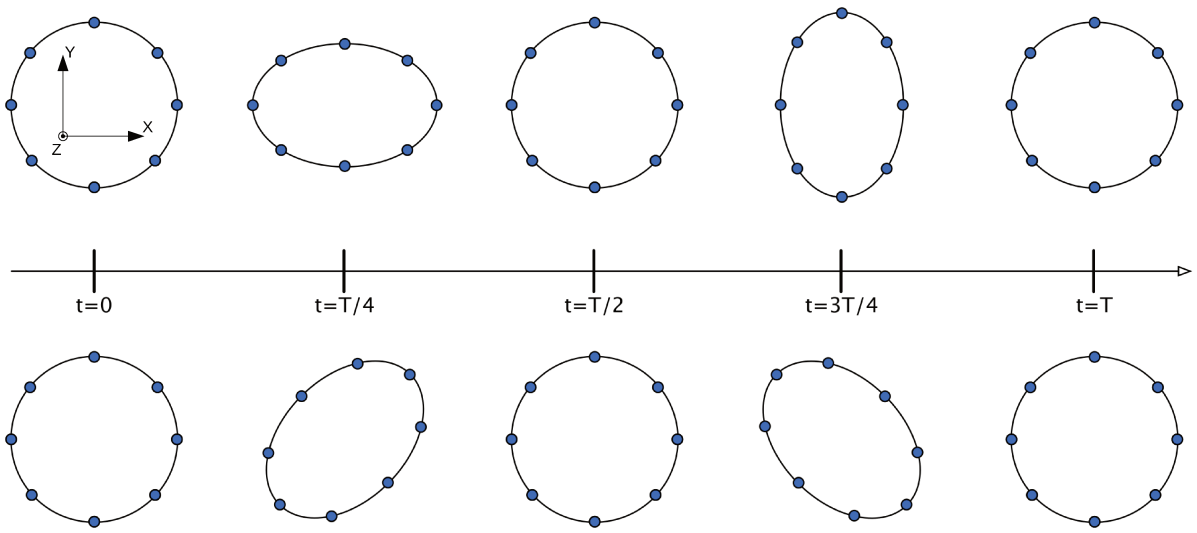

Figure 8.7 – Effect of the plus (top) and cross (bottom) polarizations of a gravitational wave propagating along z on a circle of free-falling masses laid on the x,y plane.

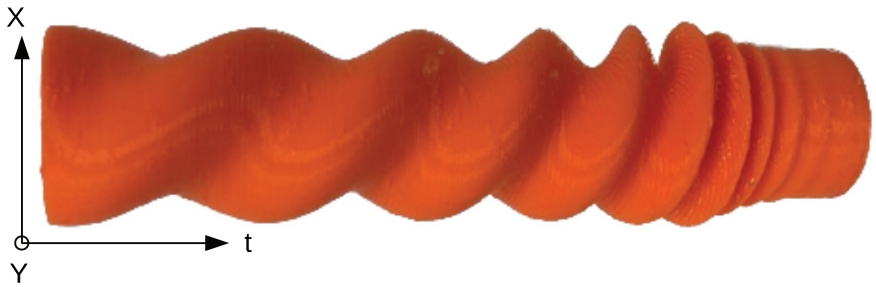

Figure 8.8 – Representation of the gravitational wave from the GW150904 binary black hole merger, the horizontal dimension representing the time evolution [119].

counterpart [20, 21]. These two detectors operate on the same principle of gravitational wave detection by interferometry which is described below.

The relative spacetime deformation along any two orthogonal directions is opposite at all times. This differential effect is exploited by gravitational wave detectors by comparing the length of the two arms of the detector with a Michelson interferometer [120] as illustrated in figure 8.9. The light of the laser beam is split between the two arms of the detector. When a gravitational wave crosses the detector, the length of one arm is shortened while the length of the other is elongated. This will result in a change of the phase of the light at the recombination point and the destructive interferences will become constructive.

This is a simplified picture, the detectors being much more complex in order to stabilize the laser and to improve the sensitivity of the interferometer [121, 122]. In particular Fabry-Perot resonant cavities are used in order to increase the effective length of the arms, the light being reflected few hundreds of times in an arm on average.

An example of signal from a binary merger is shown on figure 8.10 corresponding to the first detected event, so-called *GW150914*. One can see that the amplitude and frequency of the signal increases with time when the distance between the two objects decreases and their angular velocity increases. Then the amplitude starts to decrease when both objects collide.

In order to extract the signal from the data, templates with the shape of expected signals are computed. Then, correlations between templates and data are looked for, this process is called *matched-filtering*. The template having best correlation with data is shown on the second row of figure 8.10 with the residual fluctuations after subtracting the template on the third row. Model-independent algorithms are also used.

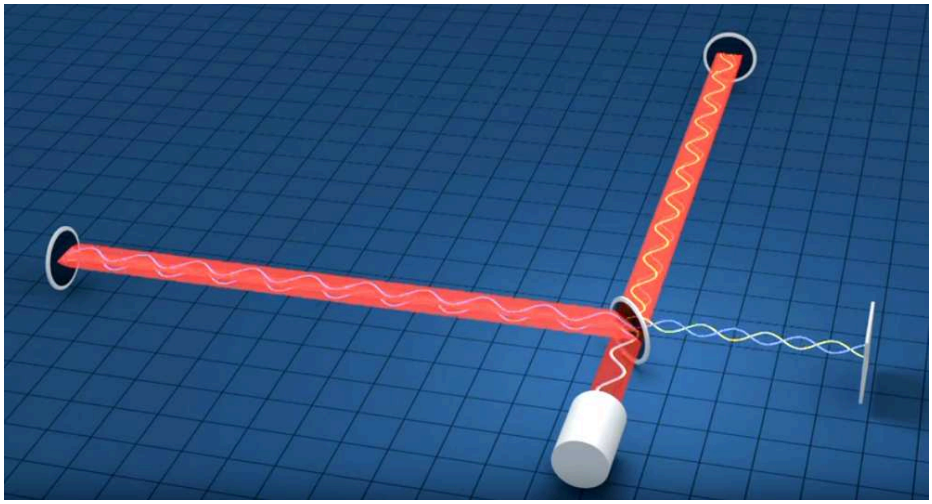

(a) Default configuration, destructive interferences

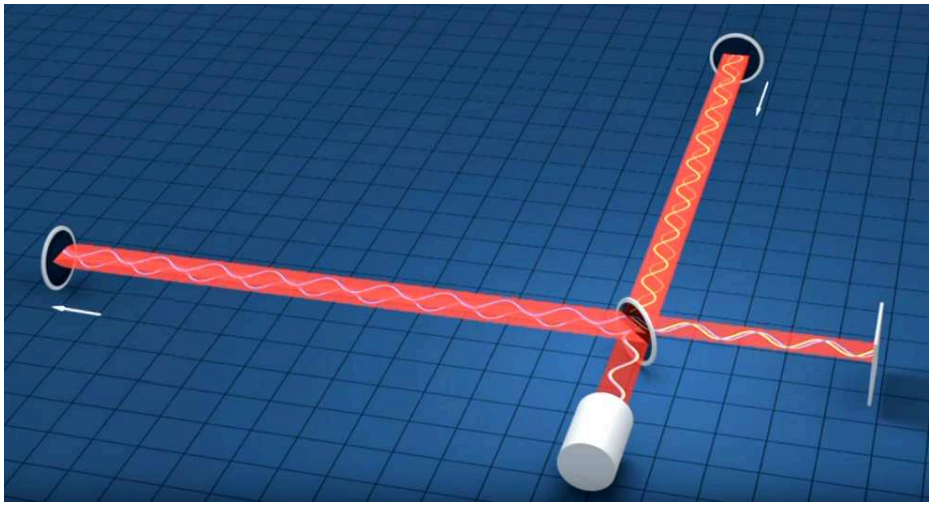

(b) Gravitational wave passes, constructive interferences

Figure 8.9 – Simplified drawing of a gravitational wave interferometer. A laser beam is split in two orthogonal directions by a beam splitter and reflected back by two mirrors, they are recombined by the beam splitter. In the default situation, the recombined beams are interfering destructively (a), if a gravitational wave passes the interferences are constructive (b).

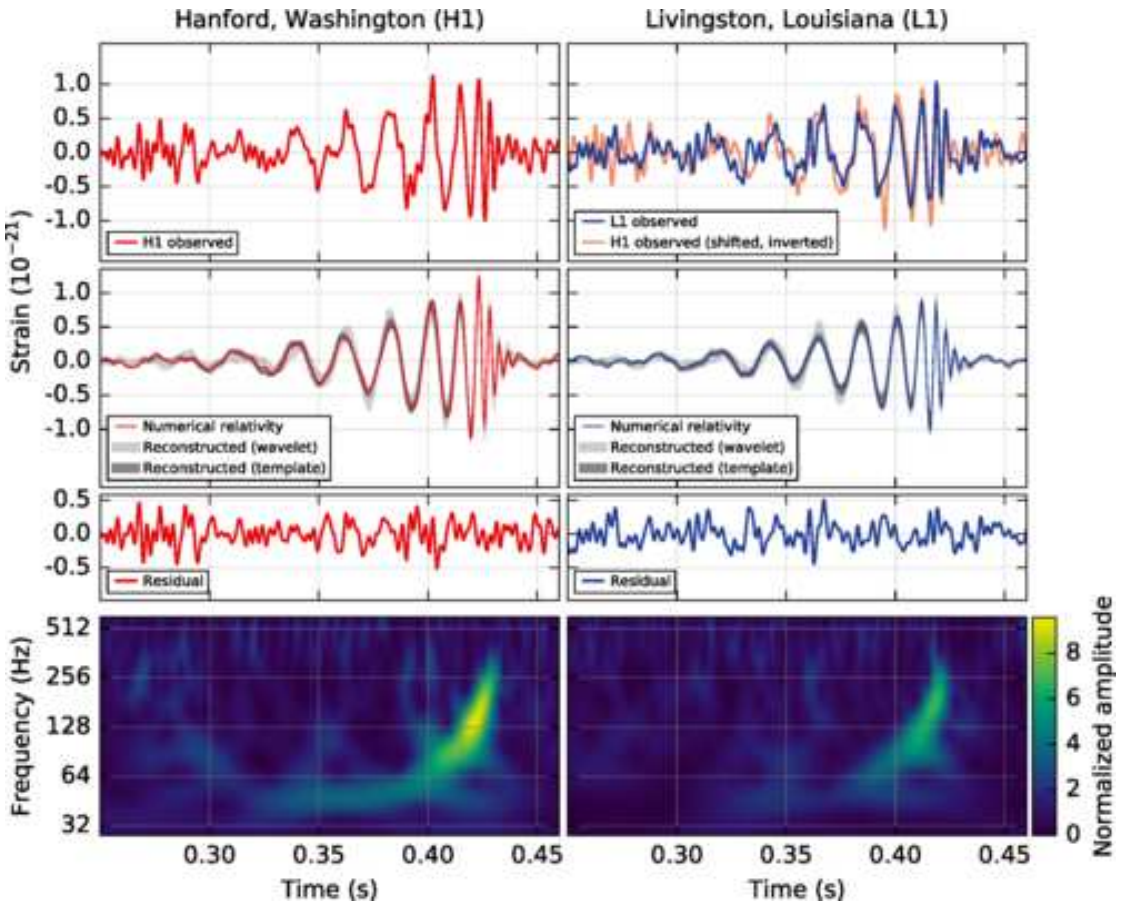

Figure 8.10 – Template fitting of the GW150914 signal. First row: Strain signal of the GW150914 gravitational wave event seen by the LIGO Handford and Livingston detectors. Second row: Template waveform matching the data. Third row: Residual noise after subtracting the template waveform. Bottom row: A time frequency representation of the data [18].

Chapter 9

The Binary Neutron Star Merger

On September 14th, 2015, the LIGO Scientific Collaboration directly observed gravitational waves for the first time in history [18]. This first detection as well as the four following detections [123, 124, 125, 126] (and one lower-significance candidate [127]) resulted from the coalescence of two black holes. It is only on August 17th, 2017 that occurred the first direct detection of a binary neutron star merger, the so-called *GW170817* together with the first detection of an electromagnetic counterpart [20]. This short γ-ray burst surprised the community by being the closest and dimmest of the short γ-ray bursts with known distance. This is probably not a lucky coincidence, but an observation bias. Without the gravitational wave detection, this event wouldn't have been followed and localized and consequently its distance wouldn't have been known. Among the short γ-ray bursts with unknown distances, some are probably similar.

This event will be presented in this chapter as I took part to its neutrino follow-up. Its characteristics and particularities with respect to the previous gravitational wave detections will be developed in a first section. Then, the chronology of the detection and multi-messenger follow-ups of GW170817 will be presented and finally its scientific implications will be summarized in order to underline the exceptional nature of this event.

9.1 GW170817: Characteristics of the Gravitational Wave Event

The GW170817 gravitational wave event occurred seventeen days after the advanced Virgo detector joined the data taking and eight days before the end of the run. It was the last confirmed detection before a one-year break... last but not least!

This event was the first *direct* detection of a binary neutron star merger, almost fifty years after the first *indirect* detection by Hulse and Taylor [128]. As explained in section 8.3.1 the data analysis technique by matched-filtering [129] allows to estimate the two masses of initial objects and the total mass of the system (2.73 to 3.29 stellar masses) as displayed in figure 9.2. The masses measured are in agreement with masses of known neutron stars, by consequence it was the hypothesis considered from the beginning, it was then confirmed by the observation of

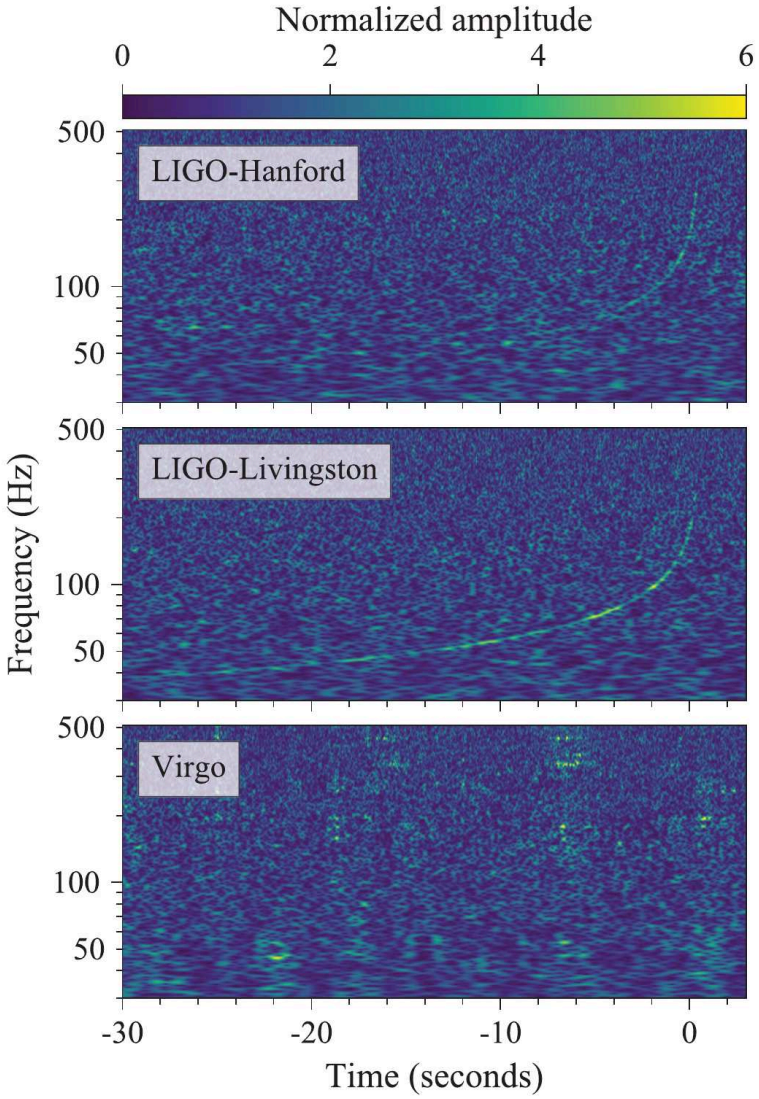

Figure 9.1 – Time-frequency representation of the GW170817 signal observed by the aLIGO-Handford **(top)**, aLIGO-Livingston **(middle)** and aVirgo **(bottom)** detectors. The time is given relative to August 17th, 2017 12 : 41:04 UTC. The amplitude scale in each detector is normalized to the detector's noise amplitude spectral density. This figure is taken from [19].

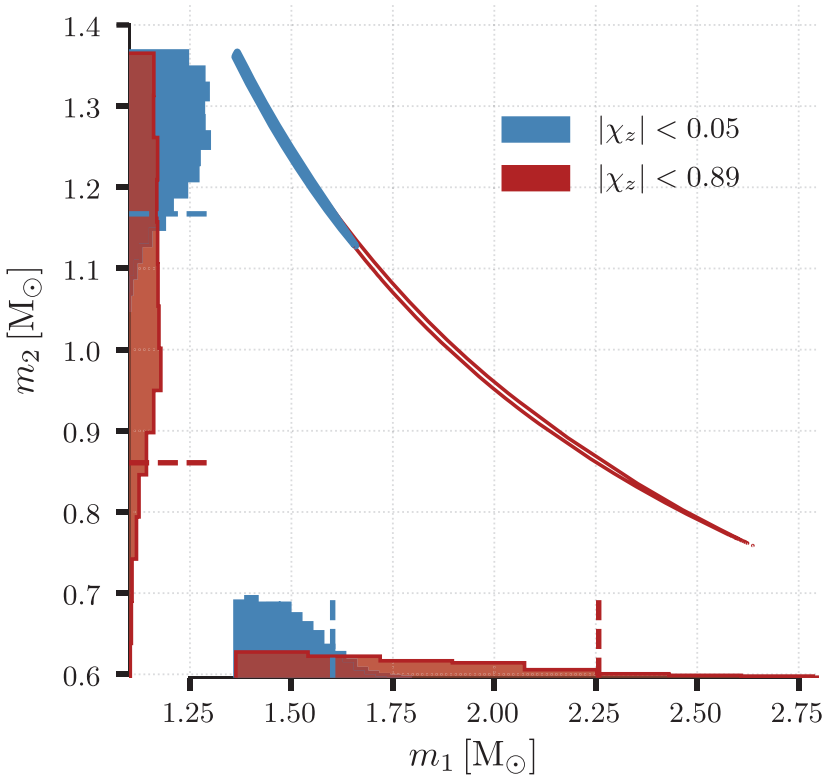

Figure 9.2 – Two-dimensional posterior distribution for the component masses m_1 and m_2 in the rest frame of the source for the low-spin (blue) and high-spin (red) scenarios. The coloured contours enclose 90 % of the joint probability, its shape is determined by a line of constant total mass. The width of the line representing the uncertainty on the total mass. The marginal distributions are shown on axes. Dashed lines enclose 90 % probability away from equal mass of 1.36 M_{Sun}. This figure is taken from [19].

electromagnetic counterparts.

However, it is not known if the remnant object is a black hole or a neutron star. Although figure 9.3 seems to show that the total mass corresponds to the mass of known neutron stars, this figure doesn't account for the error bars on the masses. Adding this information doesn't allow us to conclude on the nature of the remnant. As seen in section 8.2.2, a late neutrino detection would be a proof of the presence of a long-lived neutron star.

This event is also the loudest gravitational wave signal observed with a signal to noise ratio of 32.4 and a false alarm rate of one per $8.0 \cdot 10^4$ years. This can be surprising as a smaller amplitude of the signal is expected from the lower masses of neutron stars with respect to black hole binaries. However this event, localized at a distance of roughly 40 Mpc, was also ten times closer than any previous localized event and the gravitational wave signal amplitude is proportional to the inverse of the distance. Moreover, the merging time-scale being proportional to the inverse of the mass to the power 5, neutron star binary signals are expected to be longer, this was the case for GW170817 which lasted ~100 s which is ~50 times more than the previous longer signal.

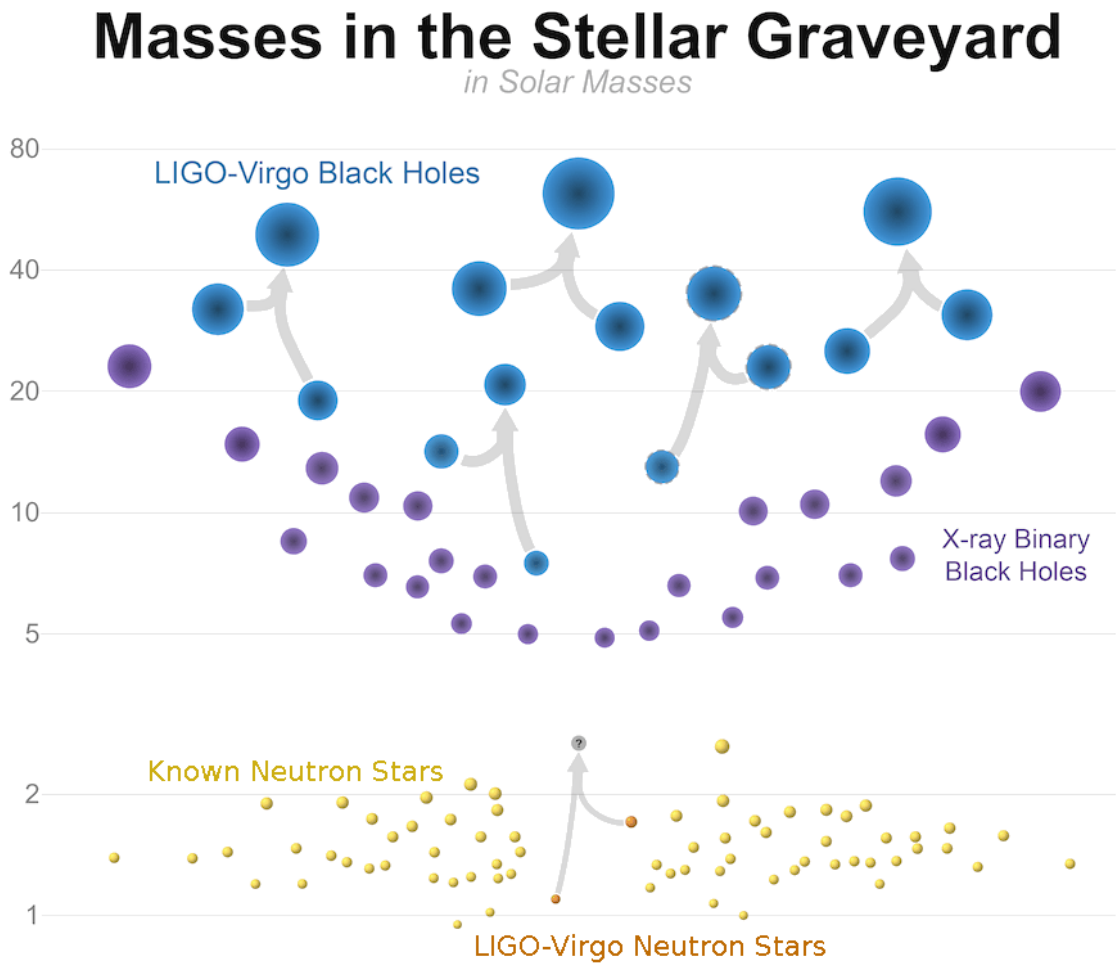

Figure 9.3 – Mass comparison. Masses of black holes detected through electromagnetic (purple) and gravitational-wave (blue) observations, neutron stars measured with electromagnetic observations (yellow), and neutron stars that merged in the GW170817 event (orange). The remnant of GW170817 is unclassified and labelled as a question mark. *Credit: LIGO/Frank Elavsky/Northwestern.*

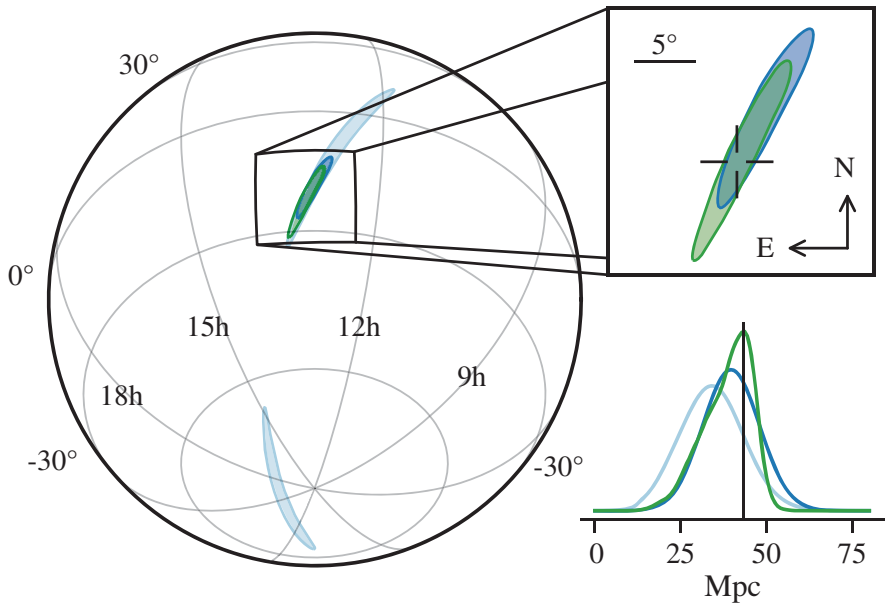

Figure 9.4 – Sky location of GW170817 reconstructed by a rapid algorithm from a Hanford-Livingston (190 deg², light blue contours) and Hanford-Livingston-Virgo (31 deg², dark blue contours) analysis. A higher latency Hanford-Livingston-Virgo analysis improved the localization (28 deg², green contours). The top right reticle marks the position of the apparent host galaxy NGC 4993. The bottom-right plot shows the *a posteriori* luminosity distance distribution from the three localization analyses. The distance of NGC 4993 is shown with a vertical line. This figure is taken from [19].

Thanks to the short distance of this event, it felt inside of the horizon of the three detectors including aVirgo whose horizon is at 52 Mpc for binary neutron stars. Unfortunately due to the orientation of aVirgo, GW170817 could not be seen by this interferometer as shown in figure 9.1. Nevertheless, the non-detection helped to reduce the localization uncertainty of the event as can be seen in figure 9.4. Indeed, the 90 % credible region of the signal (denoted *credible region* in the following) using only aLIGO detectors would have had a size of 190 deg² and thanks to aVirgo it was reduced to 28 deg² [19], the best localization ever achieved with interferometers of that kind.

But on top of this, GW170817 is above all the first event of a new era of expansion of the multi-messenger time-domain astronomy. The different detections of this binary neutron star and its remnant will be developed in the following section.

9.2 Chronology of the Follow-up

Direct gravitational wave detections have always been followed by numerous multi-messenger searches, however none of them has been successful with binary black holes. For this first binary neutron star, an electromagnetic signal has been detected before any alert was sent by the gravitational wave detectors and it has been followed by many more [21]. More than 70 observatories represented on figure 9.5 took part to the multi-messenger follow-up and the paper

Figure 9.5 – Map of the gravitational wave detectors (yellow), light-based observatories (blue) and neutrino telescopes (red) that took part to the detection or follow-up of the GW170817 gravitational wave event.

reporting these has been signed by ~3 500 scientists.

This section will present the chronology of detection of multi-messenger signals coming from the binary neutron star merger GW170817. ANTARES participation in this follow-up will also be introduced in this chronology. In order to make the reading more pleasant, only the first detections of each *messenger* will be stated, however the author does not grant less scientific interest to subsequent detections.

Most of the detections stated below are displayed on figure 9.7 with the corresponding Gamma-ray Coordinates Network (GCN) notices and circulars. The GCN is the network used by astronomers and astrophysicists to distribute informations about γ-ray bursts and transient events. A notice is an alert sent without any humans-in-the-loop while a circular is a prose-style message from follow-up observers reporting on their results. The upper part of figure 9.7 represents the real time detections while the lower part represents the informations sent to the community.

On August 17th, 2017, although the gravitational wave signal happened before, the *Fermi* Gamma-ray Burst Monitor (*Fermi*-GBM) was the first experiment to send a public alert to the community [130] at 12:41:20 UTC, 14 s after the detection. The event, shown in figure 9.6, was seen with a 4.8 σ significance and a rough localization of the event with a 3 200 deg^2 credible region.

In the meantime, the low-latency binary-coalescence search was identifying the gravitational wave signal in the aLIGO-Handford data. The detected coalescence finished at t_c = 12:41:04 UTC and at this time the Livingston detector was saturated by a glitch, as for aVirgo, its low-latency data transfer was delayed. Nevertheless, a GCN notice has been released 27 min after the merger and 13 min later the GCN circular N° 21505 [131] linked this event with the γ-ray burst seen by *Fermi*-GBM at t_c + 1.7 s. The attempt to localize the event with one detector

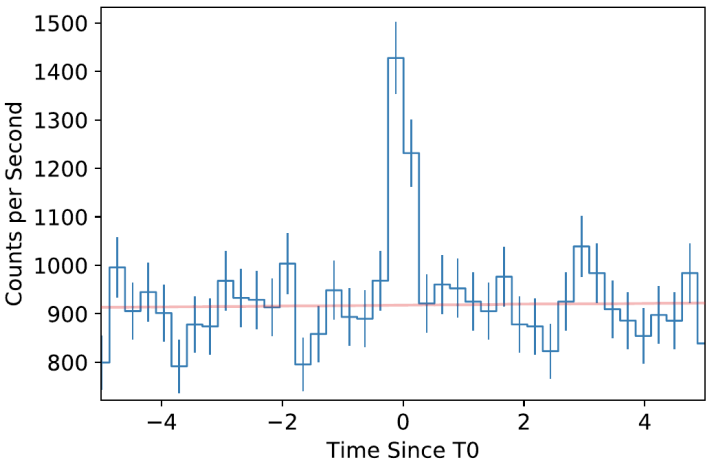

Figure 9.6 – Light curve of GRB 170817A measured by *Fermi*-GBM in the 50 to 300 keV band. The red band is the background estimate. [20]

Figure 9.7 – Timeline of the multi-messenger observations of the GW170817 event (green) as well as the Gamma-ray Coordinates Network (GCN) notices (blue) and circulars (red) sent subsequently in the 18 hr following the event. The ANTARES GCN circular is represented in orange.

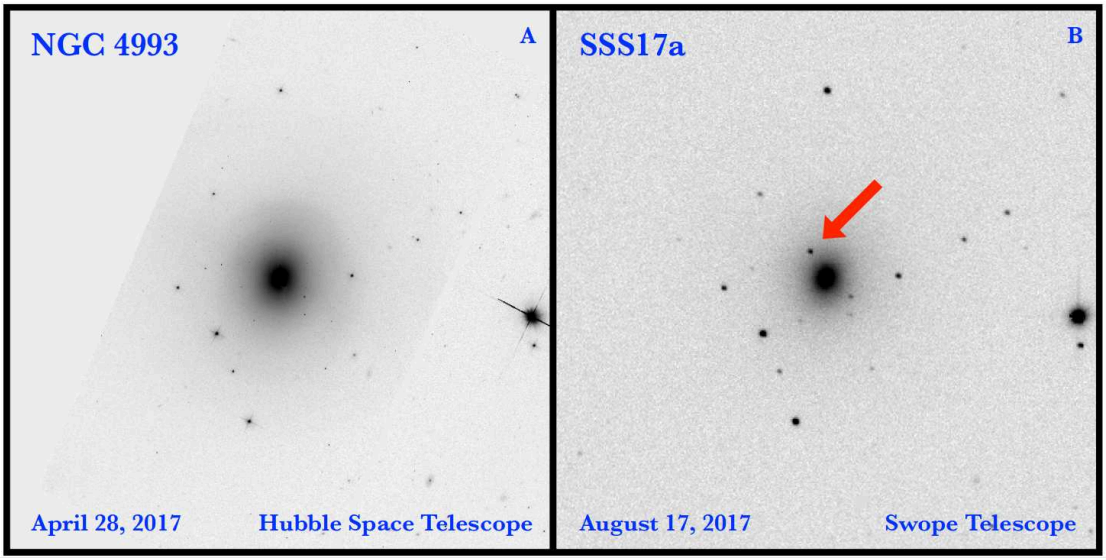

Figure 9.8 – 3′ × 3′ images centred on NGC 4993 with North up and East left. Panel A: Hubble Space Telescope image from four months before the merger. **Panel B:** Swope image of the binary neutron star remnant denoted as SSS17a on August 17th, 2017 at 23:33 UTC. SSS17a is marked with the red arrow [135].

lead to a credible region much broader than the *Fermi*-GBM one.

It is from these measurements that ANTARES started a search for a neutrino counterpart using the online sample of upward-going tracks. At this time the credible region of *Fermi*-GBM and aLIGO-aVirgo were partly in the ANTARES field of view. However, in parallel LIGO Scientific Collaboration removed the background from the aLIGO-Livingston detector and Virgo Collaboration processed their data. With the data of the three interferometers, the credible region was reduced to 31 deg^2 [132]. As a consequence, the localization of GW170817 was not in the ANTARES field of view any more when the results of the online analysis were sent [133], eight hours after the merger detection. No neutrino event were seen either in a time window of ± 500 s around the coalescence time t_c nor in a more extended time window of ± 1 hr. This analysis will be developed in section 10.1.2.

The optical telescopes strategy was to target galaxies inside of the three-dimensional localization of the event accounting for their stellar mass and star formation rate. The localization using the three gravitational wave detectors reduced a lot the number of targeted galaxies but the credible region was not in the field of view of the terrestrial telescopes before ten hours and the Chilean night. The spatial telescopes have a narrower field of view and did not follow this event before it was well localized. It was the 1 m Swope Telescope that first detected light at 23:33 UTC [134] and located the event in the galaxy NGC 4993 as can be seen in figure 9.8. Five other optical detections followed within an hour.

The Rapid Eye Mount/ROS2 detected the first near-infrared signal 12.7 hours after the coalescence followed by ultraviolet detection by the UVOT instrument on-board *Swift* satellite at t_c + 15.3 hr. These observations were continuous during the following days and showed an unusual rapid luminosity decline in UV-blue and brightening of the near-infrared emission. This

evolution, characteristic of a kilonova, is considered unprecedented by the community for a transient event in nearby universe and makes this event even more interesting.

At t_c + 4 days, ANTARES sent the GCN circular N° 21631 [136] reporting the results of a search for downward-going tracks, as the merger was in the downward-going field of view at t_c. As developed in section 10.2.1, no event spatially correlated with the merger passed the cuts neither in the ± 500 s nor in the ± 1 hr time windows.

X-ray and radio observations are very useful to constrain the geometry of the ejecta, energy output as well as the orientation of the system and the environment of the merger. During the first days neither X-ray nor radio emissions had been detected and limits were put. It is only nine days after the event that the first X-ray counterpart was detected by *Chandra* and seven days later for the first radio counterpart with the Jansky Very Large Array.

These multi-messenger searches have important physical implications that will be developed in the following section.

In parallel, ANTARES started two offline analyses onto which I have contributed by adding sensitivity to all the neutrino flavour events using the shower sample on a ± 500 s time window around the merger time and + 14 days after the coalescence. These analyses will be developed in sections 10.2.2 and 10.2.3.

9.3 Physics Implications

The GW170817 event, has great implications on astrophysics by its nature and unexpected properties identified from the wealth of data collected. Moreover, its nearly coincident detection in gravitational waves and photons allows to test gravity in many ways as well as to use it as a standard siren to measure the Hubble constant. Some of the most important results will be summarized in this section.

Astronomical Implications

The most important implication of GW170817 is probably the *kilonova* detection. A kilonova is the electromagnetic emission observed hours to days after the merger as represented in figure 9.9. This emission results from the heating of the ejecta by radioactive decay of heavy elements produced by r-process. The r-process (r for rapid) is the main mechanism of synthesis of atomic nuclei heavier than iron. These nuclei are not stable, therefore the neutron capture must be rapid so that the newly formed nucleus does not undergo β-decay before another neutron is captured. By consequence it occurs in neutron-rich environments like matter thrown off from the merger.

The nucleosynthesis of heavy elements is one of the key question in nuclear astrophysics. Before this detection the major candidate for nucleosynthesis of heavy elements was core-collapse supernova, however simulations were not able to produce the heaviest elements. This measurement shows that the coalescence of a binary neutron star system is a very good candidate, the data matching perfectly the models as can be seen in figure 9.9. The astrophysical

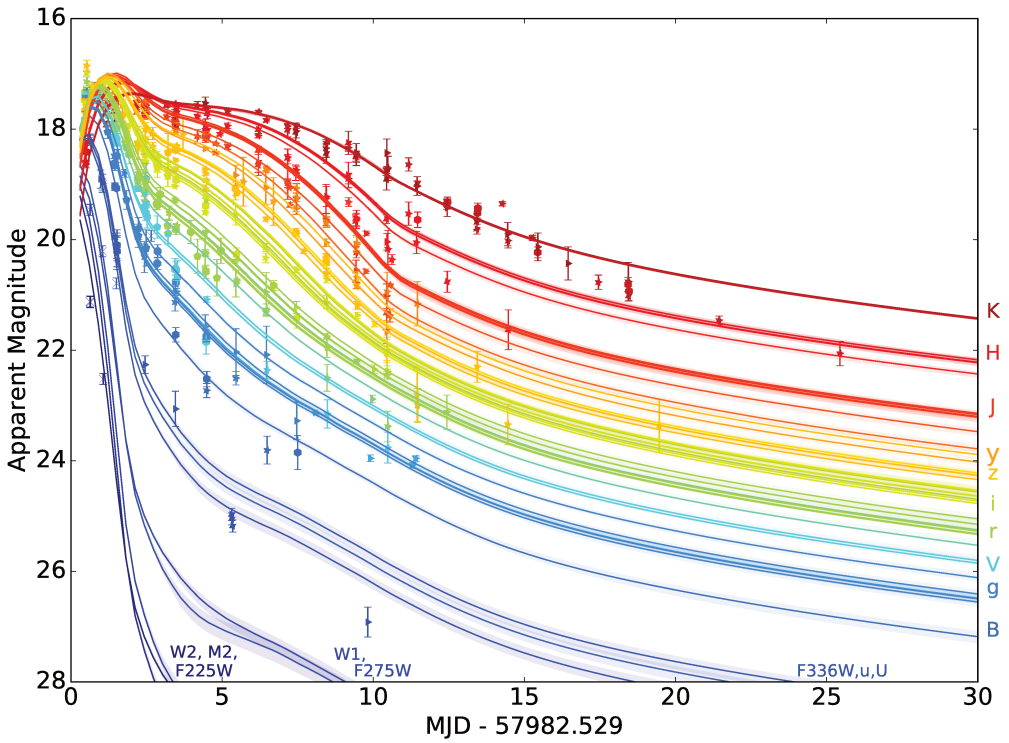

Figure 9.9 – Kilonova light curves. Ultraviolet, optical and infrared light curves for days after the merger along with the kilonova models with the highest likelihood scores. [137]

origin of each element can be seen in figure 9.10 illustrating the importance of merging neutron stars in nucleosynthesis.

Thanks to the *Fermi*-GBM detection, GW170817 also confirms the long-standing hypothesis that binary neutron stars are linked to short γ-ray bursts and allows to revise expectation rates for joint gravitational wave-electromagnetic detections of binary neutron stars [20].

Before GW170817, uniform jets with sharp edges have been widely used to describe γ-ray bursts as it is the simplest model. But for this event, a uniform sub-luminous jet seen on-axis (figure 9.11 (A)) cannot explain the late rise of radio emission. The scenario of a standard (luminous) jet seen off-axis (figure 9.11 (B)) is also ruled out as the rise of the late radio emissions is too slow [138]. This afterglow emission results from the interaction of the jet with the circum-merger medium.

The particularities of this event forces us to consider more complex models [138, 139]. The interaction of the jet with the ejecta surrounding the merger can give rise to a mildly relativistic cocoon ($\gamma \approx 2$–3) which explains well the low-luminosity γ-ray emissions. The jet can be chocked if it does not escape from the ejecta (figure 9.11 (C)), this scenario explains well the observations. The scenario of a successful jet (figure 9.11 (D)) is not favoured. Indeed, theoretical predictions suggest that the cocoon and jet should have comparable energies. This should result on the observation of the jet signature in the radio band that has not been observed. But this scenario can also be visualized as a structured jet, with a Lorentz factor decreasing with the angle. This

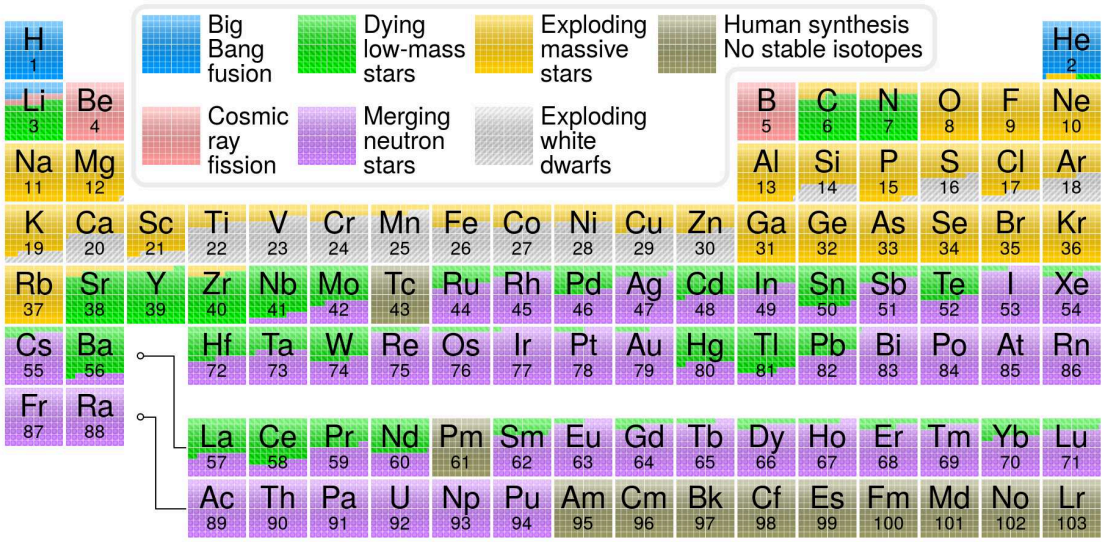

Figure 9.10 – Periodic table indicating the main origin of elements found on Earth. The elements with Z > 94 are mainly of human synthesis. Diagram by Cmglee, distributed under a CC-BY 2.0 license.

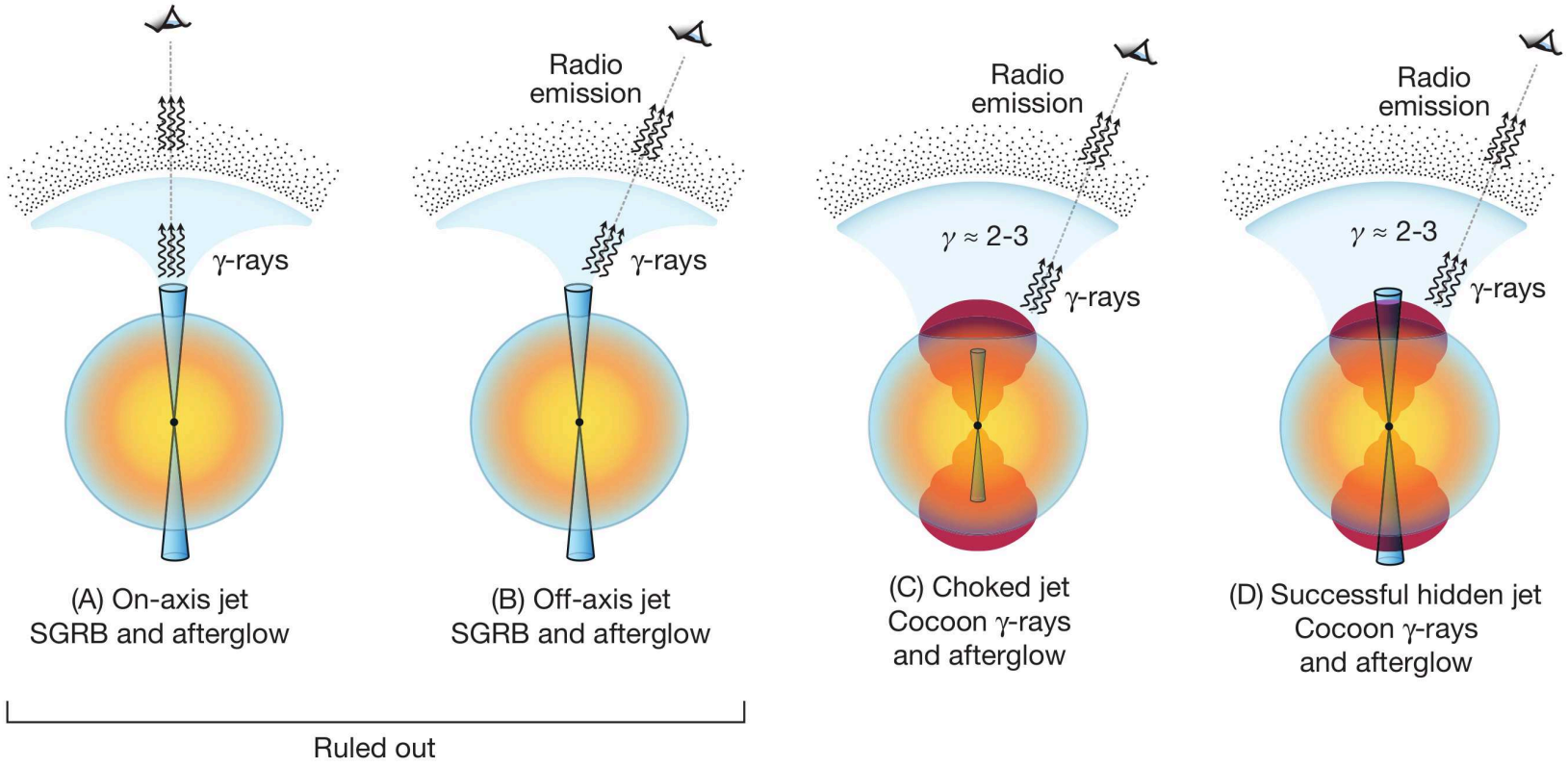

Figure 9.11 – Potential jet and dynamical ejecta scenarios. The blue cones are the jets released by the merger represented by a black point. The spherical ejecta is represented in orange and the cocoon in red. The black dotted region represents the circum-merger environment. The eye indicates the line of sight of the observer. See the text for the scenario description. Adapted from [138].

scenario allows to explain well the observations. It is the long-term radio and X-ray observations that will allow to choose between the chocked and structured jet scenario. More details can be found in [138] and references therein.

The GW170817 event can also be used as a standard siren to measure the Hubble constant [140] in an new independent way. The luminosity distance obtained from the gravitational wave data is used with the redshift of the electromagnetic signal to measure a value of $70.0^{+12.0}_{-8.0}\,\mathrm{km\,s^{-1}\,Mpc^{-1}}$. It is consistent with existing measurements of 70–73 $\mathrm{km\,s^{-1}\,Mpc^{-1}}$ [141] although less precise. However the precision of this measurement will improve to $69^{+2}_{-4}\,\mathrm{km\,s^{-1}\,Mpc^{-1}}$ after 25 observations [142].

Gravitation Tests

As mentioned earlier, this event allowed also to test some theoretical predictions about gravitation. For example, measuring a γ-ray counterpart only 1.7 s after the merger, knowing the distance of the event allows to constrain the difference between the speed of the gravitational waves and the speed of light to be between $-3 \cdot 10^{-15}c$ and $+7 \cdot 10^{-16}c$ [143].

The time delay between the two signals can also be used to test the weak equivalence principle using the Shapiro effect. The weak equivalence principle states that the inertial mass is equal to the gravitational mass, and the Shapiro effect predicts that the propagation time of massless particles in curved spacetime increases with respect to flat spacetime. But as the inertial mass is made up of several types of mass-energy (rest energy, electromagnetic energy…), if one type contributes to gravitational mass differently it would violate the weak equivalence principle and result in a different delay [144].

9.4 Conclusion

Thanks to the collaboration of around 3 500 scientists, this event detection and its follow-up brought unexpected results as well as confirmations of theoretical predictions. More events of this type should be detected in the following years to confirm or improve these results.

For some of the next detections, one can hope that events will be detected by the three improved interferometers which would lead to an even better localization of the event. A shorter time delay before the first optical detection can also be expected for events falling in the field of view of terrestrial telescopes. Finally, events falling inside of the upward-going field of view of the Antares and/or IceCube neutrino telescopes would lead to better constraints on a potential neutrino emission and potentially a detection. A neutrino detection would allow a localization of the event with a typical position uncertainty of ~1 $\mathrm{deg^2}$ within minutes. This would allow a better and earlier multi-messenger follow-up, in particular by the small field of view telescopes.

Chapter 10

Search Method

The ANTARES follow-up of GW170817 has been done in three stages that are described in this chapter. A first online analysis has been carried out within a few hours after the merger using upward-going tracks. In the mean time the localization of the event has been refined by the LIGO-Virgo collaborations, with the consequence that the event was finally not in the ANTARES field of view. To account for this, a second analysis has been designed using downward-going tracks which was released within a few days. These two first analyses are described briefly in sections 10.1.2 and 10.2.1.

A third part of this follow-up with two analyses, to which I included the shower sample for the first time in a transient analysis, is described into more details in sections 10.2.2 and 10.2.3. This part describes a search over a short time window using downward-going events and another over a longer one using upward-going events. This third part has been done in parallel with ICECUBE and Pierre Auger collaborations and published together. The ICECUBE and Auger methods will be briefly detailed in sections 10.3 and 10.4.

The background rejection of these analyses profits from the transient nature of this event by selecting neutrinos occurring on a certain time window around or after the event. The localization is also used to efficiently reject the background by selecting events falling close to the source. Thanks to that, the quality cuts can be relaxed except for the search over 14 days.

10.1 Online Follow-up

The online neutrino follow-up is used in a multi-messenger perspective. As most experiments have a small viewing angle, having a precise localization of the event is fundamental to allow them to point to the source and collect data during the transient phase. This is the main goal of the online part of the neutrino follow-up, the detection of a neutrino would reduce the region of interest to typically one square degree. Moreover, the detection of a source by a neutrino experiment would be a hint for significant cosmic ray acceleration.

But the online data set cannot profit from the precise calibrations which are produced afterwards for offline analyses. Consequently, the event reconstruction has been adapted.

10.1.1 Online Reconstruction Algorithm

The online algorithm relies on a charge calibration [145] with a month granularity and no positioning calibration. It initially aimed at reconstructing signal-like events to send alerts to the community through the *TAToO* system (Telescopes and ANTARES Target of Opportunity). Only track events are reconstructed online as they provide the best pointing power. It is designed to be robust and fast in order to process all data in real time. The reconstructed direction of a track is available within 10 ms.

As it cannot rely on the dynamical positioning alignment, an idealized detector geometry is used which does not consider the orientation of the storeys and the difference of line shape due to the sea current.

A fast reconstruction algorithm is used to reject most of the downward-going events. It merges the hits of the three optical modules of a storey assigning their location to the barycentre of the storey. Then it minimizes a χ^2 comparing measured hit times and positions to the expected ones from the light induced by a muon Cherenkov track, which is assumed to be a straight line. Events reconstructed as downward-going are rejected and the fitted value of the χ^2 is used as a quality parameter Q to remove badly reconstructed tracks in general and atmospheric muons reconstructed as upward-going in particular.

A neutrino purity better than 90 % is achieved with a cut in the track fit quality of $Q < 1.4$ while keeping 48 % of the total sample of upward-going neutrinos. Above 10 TeV a median angular resolution of 0.5° is reached [146].

10.1.2 Online Analysis

The low-latency search for a neutrino counterpart to GW170817 aimed at providing the LIGO/Virgo electromagnetic partners with the location of a potential counterpart as fast as possible. Therefore, the selection cuts have not been optimized for this analysis and no Monte Carlo simulation has been produced. The online upward-going track sample has been used as is.

As explained in section 9.2, initially, the probability map of the gravitational wave event was computed using the aLIGO Hanford data only and a large part of the 90 % probability contour map of the event was in ANTARES field of view. Therefore, we performed a search for prompt neutrino emission in a time window of ± 500 s around the event time as presented in section 8.2. We looked for any event in ANTARES field of view. No events were seen as expected from the background rate of 10^{-2} neutrinos over the time window. Then an extended search within ± 1 hr has been performed not giving any coincidence either.

A refined map sent by LIGO/Virgo showed that the event was not in the ANTARES field of view as can be seen in figure 10.1. Unfortunately it has been released before the publication of these ANTARES results in the GCN Circular N° 21522 [133] however ANTARES upward-going events were still compatible with the *Fermi*-GBM signal.

The GCN Circular has been sent eight hours after the event and four hours before the first GCN Circular announcing the detection of the optical counterpart to GW170817, hence a neutrino detection would have enabled to pinpoint the source location 30 % earlier. This would have profited for example to X-ray satellites like *Chandra* or XMM-*Newton* that have a very small field

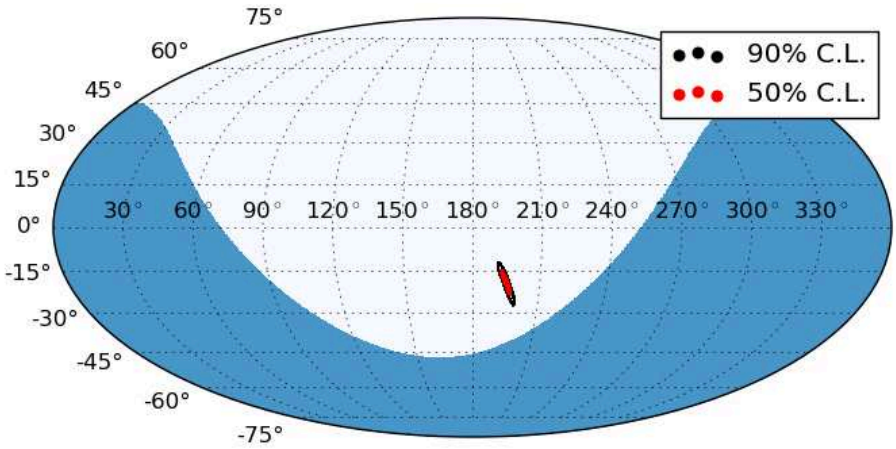

Figure 10.1 – ANTARES visibility at the time of the alert is shown in blue, for upward-going events, together with the 90 % (50 %) contour of the probability map of the event in black (red).

of view. An early X-ray observation would have constrained the cocoon or structured jet emission models described in section 9.3.

10.2 Offline Follow-up

In a second phase, once the source was localised offline follow-up searches allowed to use the usual reconstruction algorithms after proceeding to a full calibration of the detector in terms of positioning [49], timing [48] and efficiency [46]. In particular due to the location of the counterpart above the ANTARES horizon, the downward-going events have been exploited. The shower sample has also been used in order to exploit at best the ANTARES potential. The optimization of the selection cuts was also made possible thanks to a boosted Monte Carlo production with ten times more events.

In what follows, the signal is simulated as a point-like source at the position of GW170817 generating a neutrino flux $\propto E^{-2}$.

10.2.1 Downward-going Follow-up Tracks

A search for downward-going tracks coming from above the ANTARES horizon as been performed for the second time in the ANTARES history [124], indeed such analysis is only possible when looking for neutrino counterpart to transient sources. In this case the sensitivity is reduced but the space and time selection of events correlated with the merger made it possible to reject most of atmospheric muon background.

A neutrino is considered spatially correlated if it is reconstructed inside of the 90 % probability map of the gravitational wave event. For the time correlation, two time windows have been used, ± 500 s and ± 1 hr.

The optimization strategy was chosen so that a neutrino detected in correlation with GW170817 leads to a detection with a 3σ significance level. The point source cuts are used [99], with the cut on the angular error estimate β_{Tr} fixed to $\beta_{\text{Tr}} < 1°$. A cut on the number of hits used by the reconstruction (which can be considered as a proxy for the neutrino energy) is also used. Then, the optimization is done on the reconstruction quality estimator Λ_{Tr} and the number of hits. The optimized values of these cuts for the ± 500 s time window are $\Lambda_{\text{Tr}} >$ -5.8 and $N_{\text{hits}} > 100$. The same cuts are used for the ± 1 hr time window without a new optimisation. The parameters Λ_{Tr} and β_{Tr} and N_{hits} are described in section 2.6. With the chosen set of cuts, an angular resolution of 0.5° at 10 TeV is reached.

No neutrino has been detected in any of the two time windows. These results have been released in the GCN Circular N° 21631 [136], 4 days after the merger.

10.2.2 Shower plus Track: Prompt Emission Search

To further improve the sensitivity to a potential neutrino counterpart, a shower reconstruction was used to search for all flavour neutrino events, for the first time in an ANTARES follow-up analysis, in parallel with the long time-scale emission analysis presented in the following section. These two analyses have been announced together with the official announcement of the GW170817 detection on October 16$^{\text{th}}$ and published on November 30$^{\text{th}}$, 2017, in collaboration with the ICECUBE, Pierre Auger, LIGO and Virgo collaborations.

The optimization strategy is identical for both the track and shower samples. Hereafter, it will be developed for showers on which I worked. The implementation for the track sample will be summarized afterwards.

The goal of this analysis is to search for a prompt neutrino emission, therefore, as for previous analyses, a neutrino will be considered correlated in time if it occurs within the time window of ± 500 s around the time of the merger.

Shower Optimization

Once again the optimization aims at maximizing the signal probability keeping the probability to observe one event from the background smaller than $p_{3\sigma} = 2.7 \cdot 10^{-3}$ so that one event passing the cuts lead to a 3σ detection.

The event selection used for previous point source searches [94] is used here as a basis. However events are selected as downward-going and thanks to the space and time correlation, the β_{Sh} cut can be totally relaxed. The selection cuts can be seen in Table 10.1, the variables are detailed in sections 2.6 and 5.3.

The optimization is done by relaxing the likelihood muon veto cut $\mathcal{L}_\mu$ and optimizing the spatial cut, the *region of interest*, in which events are considered spatially compatible (given the resolution) with the merger. Basically, it is designed as follows: For different radii of the region of interest R_{RoI}, the cut on $\mathcal{L}_\mu$ is optimized to reduce the *background probability* to $p_{3\sigma}$. Then, the R_{RoI} maximizing the signal probability using a E^{-2} spectrum is chosen. This will be developed in what follows.

As seen in section 5.3.2, $\mathcal{L}_\mu$ was introduced as a likelihood ratio between cosmic showers and atmospheric muons that is defined from an upward-going sample. To make a consistent

Table 10.1 – List of the selection cuts applied for showers. The usual cuts are defined in section 5.3.2. R_{RoI} is the angular distance of the event to the source and $|t_{\mathrm{evt}} - t_{\mathrm{src}}|$ the time between the merger and the neutrino candidate.

Criterion	Condition
Triggered	T3 or 3N
Track Veto	Not selected as a track
Containment	$\rho_{\mathrm{Sh}} < 300$ m, $\lvert z\rvert < 250$ m
Downward-going	$\cos(\theta) > 0$
M-Estimator	$M_{\mathrm{Est}} < 1000$
RDF from Dusj	$\mathcal{L}_{\mathrm{Dusj}} > 0.3$
Muon Veto	$\mathcal{L}_{\mu} > -13$
Time correlation	$\lvert t_{\mathrm{evt}} - t_{\mathrm{src}}\rvert < 500$ s
Spatial correlation	$R_{\mathrm{RoI}} < 24°$

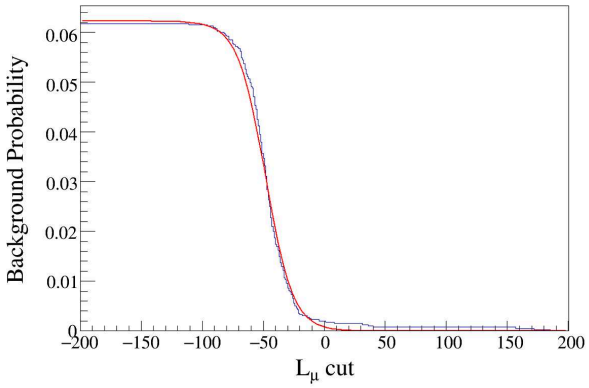

Figure 10.2 – Probability to detect a background event correlated in space and time as a function of the cut on L_{μ} for a time slice of 1000 seconds and a radius of the region of interest of 24°.

use of $\mathcal{L}_{\mu}$ here, it has been redefined using the same probability density distributions but from a downward-going sample.

The optimization on $\mathcal{L}_{\mu}$ is done from the curve represented on figure 10.2 which shows the probability to have a background event correlated with GW170817 as a function of the cut on $\mathcal{L}_{\mu}$. It comes from the anti-cumulative distribution of $\mathcal{L}_{\mu}$ for atmospheric muons and neutrinos from the Monte Carlo simulation. All downward-going events of the run are used, with the approximation that the background rate is constant on all the field of view and all the run[1]. Then the curve is rescaled to match the data: the number of events before the cut on $\mathcal{L}_{\mu}$ is scaled to the corresponding number of events in the dataset (25 events). Then, this is rescaled to the 1 000 s time window and to the region of interest. Finally, this is fitted by a hyperbolic tangent to get the value of the cut leading to a probability to detect a background event of less than $p_{3\sigma}$.

For each pair of (R_{RoI}, $\mathcal{L}_{\mu}$), the acceptance is computed. The acceptance being defined as the constant of proportionality between the signal flux normalization and the expected number of signal event. The pair of (R_{RoI}, $\mathcal{L}_{\mu}$) maximizing the acceptance is chosen as shown in Ta-

[1]This would have a small impact on the significance of a potential detection but not on the upper limit set.

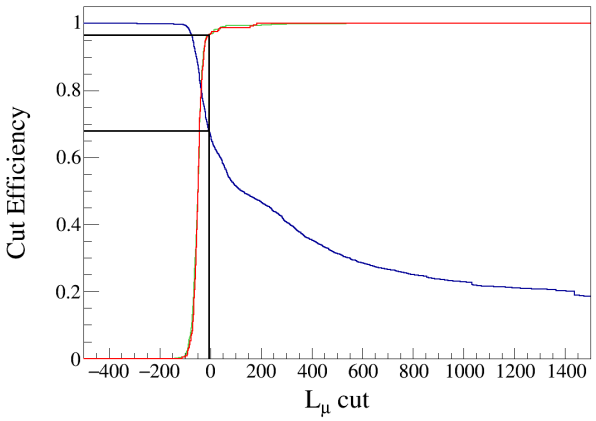

Figure 10.3 – Proportion of remaining signal and rejected background after the cut on $\mathcal{L}_\mu$. Blue: remaining astrophysical neutrinos, Red: rejected atmospheric muons, Green: rejected atmospheric neutrinos. The black lines show the values corresponding to the cut on $\mathcal{L}_\mu$ of -13.

Table 10.2 – Optimization of the size of the region of interest R_{RoI} and the muon veto $\mathcal{L}_\mu$ by maximizing the acceptance keeping a background probability of $p_{3\sigma}$. The bold line is the maximum.

R_{RoI}	$\mathcal{L}_\mu$ cut	Acceptance
20°	-17	0.655
21°	-16	0.655
22°	-15	0.655
23°	-14	0.656
24°	**-13**	**0.660**
25°	-12	0.657
26°	-11	0.650
27°	-11	0.651
28°	-10	0.648

ble 10.2. It results in rejecting 96% of the background keeping 68% of the signal as can be seen in figure 10.3. One can see in figure 10.4 that more than 80 % of the signal events remaining after cuts are contained in a region of interest with a radius of 24°, the median angular resolution being of 6°. The energy range defined as containing 90 % of the signal is [23 TeV, 16 PeV].

Track Optimization

For the track sample, the same optimization strategy is used, Λ_{Tr} being the quality cut which is optimized in parallel with the size of the region of interest. Figure 10.5 illustrates the optimization process, it results on a cut on Λ_{Tr} at -5.5 and a value of R_{RoI} of 1.5°. The final cuts are shown in Table 10.3. The region of interest is much smaller than for the showers thanks to the good angular resolution of the tracks, the median being at 0.5°. Even the energy range is slightly higher for the tracks ([32 TeV, 22 PeV]) contrary to the galactic plane analysis. This is due to the higher muon background to reject in the downward-going track sample, as rejecting background cut in the signal mostly lower energy events.

After unblinding, zero showers and five tracks have been seen in the time window of ± 500 s around the coalescence but none of them felt inside of the region of interest as can be seen in

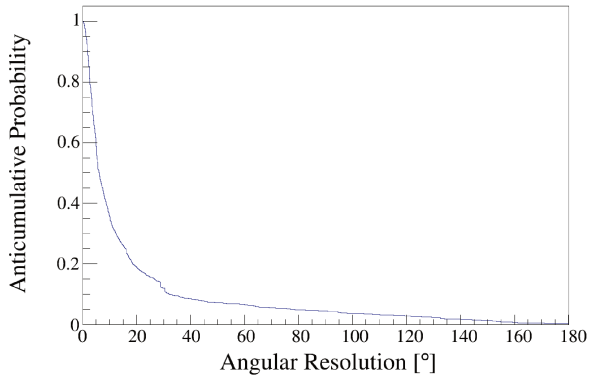

Figure 10.4 – Angular resolution. Probability that a signal event has an angular resolution greater than the value in x.

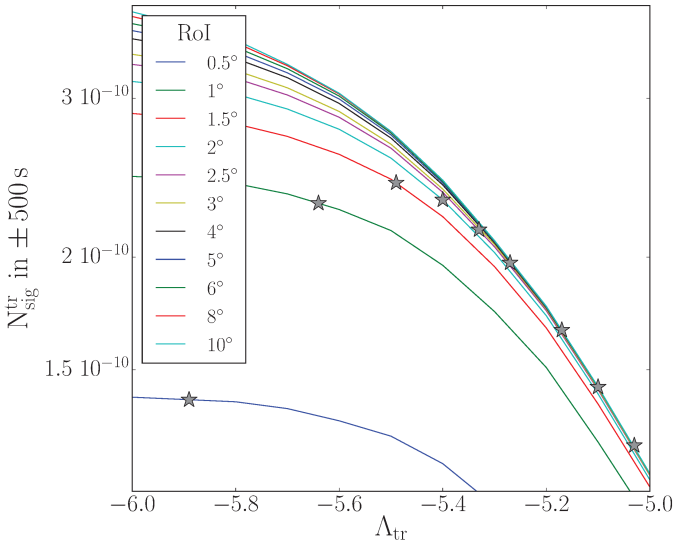

Figure 10.5 – Λ_{Tr} optimization. Number of signal events expected correlated in time for different sizes of the region of interest as a function of the cut on Λ_{Tr}.

Table 10.3 – List of the selection cuts applied for tracks. The usual cuts are defined in section 5.3.1. R_{RoI} is the angular distance of the event to the source and $|t_{\text{evt}} - t_{\text{src}}|$ the time between the merger and the neutrino candidate.

Criterion	Condition
Triggered	T3 or 3N
Downward-going	$\cos(\theta) > 0$
Quality	$\Lambda_{\text{Tr}} >$ -5.5
Error Estimate	$\beta_{\text{Tr}} < 1°$
Time correlation	$\lvert t_{\text{evt}} - t_{\text{src}} \rvert < 500\,\text{s}$
Spatial correlation	$R_{\text{RoI}} < 1.5°$

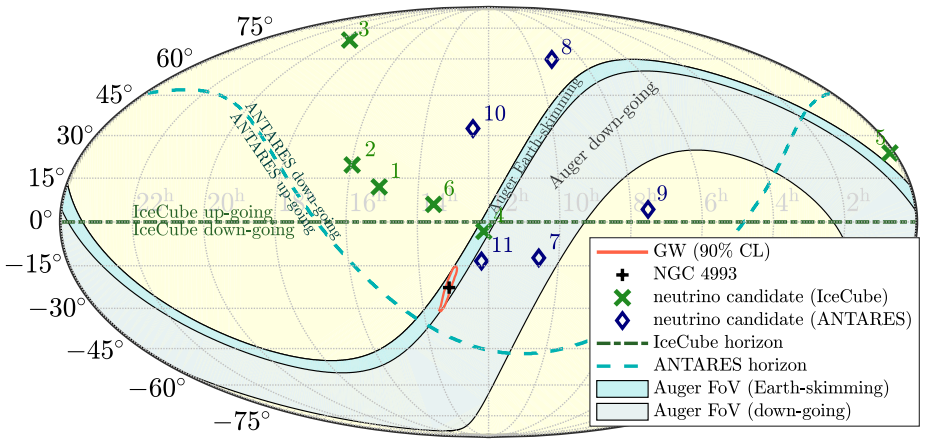

Figure 10.6 – Map of the neutrino follow-up of the GW170817 event. Localization of the 90 % credible region of GW170817 (red contour) and the NGC 4993 galaxy hosting the merger (black plus symbol) as well as the directions of ANTARES's (blue diamond) and IceCube's (green crosses) neutrino candidates within 500 s of the merger. ANTARES and IceCube's horizons separating downward-going and upward-going events (dashed blue and green lines respectively) are also shown with the Auger's fields of view of Earth-skimming (darker blue) and downward-going (lighter blue) directions. [147]

figure 10.6. A limit combining tracks and showers has been put on the neutrino flux expected from the merger, it is described in the chapter 11.

10.2.3 Shower plus Track: Long Time-scale Emission Search

This second analysis combining tracks and showers aims at testing a potential neutrino emission on a longer time-scale as presented in section 8.2, a time window of 14 days after the event is used.

Because of the wide time window, a significance of 3σ cannot be reached without removing a large part of the potential signal, therefore the usual upward-going point source cuts were applied with a region of interest defined as containing 90 % of the signal and no further optimisation has been performed. The radius R_{RoI} of this region is 1.5° for a median angular resolutions of 0.4° for the tracks. For the showers, R_{RoI} is of 12° and the median angular resolution is 3°.

During the 14 days time window, the binary neutron star has been inside of the ANTARES field of view ~7 days. The probability to have a background event in the time window is of ~10^{-2}.

As for the previous analyses, no events were seen and a limit has been derived as detailed in chapter 11.

10.3 IceCube Follow-up

The IceCube search for a neutrino counterpart to GW170817 started by an online analysis looking for a prompt neutrino emission in the ± 500 s time window. The online sample containing upward and downward-going tracks has been used like in previous online analyses [148, 149].

In this time window, 4.0 events are expected in the Northern sky and 2.7 in the Southern sky. Finally, as can be seen in figure 10.6, three events fall in the Northern sky and two in the Southern sky, which is compatible with the background expectation. None of them is spatially consistent with the merger. Afterwards, this analysis has also been applied on a longer time-window of 14 days, no correlation has been seen either.

In a second stage, an offline analysis has been performed within IceCube using contained tracks and showers as described in [147] leading to an event rate much lower than the online analysis. This analysis has been performed with two time windows, looking for a prompt emission within ± 500 s (see figure 10.6) and a longer time-scale emission within 14 days. A total of 0.4 tracks and 2.5 showers was expected to fall in the declination range [-13°, -33°] centred on GW170817, within 14 days.

Finally, no spatially correlated events were seen in any of the time windows. A limit combining the online and offline samples has been put as shown in chapter 11.

IceCube also proceeded to a search for an outburst of MeV neutrinos via an increase of the hit rate in the whole detector, no such increase has been measured.

10.4 Auger Follow-up

The Pierre Auger Collaboration performed two offline analyses with the same ± 500 s and + 14 days time windows as Antares and IceCube in order to publish together.

Luckily, the neutron star merger fell inside of the most sensitive field of view of the experiment, seeing the Earth-skimming events at the time of the coalescence as can be seen in figure 10.6. The probability of finding an event in this field of view and time window was computed to be of $6.3 \cdot 10^{-7}$ in the ± 500 s time window.

For the + 14 days time window, the position of the merger was in the Earth-skimming zone ~4 % of the time and in the downward-going zone ~11 % of the time, the downward-going zone being larger as can be seen of figure 10.6.

In these two analyses, no events were seen and limits at higher energies than Antares and IceCube have been put on the expected neutrino flux.

10.5 Summary

The four Antares follow-up analyses of the GW170817 event are summarized in Table 10.4 as well as the IceCube and Auger analyses mentioned earlier. No events has been seen coincident in time and space with the neutron star merger, this allows to put limits on the neutrino flux as explained in the following chapter.

Table 10.4 – Summary of the neutrino follow-up analyses of the GW170817 event. It follows the same order as the current chapter. The *release time* indicates the elapsed time between the event and the publication of the results.

Experiment	Online/ Offline	Field of View	Topology	Time Window
ANTARES	Online	Up	Track	± 500 s, ± 1 hr
ANTARES	Offline	Down	Track	± 500 s, ± 1 hr
ANTARES	Offline	Down	Track + Shower	± 500 s
ANTARES	Offline	Up	Track + Shower	+ 14 days
ICECUBE	Online	Full sky	Track	± 500 s, + 14 d
ICECUBE	Offline	Full sky	Contained Tr + Sh	± 500 s, + 14 d
ICECUBE	Offline	Full sky	MeV Neutrinos	± 500 s
Auger	Offline	Earth-skm	Air Shower	± 500 s
Auger	Offline	Down	Air Shower	+ 14 days

Chapter 11

Results

As explained in the previous chapter, after unblinding no neutrino event has been detected in space correlation with the GW170817 gravitational wave event in the online analyses.

This chapter focuses on the upper limits put on the neutrino fluence from the offline analyses in which no event have been seen in correlation in the ± 500 s time-window as shown in figure 10.6, neither in the + 14 days one.

11.1 Limit Computation

These null results are used to compute the upper limits at 90 % confidence level for both the ± 500 s and + 14 days analyses and for each experiment independently.

We know that a signal flux Φ will produce an average of N_{evts} detected signal events in the ANTARES detector with

$$N_{\text{evts}} = \iint \Phi(E,t)\, A_{\text{eff}}(E,\delta)\, dE\, dt, \tag{11.1}$$

A_{eff} being the effective area of the ANTARES detector which depends on the energy of the signal E, the declination of the source δ and the applied cuts.

Our analyses are integrated over time to be independent from the time evolution of the signal. As a consequence, the limits are put on the spectral fluence F which is the flux integrated over the time window considered in each analysis. The limits are given assuming an E^{-2} spectrum within each energy decade, therefore $\Phi(E) = \phi_0\, E^{-2}$ with ϕ_0 the normalisation of the flux. Hence F is given by

$$F = \int \Phi(E)\, dt = \Delta t\, \phi_0\, E^{-2}. \tag{11.2}$$

For an energy decade we obtain

$$N_{\text{evts}} = \Delta t\, \phi_0 \int_{E_{\text{low}}}^{E_{\text{up}}} E^{-2} A_{\text{eff}}(E,\delta)\, dE \tag{11.3}$$

$$= F E^2 \int_{E_{\text{low}}}^{E_{\text{up}}} E^{-2} A_{\text{eff}}(E,\delta)\, dE \tag{11.4}$$

with E_{low} and E_{up} the bounds of the decade.

But the number of events actually detected from a fluence F suffers Poissonian fluctuations. In Poisson statistics, the 90 % confidence level upper limit assuming a non detection is for an average number of events of $N_{\text{evts}}^{90\%} = 2.3$. In other words it is the average number of events for which we have less than 10 % chance to detect zero events. So the upper limit on the fluence with a 90 % confidence level is given by

$$E^2 F^{90\%} = \frac{2.3}{\int_{E_{\text{low}}}^{E_{\text{up}}} E^{-2} A_{\text{eff}}(E, \delta)\, dE}. \tag{11.5}$$

11.2 Results

The limits obtained are shown in figure 11.1 together with the signal expectations according to the models presented in section 8.2. In this figure, the fluences of the models have been rescaled to show the flux expected for a source at 40 Mpc which is the approximate measured distance of the merger. For the extended emission we also computed the approximated off-axis spectral fluences

$$F_{\text{off}}(E) = \eta\, F_{\text{on}}(E/\eta), \tag{11.6}$$

with $\eta = \delta(\theta_{\text{obs}})/\delta(0)$ the scaling factor accounting for the difference in the Lorentz boosts between the off-axis and on-axis viewing angles. This results in a difference in the Doppler factors δ between the two viewing angles, with $\delta(\theta_{\text{obs}}) = \left(\Gamma\, \left[1 - \beta \cos(\theta_{\text{obs}} - \theta_j)\right]\right)^{-1}$, θ_{obs} being the viewing angle and θ_j the opening angle of the jet. The parameter F_{on} is the on-axis fluence as given in [114].

As can be seen in the top panel of figure 11.1 which is related to the ± 500 s analysis, the extended emission is the most favorable for neutrino detection. The non-detection of any neutrino counterpart with IceCube is consistent with an off-axis viewing angle. This is compatible with the favoured hypothesis of an off-axis viewing angle. In comparison, relying on this model, the prompt emission is far from being detected, even in the on-axis hypothesis.

On the bottom panel, we can see the late-emission related to a potential magnetar resulting from the coalescence tested with the 14 days time window. Two curves are shown, corresponding to the integrated emission from approximately 0.3 to 3 days and from 3 to 30 days. The curve corresponding to the fluence integrated over 14 days was not displayed in the [112] article but it should lie between these two curves.

The differences in the Antares limits between the top and bottom panels are due to the different samples and time-windows. The downward-going sample used for the ± 500 s analysis is less sensitive at low energy because of the atmospheric muon rejection. It is at high energy that the upward-going sample used for the + 14 days analysis is less sensitive because of the absorption of high-energy neutrinos by the Earth. The difference in Auger limits come from the fact that in the 14 days time window the source is most of the time outside of its field of view.

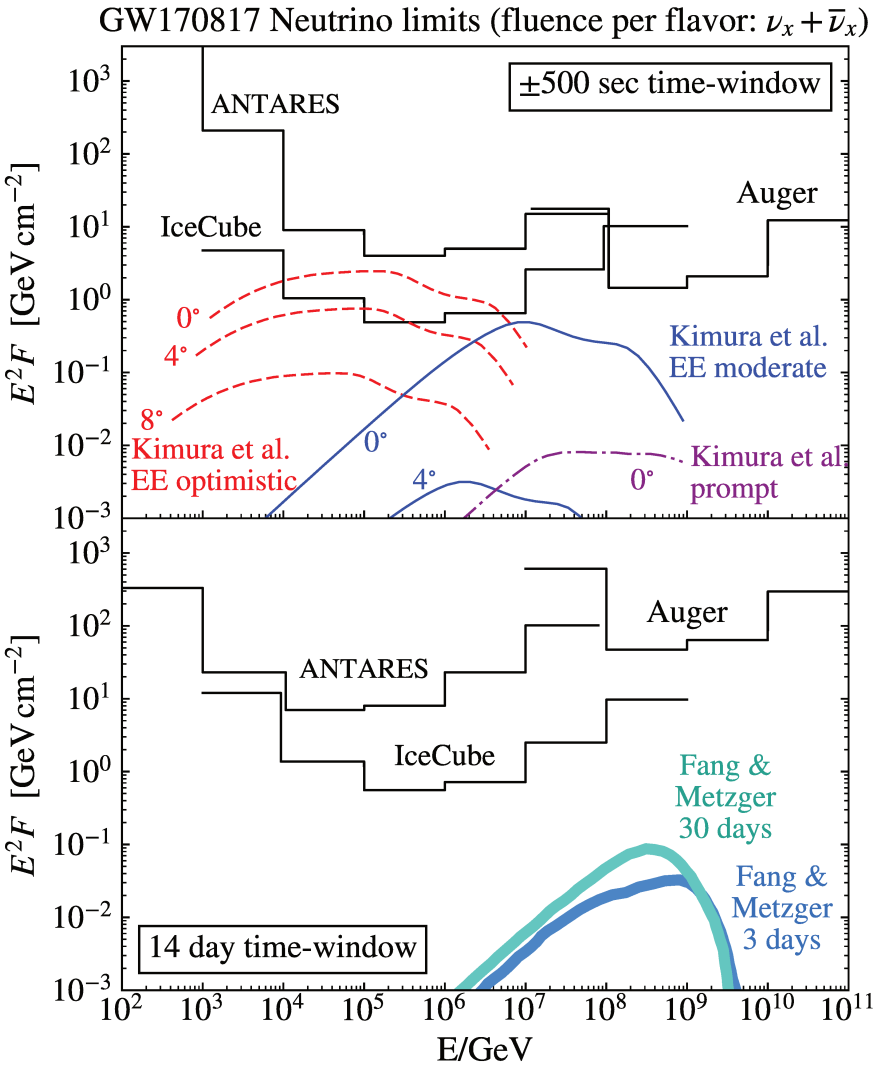

Figure 11.1 – Upper limits (at 90 % confidence level) on the neutrino spectral fluence from GW170817 during a ± 500 s window centred on the GW trigger time (top panel), and a 14-day window follow the GW trigger (bottom panel). Also shown are predictions by neutrino emission models scaled to a distance of 40 Mpc. In the upper plot, models from [114] for both extended emission (EE) and prompt emission are shown for the case of on-axis viewing angle and selected off-axis angles to indicate the dependence on this parameter. The shown off-axis angles are measured beyond the jet opening half angle. Models from [112] are shown in the lower plot. All fluences are shown as the per flavour sum of neutrino and anti-neutrino fluence. [147]

11.3 Conclusion

While resulting in a degraded sensitivity of both ANTARES and ICECUBE, the source location was ideal for the Pierre Auger Observatory. With a source located in the upward-going field of view of ANTARES or ICECUBE, we can expect a fluence sensitivity 5 to 10 times better for prompt emission with an E^{-2} neutrino spectrum depending on the energy range. Such a localization as well as a better orientation of the jet axis can be expected in the coming years thanks to the improvement of the gravitational wave detectors. Moreover, when aLIGO and aVirgo will reach their design sensitivities, KM3NeT will be taking data with a very good point source sensitivity.

A neutrino detection from early emissions will allow to characterise the proportion of hadronic and leptonic components inside of the jet and better understand the cosmic ray acceleration processes, it could also probe the presence of a cocoon or a structured jet and its dynamic. We can also detect neutrinos emitted from the inside of the central engine or more unexpected emissions. And late detections would probe the presence of a long-lived neutron star remnant in the form of a magnetar.

In parallel, a neutrino detection in the online analyses, may allow to localize the source earlier as explained in chapter 9.

Acknowledgements

I would like to thank my PhD advisors, Antoine Kouchner and Bruny Baret who trusted me and gave me the possibility to do fascinating studies. This work wouldn't have been possible without their help and their support.

I worked a lot with Bruny which was a real pleasure! I thank him for his advices that I came to get a little too often, and for the freedom he left me to follow them or not! Finally, I thank him for trusting me about the way I work, not always conventional, especially in the last few weeks of my PhD.

I also thank Alexis for his help in the follow-up of the event GW17081717, in my post-doc research and more generally whenever I needed him.

And I thank the three of them for their accurate review of this thesis.

I also thank all those who were part of the APC Antares/KM3NeT team during my thesis, as well as all the PhD students who participated in the warm atmosphere I experienced during this thesis. In alphabetical order I would like to thank Alexandre, Christine, Corinne, Dimitri, Jean-Baptiste, João, Luigi, Marc, Marion, Marta, Philippe, Rémy, Rodrigo, Salvatore, Si, Simon, Théodore, Véronique and many more… As well as the members of the Antares collaboration who helped me: Tino, Aart, Dorothea, Maurizio…

I also would like to thank my friends for the moments of recreation that I truly needed! Yann and Jonathan for the afternoons of games, Charles, Florian and Mathieu for… the afternoons of games and Clément, Élisa, Thessalie, Thomas and the others for the *evenings* of games! I also thank Alan, Alexandra, Baptiste, Jesse and Olivier for the rare but pleasant time spent together and Marie for the uncontrollable laughter attacks we had while she was in internship at APC.

Finally, I would like to thank my family for their support when I was not totally relaxed and not so pleasant during vacancies. In particular, I would like to thank my parents, thanks to which I was able to build myself and to build my rationalism that they did not always understand well. I have a special thought for my mother who left us just before I started my PhD, she was an ideal mother.

Bibliography

[1] C. L. Cowan et al. “Detection of the Free Neutrino: A Confirmation”. In: *Science* 124.3212 (July 20, 1956), pp. 103–104. DOI: 10.1126/science.124.3212.103 (cit. on p. 15).

[2] G. Danby et al. “Observation of High-Energy Neutrino Reactions and the Existence of Two Kinds of Neutrinos”. In: *Phys. Rev. Lett.* 9 (1962), pp. 36–44. DOI: 10.1103/PhysRevLett.9.36 (cit. on p. 15).

[3] K. Kodama et al. “Observation of Tau Neutrino Interactions”. In: *Phys. Lett. B* 504.3 (Apr. 2001), pp. 218–224. DOI: 10.1016/S0370-2693(01)00307-0 (cit. on p. 15).

[4] Y. Fukuda et al. “Measurement of the Flux and Zenith-Angle Distribution of Upward Throughgoing Muons by Super-Kamiokande”. In: *Phys. Rev. Lett.* 82.13 (Mar. 29, 1999), pp. 2644–2648. DOI: 10.1103/PhysRevLett.82.2644 (cit. on p. 15).

[5] V. F. Hess. “Penetrating Radiation in Seven Free Ballon Flights.” In: *Phys Zeitschr* 13 (1912), p. 1084 (cit. on p. 16).

[6] J. Clay. “Penetrating Radiation”. In: *Proceedings of the Royal Academy of Sciences Amsterdam*. Vol. 30. 1927, pp. 1115–1127 (cit. on p. 16).

[7] “Particle Data Group. 2015 Review of Particle Physics.” In: *Chin. Phys. C* 38 (2014 and 2015 update) (cit. on pp. 17, 29, 32).

[8] M. Takeda et al. “Extension of the Cosmic-Ray Energy Spectrum beyond the Predicted Greisen-Zatsepin-Kuz’min Cutoff”. In: *Phys. Rev. Lett.* 81.6 (Aug. 10, 1998), pp. 1163–1166. DOI: 10.1103/PhysRevLett.81.1163 (cit. on p. 17).

[9] R. U. Abbasi et al. “First Observation of the Greisen-Zatsepin-Kuzmin Suppression”. In: *Phys. Rev. Lett.* 100.10 (Mar. 10, 2008), p. 101101. DOI: 10.1103/PhysRevLett.100.101101 (cit. on p. 17).

[10] K. Greisen. “End to the Cosmic-Ray Spectrum?” In: *Phys. Rev. Lett.* 16.17 (Apr. 25, 1966), pp. 748–750. DOI: 10.1103/PhysRevLett.16.748 (cit. on p. 17).

[11] G. T. Zatsepin and V. A. Kuz’min. “Upper Limit of the Spectrum of Cosmic Rays”. In: *JETP Lett.* 4.3 (Aug. 1, 1966), p. 78 (cit. on p. 17).

[12] E. Fermi. “On the Origin of the Cosmic Radiation”. In: *Phys. Rev.* 75.8 (Apr. 15, 1949), pp. 1169–1174. DOI: 10.1103/PhysRev.75.1169 (cit. on p. 17).

[13] T. Michael. "Light at the End of the Shower An All-Flavour Neutrino Point-Source Search with the ANTARES Neutrino Telescope". PhD Thesis. 2016 (cit. on pp. 19, 30, 32, 33, 46, 47).

[14] V. L. Ginzburg, Y. M. Khazan, and V. S. Ptuskin. "Origin of Cosmic Rays: Galactic Models with Halo". In: *Astrophys. Space Sci.* 68.2 (Apr. 1, 1980), pp. 295–314. DOI: 10.1007/BF00639701 (cit. on p. 17).

[15] K. S. Hirata et al. "Observation in the Kamiokande-II Detector of the Neutrino Burst from Supernova SN1987A". In: *Phys. Rev. D* 38.2 (July 15, 1988), pp. 448–458. DOI: 10.1103/PhysRevD.38.448 (cit. on p. 20).

[16] T. Haines et al. "Neutrinos from SN1987a in the IMB Detector". In: *Nucl. Instrum. Methods Phys. Res. Sect. A* 264.1 (Feb. 1, 1988), pp. 28–31. DOI: 10.1016/0168-9002(88)91097-2 (cit. on p. 20).

[17] M. Aglietta et al. "On the Event Observed in the Mont Blanc Underground Neutrino Observatory during the Occurrence of Supernova 1987 *A*". In: *Europhys. Lett.* 3.12 (June 15, 1987), pp. 1315–1320. DOI: 10.1209/0295-5075/3/12/011 (cit. on p. 20).

[18] B. P. Abbott et al. "Observation of Gravitational Waves from a Binary Black Hole Merger". In: *Phys. Rev. Lett.* 116.6 (Feb. 11, 2016), p. 061102. DOI: 10.1103/PhysRevLett.116.061102 (cit. on pp. 20, 118, 122, 123).

[19] B. P. Abbott et al. "GW170817: Observation of Gravitational Waves from a Binary Neutron Star Inspiral". In: *Phys. Rev. Lett.* 119.16 (Oct. 16, 2017), p. 161101. DOI: 10.1103/PhysRevLett.119.161101 (cit. on pp. 21, 118, 124, 125, 127).

[20] A. Goldstein et al. "An Ordinary Short Gamma-Ray Burst with Extraordinary Implications: *Fermi*-GBM Detection of GRB 170817A". In: *Astrophys. J.* 848.2 (Oct. 16, 2017), p. L14. DOI: 10.3847/2041-8213/aa8f41 (cit. on pp. 21, 120, 123, 129, 133).

[21] B. P. Abbott et al. "Multi-Messenger Observations of a Binary Neutron Star Merger". In: *Astrophys. J.* 848.2 (Oct. 16, 2017), p. L12. DOI: 10.3847/2041-8213/aa91c9 (cit. on pp. 21, 120, 127).

[22] T. I. Collaboration et al. "Multimessenger Observations of a Flaring Blazar Coincident with High-Energy Neutrino IceCube-170922A". In: *Science* 361.6398 (July 13, 2018), eaat1378. DOI: 10.1126/science.aat1378 (cit. on pp. 21, 22).

[23] M. G. Aartsen et al. "Neutrino Emission from the Direction of the Blazar TXS 0506+056 Prior to the IceCube-170922A Alert". In: *Science* 361.6398 (July 12, 2018), pp. 147–151. DOI: 10.1126/science.aat2890 (cit. on p. 21).

[24] S. Gao et al. "Interpretation of the Coincident Observation of a High Energy Neutrino and a Bright Flare". In: *arXiv* (July 11, 2018). arXiv: 1807.04275 (cit. on p. 21).

[25] A. Albert et al. "Search for Neutrinos from TXS 0506+056 with the ANTARES Telescope". In: (July 11, 2018). arXiv: 1807.04309 [astro-ph] (cit. on pp. 21, 23).

[26] A. Neronov, D. V. Semikoz, and C. Tchernin. "PeV Neutrinos from Interactions of Cosmic Rays with the Interstellar Medium in the Galaxy". In: *Phys. Rev. D* 89.10 (May 5, 2014), p. 103002. DOI: 10.1103/PhysRevD.89.103002 (cit. on p. 23).

[27] A. Neronov and D. V. Semikoz. "Evidence the Galactic Contribution to the IceCube Astrophysical Neutrino Flux". In: *Astropart. Phys.* 75 (2016), pp. 60–63. DOI: 10.1016/j.astropartphys.2015.11.002 (cit. on pp. 23, 69, 106).

[28] S. V. Troitsky. "Search for the Galactic Disk and Halo Components in the Arrival Directions of High-Energy Astrophysical Neutrinos". In: *JETP Lett.* 102.12 (Dec. 1, 2015), pp. 785–788. DOI: 10.1134/S0021364015240133 (cit. on p. 23).

[29] A. Palladino and F. Vissani. "Extragalactic plus Galactic Model for IceCube Neutrino Events". In: *Astrophys. J.* 826.2 (July 29, 2016), p. 185. DOI: 10.3847/0004-637X/826/2/185 (cit. on p. 23).

[30] G. Pagliaroli, C. Evoli, and F. L. Villante. "Expectations for High Energy Diffuse Galactic Neutrinos for Different Cosmic Ray Distributions". In: *J. Cosmol. Astropart. Phys.* 2016.11 (Nov. 2, 2016), pp. 004–004. DOI: 10.1088/1475-7516/2016/11/004 (cit. on p. 23).

[31] M. G. Aartsen et al. "Evidence for Astrophysical Muon Neutrinos from the Northern Sky with IceCube". In: *Phys. Rev. Lett.* 115.8 (Aug. 20, 2015), p. 081102. DOI: 10.1103/PhysRevLett.115.081102 (cit. on p. 23).

[32] M. G. Aartsen et al. "Observation and Characterisation of a Cosmic Muon Neutrino Flux from the Northern Hemisphere Using Six Years of IceCube Data". In: *Astrophys. J.* 833.1 (Dec. 1, 2016), p. 3. DOI: 10.3847/0004-637X/833/1/3 (cit. on pp. 23, 24, 69, 106).

[33] H. M. Niederhausen, M. Lesiak-Bzdak, and A. Stoessl. "High Energy Astrophysical Neutrino Flux Characteristics for Neutrino-Induced Cascades Using IC79 and IC86-String IceCube Configurations". In: *Proceedings of The 34th International Cosmic Ray Conference — PoS(ICRC2015)*. The 34th International Cosmic Ray Conference. Vol. 236. SISSA Medialab, Aug. 18, 2016, p. 1109. DOI: 10.22323/1.236.1109 (cit. on p. 23).

[34] C. Kopper and on behalf of the IceCube Collaboration. "Observation of Astrophysical Neutrinos in Six Years of IceCube Data". In: *Proceedings of 35th International Cosmic Ray Conference — PoS(ICRC2017)*. 35th International Cosmic Ray Conference. Vol. 301. SISSA Medialab, Aug. 16, 2017, p. 981 (cit. on p. 23).

[35] M. G. Aartsen et al. "A Combined Maximum-Likelihood Analysis of the High-Energy Astrophysical Neutrino Flux Measured with IceCube". In: *Astrophys. J.* 809.1 (Aug. 13, 2015), p. 98. DOI: 10.1088/0004-637X/809/1/98. arXiv: 1507.03991 (cit. on pp. 23, 106).

[36] D. Gaggero et al. "The Gamma-Ray and Neutrino Sky: A Consistent Picture of Fermi-LAT, Milagro, and IceCube Results". In: *Astrophys. J.* 815.2 (2015), p. L25. DOI: 10.1088/2041-8205/815/2/L25 (cit. on pp. 25, 54, 61, 68–70).

[37] M. Ageron et al. "ANTARES: The First Undersea Neutrino Telescope". In: *Nucl. Instrum. Methods Phys. Res. Sect. A* A656 (2011), pp. 11–38. DOI: 10.1016/j.nima.2011.06.103 (cit. on pp. 27, 33).

[38] S. L. Glashow and S. Weinberg. "Natural Conservation Laws for Neutral Currents". In: *Phys. Rev. D* 15.7 (Apr. 1, 1977), pp. 1958–1965. DOI: 10.1103/PhysRevD.15.1958 (cit. on p. 28).

[39] M. A. Markov. “On High Energy Neutrino Physics”. In: 1960, pp. 578–581 (cit. on p. 29).

[40] E. Aslanides and others. “A Deep Sea Telescope for High Energy Neutrinos”. In: *ArXiv* (July 29, 1999). arXiv: astro-ph/9907432 (cit. on p. 29).

[41] S. L. Glashow. “Resonant Scattering of Antineutrinos”. In: *Phys. Rev. Lett.* 118 (1960), pp. 316–317. DOI: 10.1103/PhysRev.118.316 (cit. on p. 31).

[42] J. V. Jelley. *Cerenkov Radiation And Its Applications*. In collab. with Osmania University and Digital Library Of India. Pergamon Press, 1958/00/00. 331 pp. (cit. on p. 31).

[43] R. Gandhi et al. “Neutrino Interactions at Ultrahigh Energies”. In: *Phys. Rev. D* 58.9 (Sept. 30, 1998), p. 093009. DOI: 10.1103/PhysRevD.58.093009 (cit. on p. 33).

[44] R. Gracia-Ruiz. “Search for Populations of Unresolved Sources of High Energy Neutrinos with the ANTARES Neutrino Telescope.” (cit. on pp. 34, 46).

[45] J. A. Aguilar et al. “AMADEUS - The Acoustic Neutrino Detection Test System of the ANTARES Deep-Sea Neutrino Telescope”. In: *Nucl. Instrum. Methods Phys. Res. Sect. A* 626-627 (Jan. 2011), pp. 128–143. DOI: 10.1016/j.nima.2010.09.053. arXiv: 1009.4179 (cit. on p. 35).

[46] J. A. Aguilar et al. “The Data Acquisition System for the ANTARES Neutrino Telescope”. In: *Nucl. Instrum. Methods Phys. Res. Sect. A* 570.1 (Jan. 1, 2007), pp. 107–116. DOI: 10.1016/j.nima.2006.09.098 (cit. on pp. 37, 139).

[47] J. Aguilar et al. “Performance of the Front-End Electronics of the ANTARES Neutrino Telescope”. In: *Nucl. Instrum. Methods Phys. Res. Sect. Accel. Spectrometers Detect. Assoc. Equip.* 622.1 (Oct. 2010), pp. 59–73. DOI: 10.1016/j.nima.2010.06.225 (cit. on p. 37).

[48] J. A. Aguilar et al. “Time Calibration of the ANTARES Neutrino Telescope”. In: *Astropart. Phys.* 34.7 (Feb. 2011), pp. 539–549. DOI: 10.1016/j.astropartphys.2010.12.004. arXiv: 1012.2204 (cit. on pp. 39, 139).

[49] S Adrián-Martínez et al. “The Positioning System of the ANTARES Neutrino Telescope”. In: *J. Instrum.* 7.08 (Aug. 14, 2012), T08002–T08002. DOI: 10.1088/1748-0221/7/08/T08002 (cit. on pp. 40, 139).

[50] A. Kouchner. *ANTARES: Etalonnage de l’électronique Frontale, Étude de Muons Atmospheriques et Recherche de Neutrinos Cosmiques*. Jan. 14, 2010 (cit. on p. 41).

[51] L. A. Fusco and A. Margiotta. “The Run-by-Run Monte Carlo Simulation for the ANTARES Experiment”. In: *EPJ Web of Conferences*. Vol. 116. Apr. 11, 2016, p. 02002. DOI: 10.1051/epjconf/201611602002 (cit. on p. 41).

[52] D. Bailey. “Monte Carlo Tools and Analysis Methods for Understanding the ANTARES Experiment and Predicting Its Sensitivity to Dark Matter”. In: (2002) (cit. on p. 42).

[53] R. Gandhi et al. “Ultrahigh-Energy Neutrino Interactions”. In: *Astropart. Phys.* 5.2 (Aug. 1996), pp. 81–110. DOI: 10.1016/0927-6505(96)00008-4. arXiv: hep-ph/9512364 (cit. on p. 42).

[54] G. Carminati et al. “Atmospheric MUons from PArametric Formulas: A Fast GEnerator for Neutrino Telescopes (MUPAGE)”. In: *Comput. Phys. Commun.* 179.12 (Dec. 15, 2008), pp. 915–923. DOI: 10.1016/j.cpc.2008.07.014 (cit. on p. 44).

[55] S. Agostinelli et al. “Geant4—a Simulation Toolkit”. In: *Nucl. Instrum. Methods Phys. Res. Sect. A* 506.3 (July 1, 2003), pp. 250–303. DOI: 10.1016/S0168-9002(03)01368-8 (cit. on p. 44).

[56] A. Heijboer. “Track Reconstruction and Point Source Searches with ANTARES”. PhD Thesis. 2004 (cit. on p. 45).

[57] G. Cowan. *Statistical Data Analysis*. 1 edition. Oxford : New York: Clarendon Press, June 4, 1998. 216 pp. (cit. on p. 47).

[58] V. M. Aynutdinov and Z.-A. M. Dzhilkibaev. “The Baikal Neutrino Project”. In: *Neutrino Astronomy*. World Scientific, Dec. 23, 2015, pp. 115–124. DOI: 10.1142/9789814759410_0008 (cit. on p. 49).

[59] F. Halzen and S. R. Klein. “IceCube: An Instrument for Neutrino Astronomy”. In: *Phys. Today* 61.5 (May 2008), pp. 29–35. DOI: 10.1063/1.2930733 (cit. on p. 49).

[60] I. Collaboration et al. “Cosmic Ray Composition and Energy Spectrum from 1-30 PeV Using the 40-String Configuration of IceTop and IceCube”. In: *Astropart. Phys.* 42 (Feb. 2013), pp. 15–32. DOI: 10.1016/j.astropartphys.2012.11.003. arXiv: 1207.3455 (cit. on p. 49).

[61] J. Abraham et al. “Properties and Performance of the Prototype Instrument for the Pierre Auger Observatory”. In: *Nuclear Instruments and Methods in Physics Research Section A: Accelerators, Spectrometers, Detectors and Associated Equipment* 523.1 (May 1, 2004), pp. 50–95. DOI: 10.1016/j.nima.2003.12.012 (cit. on p. 51).

[62] A. Aab et al. “Improved Limit to the Diffuse Flux of Ultrahigh Energy Neutrinos from the Pierre Auger Observatory”. In: *Phys.Rev.* D91.9 (May 26, 2015), p. 092008. DOI: 10.1103/PhysRevD.91.092008 (cit. on p. 52).

[63] S. Adrián-Martínez et al. “Letter of Intent for KM3NeT 2.0”. In: *J. Phys. G Nucl. Part. Phys.* 43.8 (2016), p. 084001. DOI: 10.1088/0954-3899/43/8/084001 (cit. on p. 53).

[64] R. Coniglione et al. “The KM3NeT/ARCA Detection Capability to a Diffuse Flux of Cosmic Neutrinos”. In: *Proceedings of 35th International Cosmic Ray Conference — PoS(ICRC2017)*. 35th International Cosmic Ray Conference. Vol. 301. SISSA Medialab, Aug. 16, 2017, p. 998 (cit. on p. 54).

[65] A. Trovato et al. “Expectations for Detection of Neutrinos from Point-like Sources with KM3NeT/ARCA”. In: *Proceedings of 35th International Cosmic Ray Conference — PoS(ICRC2017)*. 35th International Cosmic Ray Conference. Vol. 301. SISSA Medialab, Aug. 16, 2017, p. 999 (cit. on pp. 54, 56, 57).

[66] D. Gaggero et al. “Gamma-Ray Sky Points to Radial Gradients in Cosmic-Ray Transport”. In: *Phys. Rev. D* 91.8 (2015), p. 083012. DOI: 10.1103/PhysRevD.91.083012 (cit. on pp. 61, 67).

[67] E. P. Hubble. "Extragalactic Nebulae." In: *Astrophys. J.* 64 (Dec. 1, 1926), pp. 321–369. DOI: 10.1086/143018 (cit. on p. 61).

[68] M. H. Jones, R. J. A. Lambourne, and S. Serjeant, eds. *An Introduction to Galaxies and Cosmology*. Revised edition. Cambridge: Cambridge - Open University, Feb. 9, 2015. 450 pp. (cit. on p. 61).

[69] L. A. Fusco. "Search for a Diffuse Neutrino Emission in the Southern Sky with the Antares Telescope". PhD Thesis. 2016 (cit. on p. 62).

[70] R. Pogge. *Physics of The Interstellar Medium*. 2011. URL: http://www.astronomy.ohio-state.edu/~pogge/Ast871/ (visited on 07/30/2018) (cit. on p. 64).

[71] R. Jansson and G. R. Farrar. "A New Model of the Galactic Magnetic Field". In: *Astrophys. J.* 757 (2012), p. 14. DOI: 10.1088/0004-637X/757/1/14 (cit. on p. 64).

[72] V. L. Ginzburg and S. I. Syrovatskii. *The Origin of Cosmic Rays*. Elsevier, 1964. DOI: 10.1016/C2013-0-05547-8 (cit. on p. 65).

[73] M. Ackermann et al. "Fermi-LAT Observations of the Diffuse γ-Ray Emission: Implications for Cosmic Rays and the Interstellar Medium". In: *Astrophys. J.* 750.1 (2012), p. 3. DOI: 10.1088/0004-637X/750/1/3 (cit. on p. 66).

[74] E. G. Berezhko and H. J. Voelk. "The Contribution of Different Supernova Populations to the Galactic Gamma-Ray Background". In: *Astrophys. J.* 611.1 (Aug. 10, 2004), pp. 12–19. DOI: 10.1086/421937. arXiv: astro-ph/0404307 (cit. on p. 66).

[75] A. D. Erlykin and A. W. Wolfendale. "Cosmic Rays in the Inner Galaxy and the Diffusion Properties of the Interstellar Medium". In: *Astropart. Phys.* 42 (Feb. 1, 2013), pp. 70–75. DOI: 10.1016/j.astropartphys.2012.12.003 (cit. on p. 66).

[76] W. de Boer and M. Weber. "Fermi Bubbles and Bubble-like Emission from the Galactic Plane". In: *Astrophys. J.* 794.1 (Sept. 30, 2014), p. L17. DOI: 10.1088/2041-8205/794/1/L17. arXiv: 1407.4114 (cit. on p. 66).

[77] A. W. Strong and I. V. Moskalenko. "Propagation of Cosmic-Ray Nucleons in the Galaxy". In: *ApJ* 509.1 (1998), p. 212. DOI: 10.1086/306470 (cit. on p. 66).

[78] C. Evoli et al. "Antiprotons from Dark Matter Annihilation in the Galaxy: Astrophysical Uncertainties". In: *Phys. Rev. D* 85.12 (June 7, 2012), p. 123511. DOI: 10.1103/PhysRevD.85.123511. arXiv: 1108.0664 (cit. on pp. 67, 70).

[79] S. L. Snowden et al. "ROSAT Survey Diffuse X-Ray Background Maps. II." In: *Astrophys. J.* 485 (1997), p. 125. DOI: 10.1086/304399 (cit. on p. 67).

[80] H. S. Ahn et al. "Discrepant Hardening Observed in Cosmic-Ray Elemental Spectra". In: *Astrophys. J.* 714.1 (May 1, 2010), pp. L89–L93. DOI: 10.1088/2041-8205/714/1/L89. arXiv: 1004.1123 (cit. on p. 67).

[81] T. Antoni et al. "KASCADE Measurements of Energy Spectra for Elemental Groups of Cosmic Rays: Results and Open Problems". In: *Astropart. Phys.* 24.1-2 (Sept. 2005), pp. 1–25. DOI: 10.1016/j.astropartphys.2005.04.001. arXiv: astro-ph/0505413 (cit. on p. 67).

[82] W. D. Apel et al. "KASCADE-Grande Measurements of Energy Spectra for Elemental Groups of Cosmic Rays". In: *Astropart. Phys.* 47 (July 2013), pp. 54–66. DOI: 10.1016/j.astropartphys.2013.06.004. arXiv: 1306.6283 (cit. on p. 67).

[83] V. Vitale, A. Morselli, and the Fermi/LAT Collaboration. "Indirect Search for Dark Matter from the Center of the Milky Way with the Fermi-Large Area Telescope". In: *ArXiv* (Dec. 20, 2009). arXiv: 0912.3828 (cit. on p. 68).

[84] L. Goodenough and D. Hooper. "Possible Evidence For Dark Matter Annihilation In The Inner Milky Way From The Fermi Gamma Ray Space Telescope". In: *ArXiv* (Oct. 15, 2009). arXiv: 0910.2998 (cit. on p. 68).

[85] T. Daylan et al. "The Characterization of the Gamma-Ray Signal from the Central Milky Way: A Compelling Case for Annihilating Dark Matter". In: *Phys. Dark Universe* 12 (June 2016), pp. 1–23. DOI: 10.1016/j.dark.2015.12.005. arXiv: 1402.6703 (cit. on p. 68).

[86] D. Gaggero et al. "Hard Cosmic Ray Sea in the Galactic Center: A Consistent Interpretation of H.E.S.S. and Fermi-LAT γ-Ray Data". In: *Proceedings of 35th International Cosmic Ray Conference — PoS(ICRC2017)*. 35th International Cosmic Ray Conference. Vol. 301. SISSA Medialab, July 26, 2017, p. 739. arXiv: 1707.08473 (cit. on p. 68).

[87] H. Abdalla et al. "Characterising the VHE Diffuse Emission in the Central 200 Parsecs of Our Galaxy with H.E.S.S". In: *Astron. Astrophys.* 612 (Apr. 2018), A9. DOI: 10.1051/0004-6361/201730824. arXiv: 1706.04535 (cit. on p. 68).

[88] D. Grasso et al. "Evidences of Unconventional Cosmic Ray Propagation in Gamma-Ray and Neutrino Astronomy". In: Sissa Medialab, Mar. 5, 2017, p. 055. DOI: 10.22323/1.283.0055 (cit. on p. 68).

[89] T. Kamae et al. "Parameterization of Gamma, e-/+ and Neutrino Spectra Produced by p-p Interaction in Astronomical Environment". In: *Astrophys. J.* 647 (2006), pp. 692–708. DOI: 10.1086/513602 (cit. on p. 69).

[90] S. R. Kelner, F. A. Aharonian, and V. V. Bugayov. "Energy Spectra of Gamma-Rays, Electrons and Neutrinos Produced at Proton-Proton Interactions in the Very High Energy Regime". In: *Phys. Rev. D* 74 (2006), p. 034018. DOI: 10.1103/PhysRevD.74.034018 (cit. on p. 69).

[91] A. Palladino, M. Spurio, and F. Vissani. "On the IceCube Spectral Anomaly". In: *J. Cosmol. Astropart. Phys.* 2016.12 (Dec. 28, 2016), pp. 045–045. DOI: 10.1088/1475-7516/2016/12/045. arXiv: 1610.07015 (cit. on pp. 69, 106).

[92] S. Adrián-Martínez et al. "Constraints on the Neutrino Emission from the Galactic Ridge with the ANTARES Telescope". In: *Phys. Lett. B* 760 (Sept. 2016), pp. 143–148. DOI: 10.1016/j.physletb.2016.06.051 (cit. on pp. 69, 70).

[93] M. Spurio. "Constraints to a Galactic Component of the IceCube Cosmic Neutrino Flux from ANTARES". In: *Phys. Rev. D* 90.10 (Nov. 11, 2014), p. 103004. DOI: 10.1103/PhysRevD.90.103004 (cit. on p. 70).

[94] A. Albert et al. “First All-Flavour Neutrino Point-like Source Search with the ANTARES Neutrino Telescope”. In: *Phys. Rev. D* 96.8 (Oct. 3, 2017), p. 082001. DOI: 10.1103/PhysRevD.96.082001. arXiv: 1706.01857 (cit. on pp. 74, 76, 140).

[95] F. Folger. “Search for a Diffuse Cosmic Neutrino Flux Using Shower Events in the ANTARES Neutrino Telescope”. PhD Thesis (cit. on p. 77).

[96] A. Albert et al. “An Algorithm for the Reconstruction of Neutrino-Induced Showers in the ANTARES Neutrino Telescope”. In: *Astron. J.* 154.6 (Aug. 11, 2017), p. 275. DOI: 10.3847/1538-3881/aa9709 (cit. on p. 77).

[97] M. G. Aartsen et al. “Constraints on Galactic Neutrino Emission with Seven Years of IceCube Data”. In: *Astrophys. J.* 849.1 (Oct. 31, 2017), p. 67. DOI: 10.3847/1538-4357/aa8dfb. arXiv: 1707.03416 (cit. on pp. 83, 105).

[98] F. James and M. Roos. “Minuit - A System for Function Minimization and Analysis of the Parameter Errors and Correlations”. In: *Comput. Phys. Commun.* 10.6 (Dec. 1975), pp. 343–367. DOI: 10.1016/0010-4655(75)90039-9 (cit. on p. 87).

[99] S. Adrián-Martínez et al. “Search for Cosmic Neutrino Point Sources with Four Years of Data from the ANTARES Telescope”. In: *Astrophys. J.* 760.1 (Nov. 20, 2012), p. 53. DOI: 10.1088/0004-637X/760/1/53. arXiv: 1207.3105 (cit. on pp. 90, 140).

[100] S. Adrián-Martínez et al. “The First Combined Search for Neutrino Point-Sources in the Southern Hemisphere with the ANTARES and IceCube Neutrino Telescopes”. In: *Astrophys. J.* 823.1 (May 23, 2016), p. 65. DOI: 10.3847/0004-637X/823/1/65 (cit. on p. 105).

[101] M. G. Aartsen et al. “All-Sky Search for Time-Integrated Neutrino Emission from Astrophysical Sources with 7 Years of IceCube Data”. In: *Astrophys. J.* 835.2 (Jan. 24, 2017), p. 151. DOI: 10.3847/1538-4357/835/2/151. arXiv: 1609.04981 (cit. on p. 105).

[102] A. Albert et al. “New Constraints on All Flavour Galactic Diffuse Neutrino Emission with the ANTARES Telescope”. In: *Phys. Rev. D* 96.6 (Sept. 11, 2017), p. 062001. DOI: 10.1103/PhysRevD.96.062001. arXiv: 1705.00497 (cit. on pp. 105, 106).

[103] M. Chianese, G. Miele, and S. Morisi. “Interpreting IceCube 6-Year HESE Data as an Evidence for Hundred TeV Decaying Dark Matter”. In: *Phys. Lett. B* 773 (Oct. 2017), pp. 591–595. DOI: 10.1016/j.physletb.2017.09.016 (cit. on p. 106).

[104] J. Chadwick. “Possible Existence of a Neutron”. In: *Nature* 129.3252 (Feb. 1932), p. 312. DOI: 10.1038/129312a0 (cit. on p. 111).

[105] W. Baade and F. Zwicky. “Remarks on Super-Novae and Cosmic Rays”. In: *Phys. Rev.* 46.1 (July 1, 1934), pp. 76–77. DOI: 10.1103/PhysRev.46.76.2 (cit. on p. 111).

[106] A. Hewish et al. “Observation of a Rapidly Pulsating Radio Source”. In: *Nature* 217.5130 (Feb. 1968), pp. 709–713. DOI: 10.1038/217709a0 (cit. on p. 111).

[107] H.-T. Janka. “Explosion Mechanisms of Core-Collapse Supernovae”. In: *Annu. Rev. Nucl. Part. Sci.* 62.1 (Nov. 23, 2012), pp. 407–451. DOI: 10.1146/annurev-nucl-102711-094901. arXiv: 1206.2503 (cit. on p. 111).

[108] N. Chamel and P. Haensel. "Physics of Neutron Star Crusts". In: *Living Rev. Relativ.* 11.1 (Dec. 2008). DOI: 10.12942/lrr-2008-10 (cit. on p. 111).

[109] S. F. P. Zwart and L. R. Yungelson. "Formation and Evolution of Binary Neutron Stars". In: *ArXiv* (Oct. 30, 1997). arXiv: astro-ph/9710347 (cit. on p. 113).

[110] R. C. Tolman. "Static Solutions of Einstein's Field Equations for Spheres of Fluid". In: *Phys. Rev.* 55.4 (Feb. 15, 1939), pp. 364–373. DOI: 10.1103/PhysRev.55.364 (cit. on p. 113).

[111] J. R. Oppenheimer and G. M. Volkoff. "On Massive Neutron Cores". In: *Phys. Rev.* 55.4 (Feb. 15, 1939), pp. 374–381. DOI: 10.1103/PhysRev.55.374 (cit. on p. 113).

[112] K. Fang and B. D. Metzger. "High-Energy Neutrinos from Millisecond Magnetars Formed from the Merger of Binary Neutron Stars". In: *Astrophys. J.* 849.2 (2017), p. 153. DOI: 10.3847/1538-4357/aa8b6a (cit. on pp. 113, 114, 117, 148, 149).

[113] I. Bartos, P. Brady, and S. Márka. "How Gravitational-Wave Observations Can Shape the Gamma-Ray Burst Paradigm". In: *Class. Quantum Gravity* 30.12 (June 21, 2013), p. 123001. DOI: 10.1088/0264-9381/30/12/123001. arXiv: 1212.2289 (cit. on p. 113).

[114] S. S. Kimura et al. "High-Energy Neutrino Emission from Short Gamma-Ray Bursts: Prospects for Coincident Detection with Gravitational Waves". In: *Astrophys. J. Lett.* 848.1 (2017), p. L4 (cit. on pp. 113, 114, 116, 148, 149).

[115] M. Ruiz et al. "Binary Neutron Star Mergers: A Jet Engine for Short Gamma-Ray Bursts". In: *Astrophys. J.* 824.1 (June 3, 2016), p. L6. DOI: 10.3847/2041-8205/824/1/L6. arXiv: 1604.02455 (cit. on pp. 113, 115).

[116] D. Guetta et al. "Neutrinos From Individual Gamma-Ray Bursts in the BATSE Catalog". In: *Astropart. Phys.* 20.4 (Jan. 2004), pp. 429–455. DOI: 10.1016/S0927-6505(03)00211-1. arXiv: astro-ph/0302524 (cit. on p. 114).

[117] B. Baret et al. "Bounding the Time Delay between High-Energy Neutrinos and Gravitational-Wave Transients from Gamma-Ray Bursts". In: *Astropart. Phys.* 35.1 (Aug. 2011), pp. 1–7. DOI: 10.1016/j.astropartphys.2011.04.001. arXiv: 1101.4669 (cit. on p. 114).

[118] A. Einstein. "On the General Theory of Relativity". In: *Akad. Wiss. Berlin Math. Phys.* 1915 (1915), pp. 778–786 (cit. on p. 118).

[119] Thingiverse.com. *Gravitational Waves - The First 6 Detections by Sfactor.* URL: https://www.thingiverse.com/make:491710 (visited on 07/01/2018) (cit. on p. 119).

[120] A. A. Michelson and E. W. Morley. "On the Relative Motion of the Earth and the Luminiferous Ether". In: *Am. J. Sci.* Series 3 Vol. 34.203 (Jan. 11, 1887), pp. 333–345. DOI: 10.2475/ajs.s3-34.203.333 (cit. on p. 120).

[121] B. Abbott et al. "Detector Description and Performance for the First Coincidence Observations between LIGO and GEO". In: *Nucl. Instrum. Methods Phys. Res. Sect. A* 517.1-3 (Jan. 2004), pp. 154–179. DOI: 10.1016/j.nima.2003.11.124 (cit. on p. 120).

[122] A. Giazotto. "The Virgo Project: A Wide Band Antenna for Gravitational Wave Detection". In: *Nucl. Instrum. Methods Phys. Res. Sect. A* A289 (1990), pp. 518–525. DOI: 10.1016/0168-9002(90)91525-G (cit. on p. 120).

[123] B. P. Abbott et al. "GW151226: Observation of Gravitational Waves from a 22-Solar-Mass Binary Black Hole Coalescence". In: *Phys. Rev. Lett.* 116.24 (June 15, 2016), p. 241103. DOI: 10.1103/PhysRevLett.116.241103 (cit. on p. 123).

[124] B. P. Abbott et al. "GW170104: Observation of a 50-Solar-Mass Binary Black Hole Coalescence at Redshift 0.2". In: *Phys. Rev. Lett.* 118.22 (June 1, 2017), p. 221101. DOI: 10.1103/PhysRevLett.118.221101 (cit. on pp. 123, 139).

[125] B. P. Abbott et al. "GW170608: Observation of a 19 Solar-Mass Binary Black Hole Coalescence". In: *Astrophys. J. Lett.* 851.2 (Dec. 18, 2017), p. L35. DOI: 10.3847/2041-8213/aa9f0c (cit. on p. 123).

[126] B. P. Abbott et al. "GW170814: A Three-Detector Observation of Gravitational Waves from a Binary Black Hole Coalescence". In: *Phys. Rev. Lett.* 119.14 (Oct. 6, 2017), p. 141101. DOI: 10.1103/PhysRevLett.119.141101 (cit. on p. 123).

[127] R. Abbott et al. "Binary Black Hole Mergers in the First Advanced LIGO Observing Run". In: *Phys. Rev. X* 6.4 (Oct. 21, 2016). DOI: 10.1103/PhysRevX.6.041015 (cit. on p. 123).

[128] J. H. Taylor and R. A. Hulse. "A High-Sensitivity Pulsar Survey". In: *Astrophys. J.* 191 (July 1974), p. L59. DOI: 10.1086/181548 (cit. on p. 123).

[129] B. Allen et al. "FINDCHIRP: An Algorithm for Detection of Gravitational Waves from Inspiraling Compact Binaries". In: *Phys. Rev. D* 85.12 (June 19, 2012), p. 122006. DOI: 10.1103/PhysRevD.85.122006. arXiv: gr-qc/0509116 (cit. on p. 123).

[130] T. F. Collaboration. *GCN Notice 524666471*. Aug. 17, 2017. URL: https://gcn.gsfc.nasa.gov/other/524666471.fermi (visited on 07/07/2018) (cit. on p. 128).

[131] R. C. Essick and the LIGO Scientific Collaboration. *GCN Circular 21505*. Aug. 17, 2017. URL: https://gcn.gsfc.nasa.gov/gcn3/21505.gcn3 (visited on 07/07/2018) (cit. on p. 128).

[132] L. Singer and the LIGO Scientific Collaboration. *GCN Circular 21513*. Aug. 17, 2017. URL: https://gcn.gsfc.nasa.gov/gcn3/21513.gcn3 (visited on 07/07/2018) (cit. on p. 131).

[133] M. Ageron et al. *GCN Circular 21522*. Aug. 17, 2017. URL: https://gcn.gsfc.nasa.gov/gcn3/21522.gcn3 (visited on 07/07/2018) (cit. on pp. 131, 138).

[134] D. A. Coulter et al. *GCN Circular 21529*. Aug. 18, 2017. URL: https://gcn.gsfc.nasa.gov/gcn3/21529.gcn3 (visited on 07/07/2018) (cit. on p. 131).

[135] D. A. Coulter et al. "Swope Supernova Survey 2017a (SSS17a), the Optical Counterpart to a Gravitational Wave Source". In: *Science* 358.6370 (Dec. 22, 2017), pp. 1556–1558. DOI: 10.1126/science.aap9811. arXiv: 1710.05452 (cit. on p. 131).

[136] M. Ageron et al. *GCN Circular 21631*. Aug. 21, 2017. URL: https://gcn.gsfc.nasa.gov/gcn3/21631.gcn3 (visited on 07/07/2018) (cit. on pp. 132, 140).

[137] V. A. Villar et al. "The Combined Ultraviolet, Optical, and Near-Infrared Light Curves of the Kilonova Associated with the Binary Neutron Star Merger GW170817: Unified Data Set, Analytic Models, and Physical Implications". In: *Astrophys. J.* 851 (Dec. 8, 2017), p. L21. DOI: 10.3847/2041-8213/aa9c84 (cit. on p. 133).

[138] K. P. Mooley et al. "A Mildly Relativistic Wide-Angle Outflow in the Neutron Star Merger GW170817". In: *Nature* 554.7691 (Dec. 20, 2017), pp. 207–210. DOI: 10.1038/nature25452. arXiv: 1711.11573 (cit. on pp. 133, 135, 136).

[139] M. M. Kasliwal et al. "Illuminating Gravitational Waves: A Concordant Picture of Photons from a Neutron Star Merger". In: *Science* 358.6370 (Dec. 22, 2017), pp. 1559–1565. DOI: 10.1126/science.aap9455 (cit. on p. 133).

[140] B. P. Abbott et al. "A Gravitational-Wave Standard Siren Measurement of the Hubble Constant". In: *Nature* 551.7678 (Oct. 16, 2017), pp. 85–88. DOI: 10.1038/nature24471. arXiv: 1710.05835 (cit. on p. 136).

[141] N. Jackson. "The Hubble Constant". In: *Living Rev. Relativ.* 10 (Sept. 1, 2007), p. 52. DOI: 10.12942/lrr-2007-4 (cit. on p. 136).

[142] W. D. Pozzo. "Measuring the Hubble Constant Using Gravitational Waves". In: *J. Phys. Conf. Ser.* 484.1 (2014), p. 012030. DOI: 10.1088/1742-6596/484/1/012030 (cit. on p. 136).

[143] B. P. Abbott et al. "Gravitational Waves and Gamma-Rays from a Binary Neutron Star Merger: GW170817 and GRB 170817A". In: *Astrophys. J.* 848.2 (Oct. 16, 2017), p. L13. DOI: 10.3847/2041-8213/aa920c (cit. on p. 136).

[144] S. Boran et al. "GW170817 Falsifies Dark Matter Emulators". In: *Phys. Rev. D* 97.4 (Feb. 13, 2018), 041501(R). DOI: 10.1103/PhysRevD.97.041501. arXiv: 1710.06168 (cit. on p. 136).

[145] J. Aguilar et al. "A Fast Algorithm for Muon Track Reconstruction and Its Application to the ANTARES Neutrino Telescope". In: *Astropart. Phys.* 34.9 (Apr. 2011), pp. 652–662. DOI: 10.1016/j.astropartphys.2011.01.003 (cit. on p. 138).

[146] M. Ageron et al. "The ANTARES Telescope Neutrino Alert System". In: *Astropart. Phys.* 35.8 (Mar. 2012), pp. 530–536. DOI: 10.1016/j.astropartphys.2011.11.011. arXiv: 1103.4477 (cit. on p. 138).

[147] A. Albert et al. "Search for High-Energy Neutrinos from Binary Neutron Star Merger GW170817 with ANTARES, IceCube, and the Pierre Auger Observatory". In: *Astrophys. J.* 850.2 (Nov. 30, 2017), p. L35. DOI: 10.3847/2041-8213/aa9aed. arXiv: 1710.05839 (cit. on pp. 144, 145, 149).

[148] T. Kintscher. "Results and Prospects of IceCube's Real Time Alert Capabilities". In: *J. Phys. Conf. Ser.* 718.6 (June 9, 2016), p. 062029. DOI: 10.1088/1742-6596/718/6/062029 (cit. on p. 144).

[149] M. G. Aartsen et al. "The IceCube Realtime Alert System". In: *Astropart. Phys.* 92 (June 2017), pp. 30–41. DOI: 10.1016/j.astropartphys.2017.05.002. arXiv: 1612.06028 (cit. on p. 144).

Résumé en français

Ma thèse a pour sujet la recherche de neutrinos de hautes énergies résultant de l'interaction de rayons cosmiques dans la Galaxie avec le télescope à neutrino ANTARES. J'ai également participé au suivi neutrino de l'événement d'onde gravitationnelle GW170817 résultant de la coalescence d'un système binaire d'étoiles à neutrons.

Ces deux analyses sont développées ci-dessous. Elles m'ont permis d'acquérir des compétences solides en analyse de données ainsi que des connaissances plus théoriques autant sur l'accélération et la propagation des rayons cosmiques dans la Galaxie que sur les coalescences de système binaire et leur émission gravitationnelle.

Émission galactique de neutrinos

L'origine du flux diffus de neutrinos cosmiques détecté par la collaboration IceCube est encore inconnue. Le but de l'analyse présentée ici est d'explorer l'hypothèse d'une composante Galactique de ce flux.

Ces dernières années, le télescope *Fermi*-LAT a fourni une mesure détaillée du flux de rayons gamma de hautes énergies provenant du plan Galactique. La partie diffuse de ce flux au-delà de quelques GeV peut être attribuée en majorité à l'interaction des rayons cosmiques avec le milieu interstellaire. Ces interactions produisant des rayons gamma ainsi que des neutrinos par le biais de la désintégration de pions neutres et chargés, respectivement. Le modèle KRAγ (D. Gaggero et al. 2015. Astrophys. J. 815(2):L25) pris comme référence pour cette étude fournit un modèle de ce flux de neutrinos à partir des données de *Fermi*-LAT. En utilisant une dépendance radiale du coefficient de diffusion des rayons cosmiques, ce modèle prédit un flux de neutrinos particulièrement élevé, principalement dans le centre Galactique. Le modèle existe en deux versions correspondant à différentes coupures en énergie du spectre des rayons cosmiques, à 5 et 50 PeV/nucléon. On appellera ces deux versions KRAγ^{5} et KRAγ^{50}, respectivement. Ces valeurs ont été choisies par les auteurs pour encadrer les données de KASCADE et KASCADE-Grande.

J'ai fondé cette analyse sur la maximisation d'une fonction de vraisemblance afin d'estimer le nombre d'événements de signal ayant les caractéristiques du modèle dans les données. J'ai pris en compte les informations spatiales ainsi que l'énergie estimée des événements. Ensuite, j'ai utilisé un rapport de vraisemblance comme test statistique afin de comparer les données à des

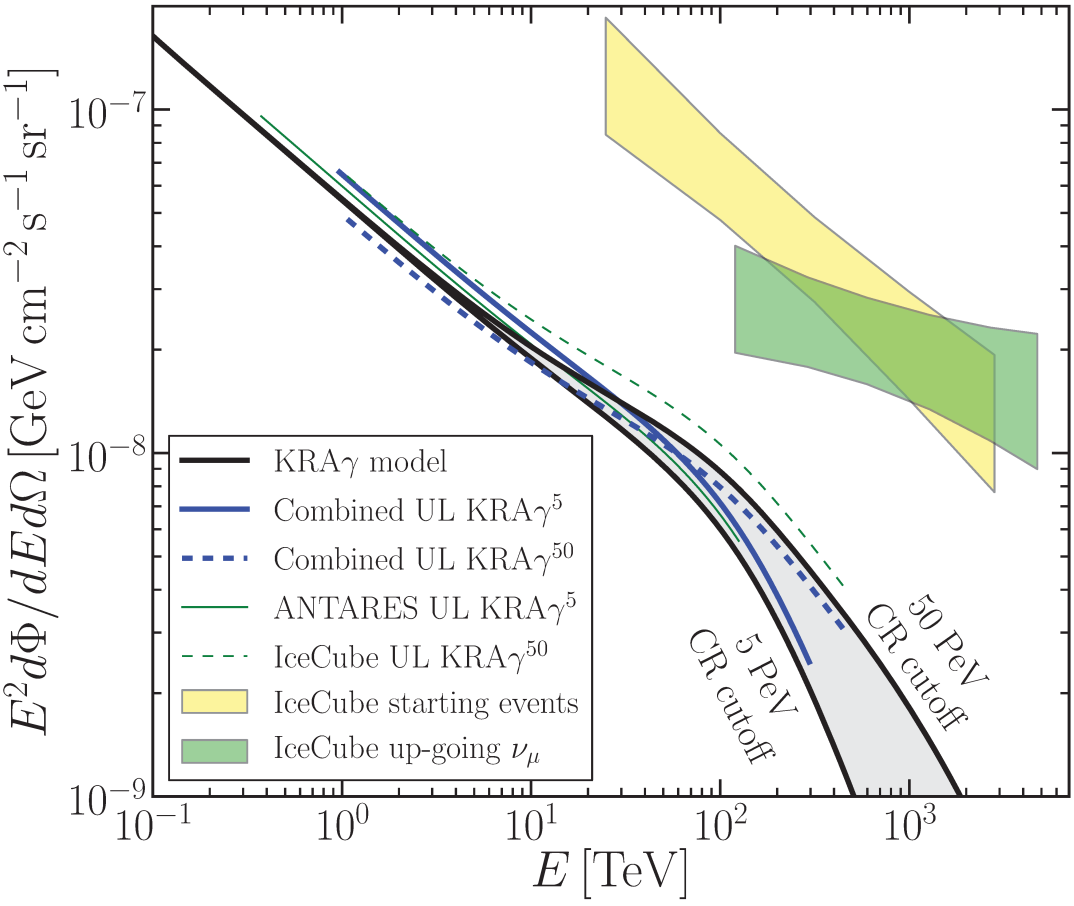

Figure 11.2 – Limite supérieure (ligne bleue) avec un niveau de confiance de 90 %, sur le flux de neutrino toutes saveurs du modèle KRAγ avec une coupure sur le spectre des rayons cosmiques à 5 et 50 PeV (lignes noires). Les lignes vertes représentent les précédentes limites par IceCube et ANTARES. Les flux isotropes de neutrinos astrophysiques mesurés par IceCube avec les événements HESE (jaune) et les traces montantes (vert) sont représentés par les surfaces colorées.

pseudo-expériences simulées pour lesquelles la proportion de signal est connue. Cela permet d'évaluer la probabilité que nos données contiennent du signal. Cette analyse, que j'ai menée dans son intégralité, a été parmi les premières analyses sensibles à toutes les saveur de neutrinos grâce à l'ajout des événements de type cascade.

Les résultats de cette analyse ont donné lieu à une publication (A. Albert et al. 2017. Phys. Rev. D. 96(6)). J'ai également travaillé en collaboration avec une équipe d'IceCube pour combiner les données des deux détecteurs, ce qui donnera lieu à une autre publication.

Comme on peut le voir sur la figure 11.2, l'analyse combinée nous a permis de rejeter le modèle KRAγ^{50}, et de mettre une limite à 120 % du flux de KRAγ^5. Ainsi, cette analyse contraint à moins de 9.6 % le nombre des événements contenus dans le détecteurs (appelés HESE) détectés par IceCube issus de l'interaction diffuse de rayons cosmiques dans la Galaxie.

Suivi de la Coalescence d'une binaire d'étoiles à neutrons

Le 17 août 2017, les collaborations LIGO et Virgo détectent pour la première fois des ondes gravitationnelles émises par la coalescence de deux étoiles à neutrons. 1.7 secondes plus tard, un sursaut gamma court était détecté spatialement compatible avec le signal d'ondes gravitationnelles. Cet événement a été suivi par de nombreux observatoires et marque le début d'une ère nouvelle de l'astronomie multimessager. Il a permis de confirmer le lien entre sursauts gamma courts et binaire d'étoile à neutrons, il a été suivi d'une détection claire de kilonova et a permis d'effectuer différent tests de la relativité générale. Je décris ici ma contribution au suivi de cet événement avec les données d'Antares.

L'observation d'une coalescence de binaire à travers un grand nombre de messagers cosmiques est idéale pour étudier les mécanismes d'accélération et d'émission de hautes énergies. En particulier l'observation de neutrinos révélerait le contenu hadronique et les mécanismes de dissipation dans les ejecta relativistes. Une détection prompte nous en apprendrait plus sur les mécanismes d'accélération des rayons cosmiques dans un éventuel jet alors qu'une détection tardive de neutrinos pourrait notamment permettre de révéler la présence d'un rémanent sous la forme d'un magnétar. Un tel objet pourrait en effet engendrer une nébuleuse dans laquelle les rayons cosmiques seraient accélérés par différents mécanismes.

Étant donné ma maîtrise des événements de type cascade, j'ai été amené à jouer un rôle majeur en les ajoutant au suivi de cet événement exceptionnel pour la première fois dans une analyse transitoire Antares. L'événement GW170817 n'étant pas visible avec les événements montants d'Antares, pour lesquels le bruit de fond des muons atmosphériques est drastiquement réduit, c'est également la première fois que les cascades descendantes étaient utilisées. Pour cette analyse, nous avons effectué une recherche ciblée d'événements en corrélation spatiale et temporelle avec la coalescence. Pour ce faire nous avons optimisé la sélection pour que la détection d'un événement mène à une significativité de 3σ tout en maximisant la probabilité de détecter un signal (pour un flux générique en E^{-2}) sur une fenêtre de temps de $\pm 500\,s$. Une recherche sur une fenêtre de temps de 14 jours après la coalescence a également été effectuée à la recherche d'une émission tardive.

Toute cette analyse s'est faite sur une courte période de temps afin que les résultats soient publiés en même temps que l'annonce de GW170817. Par conséquent, un article a été publié en commun avec les collaborations IceCube, Auger, LIGO et Virgo (A. Albert et al. 2017. Astrophys. J. 850(2):L35). Aucun neutrino en corrélation n'a été détecté, ce qui a permis de mettre des limites sur les modèles d'émission de neutrinos prompte et retardée. Nos résultats sont en outre compatibles avec l'hypothèse selon laquelle le jet n'était pas vu précisément le long de la ligne de visée.

Cette analyse a permis d'inclure les événements de type cascade aux suivis d'ondes gravitationnelles, ce qui sera systématique dans le cadre du prochain run d'observation Virgo/LIGO (O3).

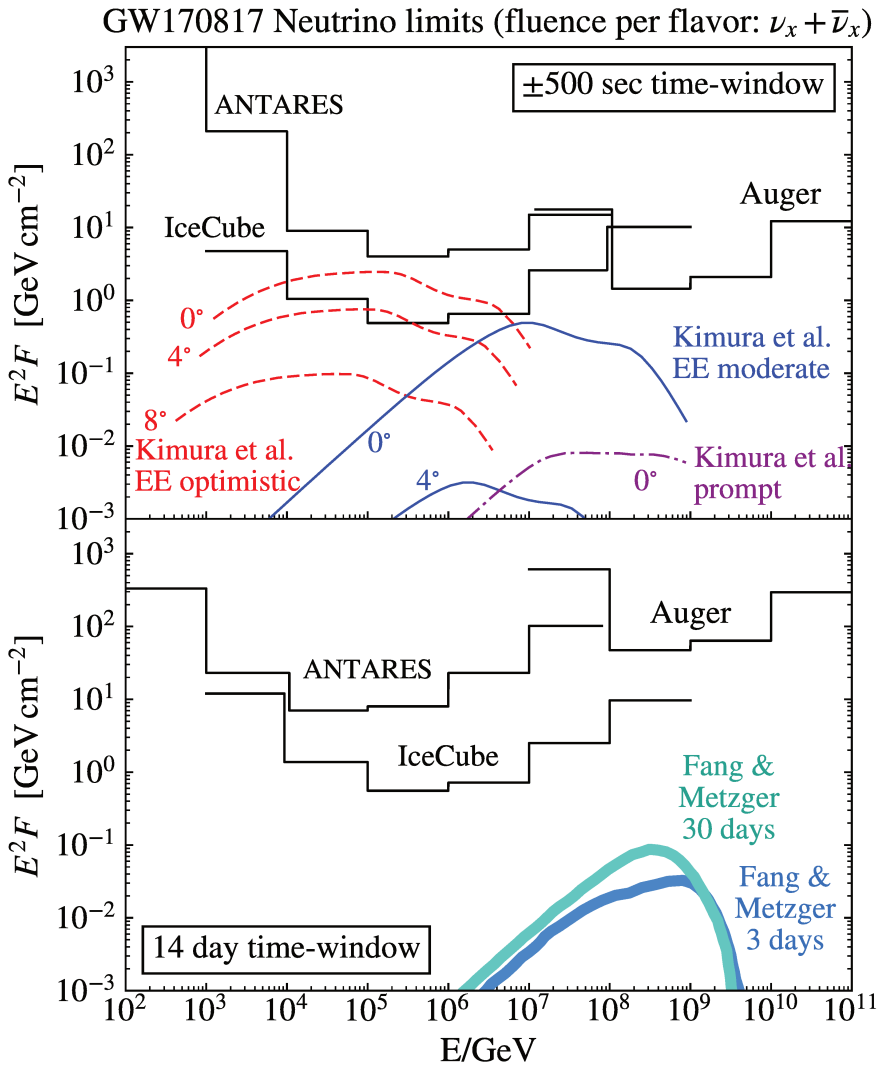

Figure 11.3 – Limites supérieures (à un niveau de confiance de 90%) sur la fluence spectrale de neutrinos provenant de GW170817 sur une fenêtre de temps de ± 500 s autour de la coalescence (panneau supérieur), et une fenêtre de 14 jours suivant le merger (panneau inférieur). Les émissions de neutrino prédites par par les différents modèles sont également représentés. Différents angles de visés du jet potentiel sont représentés, un angle de 0° correspond à un jet dirigé vers le système solaire.